

NATIONAL & INTERNATIONAL SCIENTIFIC EVENTS

6th International Conference on Food Digestion
(Granada 2019)

Venue: Granada Exhibition & Conference Centre
Location: Granada, Spain

Begins: April 2, 2019
Ends: April 4, 2019

8th International Conference on Nanotechnology
& Materials Science

Venue: Hotel Casa Amsterdam
Location: Amsterdam, The Netherlands

Begins: April 24, 2019
Ends: April 26, 2019

8th International Symposium on Delivery of Func-
tionality in Complex Food Systems

Venue: Sheraton Porto Hotel Conference Centre
Location: Porto, Portugal

Begins: July 7, 2019
Ends: July 10, 2019

47th IUPAC World Chemistry Congress

Venue: Palais des Congrès Paris
Location: Paris, France

Begins: July 7, 2019
Ends: July 12, 2019

10th International Conference on Nanotechnology:
Fundamentals and Applications (ICNFA'19)

Venue: Will be announced.
Location: Lisbon, Portugal

Begins: August 18, 2019
Ends: August 20, 2019

3rd World Congress on Electroporation and Pulsed
Electric Fields

Venue: Pierre Baudin Congress Centre (Centre de
Congrès)
Location: Toulouse, France

Begins: September 3, 2019
Ends: September 6, 2019

4th International Congress on 3D Printing (Ad-
ditive Manufacturing) Technologies and Digital
Industry 2019

Venue: Porto Bello Hotel Resort & Spa
Location: Antalya, Turkey

Begins: April 11, 2019
Ends: April 14, 2019

17th International Conference on Chemistry and
the Environment

Venue: Aristotle University KEDEA Building
Location: Aristotle University KEDEA Building,
Thessaloniki, Greece

Begins: June 18, 2019
Ends: June 20, 2019

22nd International Conference on General Relativ-
ity and Gravitation

Venue: Valencia Conference Centre
Location: Valencia, Spain

Begins: July 7, 2019
Ends: July 12, 2019

10th Triennial Congress of the International Soci-
ety for Theoretical Chemical Physics

Venue: Clarion Hotel The Edge
Location: Tromsø, Norway

Begins: July 11, 2019
Ends: July 17, 2019

6th Drug Discovery & Therapy World Congress
2019

Venue: Sheraton Boston Hotel, Boston, MA
Location: Boston, USA

Begins: September 3, 2019
Ends: September 5 2019

30th IEEE International Symposium on Personal,
Indoor and Mobile Radio Communication

Venue: Istanbul Congress Center (ICC)
Location: Istanbul, Turkey

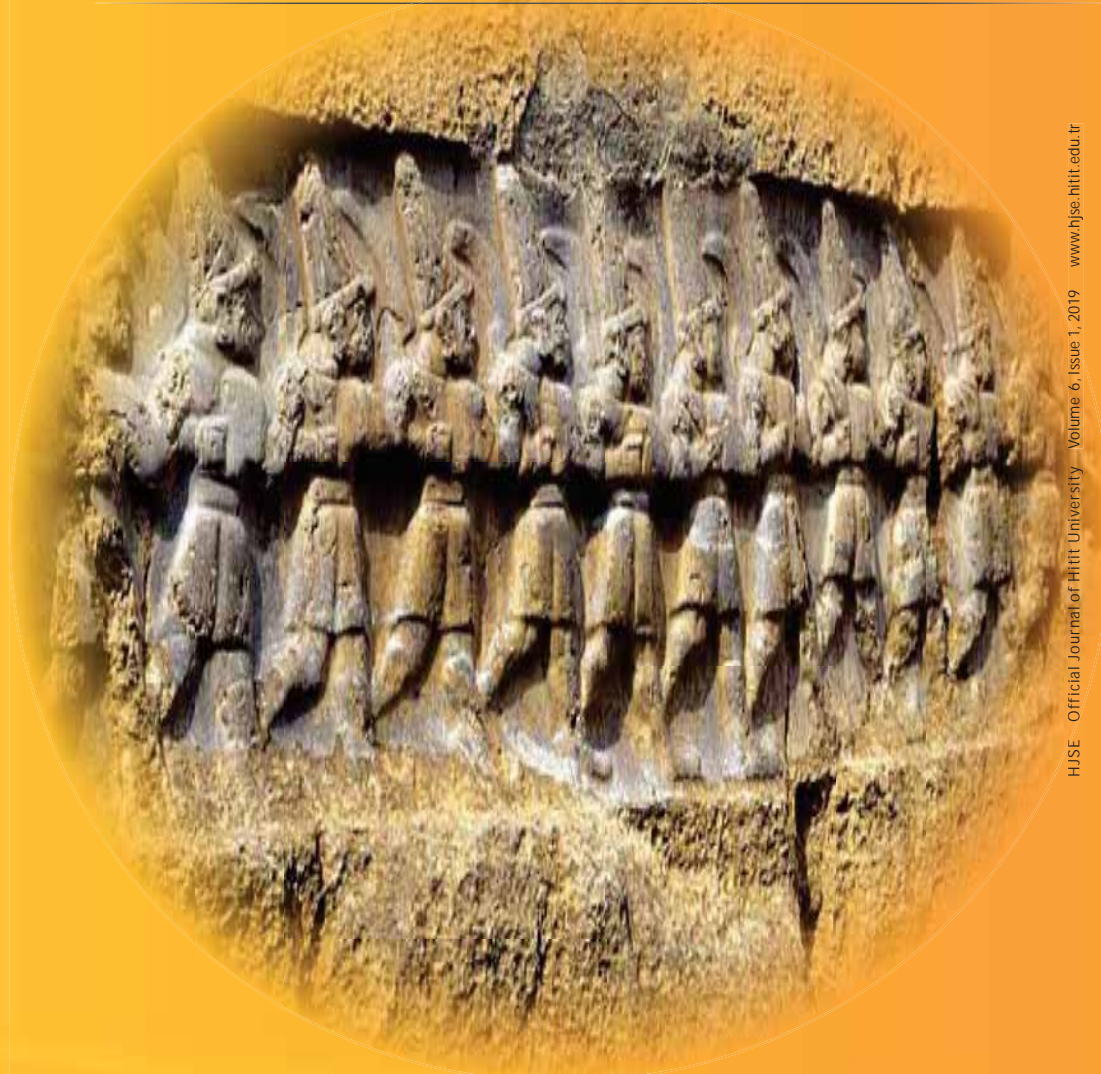
Begins: September 8, 2019
Ends: September 11, 2019



Abstracted & Indexed in:

TR Dizin Mühendislik ve Temel Bilimler Veri Tabanı |
CrossRef | Google Scholar | MIP Database | StuartxChange | ResearchBib | Scientific Indexing Services (SIS)

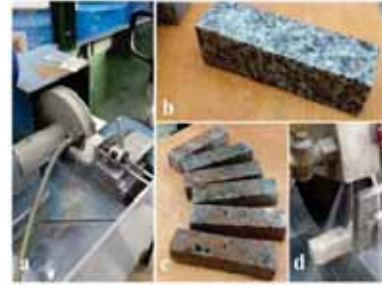
HITTITE



An Experimental Study on Determination of Crack Propagation Energy of Rock Materials under Dynamic (Impact) and Static Loading Conditions 01-06

Eren Komurlu

The Charpy impact test, a widely applied impact strength determination test for various materials such as metals, polymers and cementitious materials was performed to evaluate the crack propagation energy of 13 different granite type rock materials under the impact load condition.



Thermodynamic Optimization of Turbine Lines for Maximum Exergy Efficiency in a Binary Geothermal Power Plant 07-15

Ali Kecebas

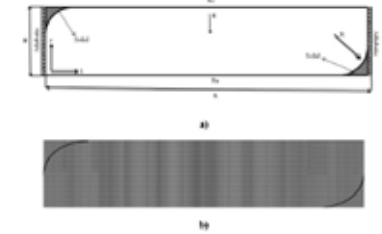
In this study, the pressure and mass flow rates on turbine lines are optimized to maximize Exergy efficiency in a binary ORC geo-thermal power plant (GPP).



Effects of Arc-Shaped Partitions in Corners of A Shallow Cavity on Natural Convection 17-23

Mert Gurturk, Hakan F. Oztop, Fatih Selimefendigil and Khaled Al-Salem

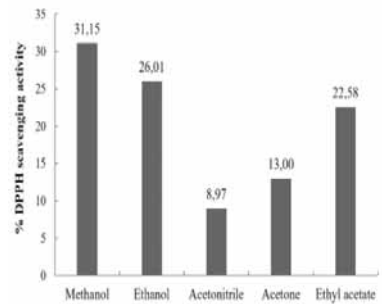
In this study, a numerical analysis carried out to determine the effects of arc-shaped partitions in corners of a shallow cavity on heat transfer which is natural convection and fluid flow.



Identification of Antioxidant Activity by Different Methods of a Freshwater Alga (Microspora sp.) Collected From a High Mountain Lake 25-29

Bulent Akar, Zeynep Akar and Bulent Sahin

In the present research, antioxidant activity of fresh-water alga *Microspora* sp. (Chlorophyta) extract prepared in different solvents (methanol, acetonitrile, ethanol, acetone and ethyl acetate) was determined with three different methods; 2,2-diphenyl-1 picrylhydrazyl (DPPH•), Iron (III) Reduction/Antioxidant Power (FRAP) Assay and Copper (II) Reductive Antioxidant Activity (CUPRAC).



Selfadjoint Singular Quasi-Differential Operators of First Order 31-35

Zameddin I. Ismailov and Pembe Ipek Al

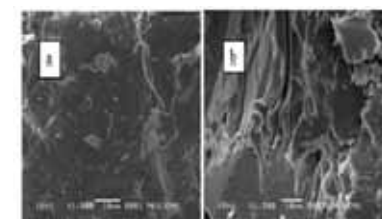
In this work, using the Calkin-Gorbachuk method firstly all selfadjoint extensions of the minimal operator generated by first order linear singular quasi-differential expression in the weighted Hilbert space of vector-functions on right semi-axis have been described.

$$\begin{aligned}
 &= \int_a^\infty w(t) \|u_-(t)\|_{\mathbb{H}}^2 dt \\
 &= \int_a^\infty \frac{w(t)}{\alpha^2(t)} \exp\left(2 \int_a^t \frac{w(s)}{\alpha^2(s)} ds\right) dt \|f\|_{\mathbb{H}}^2 \\
 &= \int_a^\infty \exp\left(2 \int_a^t \frac{w(s)}{\alpha^2(s)} ds\right) d\left(\int_a^t \frac{w(s)}{\alpha^2(s)} ds\right) \|f\|_{\mathbb{H}}^2 \\
 &= \frac{1}{2} \left(\exp\left(2 \int_a^\infty \frac{w(s)}{\alpha^2(s)} ds\right) - 1 \right) \|f\|_{\mathbb{H}}^2 < \infty.
 \end{aligned}$$

Synthesis, Characterization, Swelling Behavior and Metal Uptake Studies of Dichloroglyoxime Crosslinked Chitosan Derivative 37-44

Mahir Timur

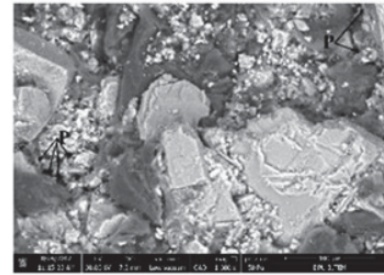
New crosslinked derivative of chitosan was prepared by the condensation reaction of chitosan (CS) and dichloro glyoxime.



An Investigation of the Effect of Pyrolytic Liquid Obtained From Waste Tire on the Corrosion Behaviours of MgO-C Refractories 45-49

Tuba Bahtli, V. Murat Bostanci, D. Yesim Hopa, N. Sevde Ulvan and S. Yalcin Yasti

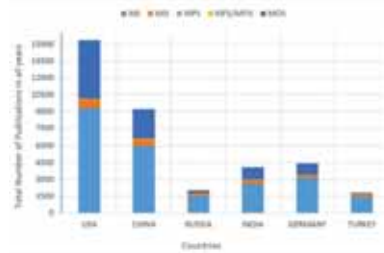
In this study, corrosion behaviours of MgO-C refractories by incorporating different binders as phenolic resin and pyrolytic liquid obtained by waste tire pyrolysis were investigated.



The Analysis of The Researches on Metal-Semiconductor Structures with and without Interfacial Layer in Turkey 51-56

Serhat Orkun Tan

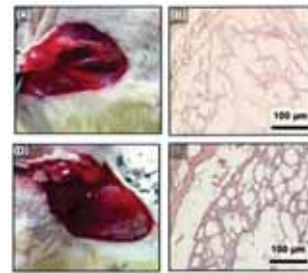
The analysis of the academic studies which are scanned in Web of Science database and made in Turkey were performed with data mining by using automated data collection methods and SQL Server Management Studio program.



Evaluation of Angiogenic Factor Release from Thermosensitive Poly(N-Vinylcaprolactam)-g-Collagen: In Vitro and In Vivo Studies 57-61

Serap Durkut

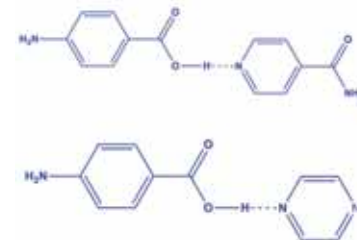
In this study, a thermosensitive poly(N-vinylcaprolactam)-g collagen (PNVCL-g-Col) hybrid hydrogel was synthesized by conjugation using the NHS/EDC cross-linking system, and characterized.



Synthesis and Characterization of Two New Co-Crystals: p-Aminobenzoic Acid with Isonicotinamide and Pyrazine (1:1) 63-68

Fureya Elif Ozbek

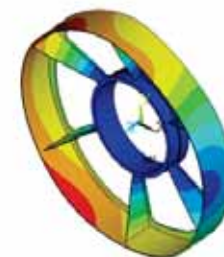
The thermal stability of the co-crystals was investigated by using DSC and it was determined that the melting points of the co-crystals 1 and 2 were lower and in-between from those of their coformers, respectively.



Lightweight design of Rotor Supporting for Large Permanent Magnet Direct Drive Wind Generator 69-73

Zhenyu Wu, Siming Wang and Ling Li

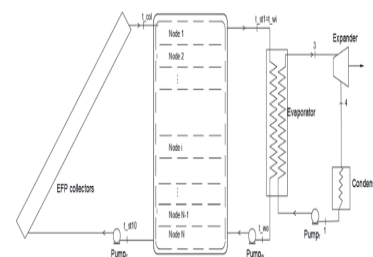
The final simulation shows that the stiffness can be met while reducing the mass by 40%.



Annual performance simulation of a solar cogeneration plant with sensible heat storage to provide electricity demand for a small community: A transient model 75-81

Cagri Kutlu, Jing Li, Yuehong Su, Yubo Wang, Gang Pei and Saffa Riffat

In this paper, a solar-driven power system as a means of meeting electricity demand in a small community has been investigated in terms of its transient performance on an annual basis.



Owner

Prof. Dr. Reha Metin ALKAN
on behalf of Hitit University

Editor-in-chief

Prof. Dr. Ali KILIÇARSLAN

Associate Editors

Prof. Dr. D. Ali KÖSE
Assist. Prof. Dr. Öncü AKYILDIZ

Production

Assoc. Prof. Dr. Kazım KÖSE
Mustafa Reşit HABOĞLU
Erhan ÇETİN
Harun Emre KIRAN
Ömer Faruk TOZLU

Editor's Office

Tel: +90 364 227 45 33 / 12 36

Fax: +90 364 227 45 35

Email: alikilicarslan@hitit.edu.tr

Subscription Service:

Tel: +90 364 227 45 33 / 12 82

Fax: +90 364 227 45 35

Email: hjse@hitit.edu.tr

EDITORIAL BOARD

Prof. Dr. İftikhar AHMAD

Prof. Dr. Mike BECKETT

Prof. Dr. İbrahim DİNÇER

Prof. Dr. Ali ELKAMEL

Prof. Dr. Mohamad S QATU

Prof. Dr. Saffa RIFFAT

Prof. Dr. Thanos SALIFOĞLU

Assoc. Prof. Dr. Yuehong SU

Dr. Wojciech NOGALA

Prof. Dr. Yusuf AYVAZ

Prof. Dr. Adil DENİZLİ

Prof. Dr. Ali GENCER

Prof. Dr. Metin GÜRÜ

Prof. Dr. Murat HOŞÖZ

Prof. Dr. Sadık KAKAÇ

Prof. Dr. Tarık Ömer OĞURTANI

Prof. Dr. Ender SUVACI

Assoc. Prof. Dr. Ali TOPÇU

Prof. Dr. Kazım Savaş BAĞÇECİ

Assoc. Prof. Dr. Cengiz BAYKASOĞLU

Prof. Dr. Vedat DENİZ

Prof. Dr. Hakan GÜNGÜNEŞ

Prof. Dr. Bülent KABAK

Prof. Dr. Ali KILIÇARSLAN

Prof. Dr. Dursun Ali KÖSE

Prof. Dr. İrfan KURTBAŞ

Assoc. Prof. Dr. Seyfi ŞEVİK

Prof. Dr. Dilber Esra YILDIZ

University of Malakand, Chakdara, Pakistan

Bangor University, Bangor, United Kingdom

Uoit Ontario University, Ontario, Canada

University of Waterloo, Ontario, Canada

Central Michigan University, Michigan, United States

The University of Nottingham, United Kingdom

Aristotle University of Thessaloniki, Thessaloniki, Greece

The University of Nottingham, United Kingdom

Polish Academy of Sciences, Poland

Suleyman Demirel University, Turkey

Hacettepe University, Turkey

Ankara University, Turkey

Gazi University, Turkey

Kocaeli University, Turkey

TOBB University, Turkey

Middle East Technical University, Turkey

Anadolu University, Turkey

Hacettepe University, Turkey

Hitit University, Turkey

Hitit University, Turkey

Hitit University, Turkey

Hitit University, Turkey

Hitit University, Turkey

Hitit University, Turkey

Hitit University, Turkey

Hitit University, Turkey

Hitit University, Turkey

Hitit University, Turkey

Journal Name : HITTITE JOURNAL OF SCIENCE AND ENGINEERING
Year : 2019
Managing Editor : Prof. Dr. Ali KILIÇARSLAN
Managing Office : Hitit University Faculty of Engineering
Managing Office Tel : +90 364 227 45 33 / 12 36
Publication Language : English
Publication Type : Peer Reviewed, Open Access, International Journal
Delivery Format : 4 times a year (quarterly)
Print ISSN : 2149-2123
Online ISSN : 2148-4171
Publisher Address : Hitit Üniversitesi Kuzey Kampüsü Çevre Yolu Bulvarı
19030 Çorum / TÜRKİYE
Publisher Tel : +90 364 227 45 33/1236



This new issue of Hittite Journal of Science and Engineering contains twelve manuscripts from the disciplines of chemistry, mathematics, biology, chemical engineering, electrical and electronics engineering, mechanical engineering, civil engineering, materials science and engineering, food engineering, tissue engineering. These manuscripts were first screened by Section Editors using plagiarism prevention software and then reviewed and corrected according to the reviewer's comments. I would like to express my gratitude to all our authors and contributing reviewers of this issue.

I would like to thank to the President of Hitit University, Dr. Reha Metin Alkan, for his constant interest in HJSE and also to the Associate Editors of HJSE, namely Dr. Dursun Ali Kose and Dr. Oncu Akyıldız, as well as our Production Editors Dr. Kazim Kose, Mustafa Reşit Haboğlu, Erhan Çetin, Harun Emre Kıran and Ömer Faruk Tozlu for their invaluable efforts in making of the journal.

It's my pleasure to invite the researchers and scientists from all branches of science and engineering to join us by sending their best papers for publication in Hittite Journal of Science and Engineering.

Dr. Ali Kiliçarslan

Editor-in-Chief

An Experimental Study on Determination of Crack Propagation Energy of Rock Materials under Dynamic (Impact) and Static Loading Conditions

Eren Komurlu 

Giresun University, Department of Civil Engineering, Giresun, Turkey

ABSTRACT

The Charpy impact test, a widely applied impact strength determination test for various materials such as metals, polymers and cementitious materials was performed to evaluate the crack propagation energy of 13 different granite type rock materials under the impact load condition. Additionally, crack propagation energies of the granite materials were determined under the static load condition to compare the results with those of the Charpy impact test. The energy levels measured from static load tests were significantly lower than those obtained from the dynamic load test that the ratio of energy level under the dynamic loading to energy level under static loading condition was measured to change between 39 and 200 for different 13 type of granite materials tested in this study. The crack propagation time for the chevron-notched specimens under static loading was also measured using professional sound recording systems. As results of this study have not indicated that the crack propagation speed and energy values measured from different granite materials have a direct relationship, energy-dependent crack propagation speed was found to be an inherent property of rock materials. The Charpy impact test was assessed usable for being a sensitive crack propagation energy determination method for rock materials. In the context of improvement of the Charpy impact test for rock materials, some issues were pointed out in this study.

Keywords:

Crack propagation in rock materials; Impact strength of rock materials; Charpy test; Impact energy; Dynamic loading; Fracture toughness

INTRODUCTION

Determination of the fracture toughness of rock materials can be carried out under different conditions of static and dynamic loads, by following various testing methods suggested by different researchers, standards and International Society of Rock Mechanics and Rock Engineering [1-10]. Although there are numerous researches to get deeper to identify the fracture mechanics of rock materials under cyclic (dynamic) loading and better understand the differences in behaviour of fracturing under cyclic and static loads, it is still a need to focus on more and suggest a standard testing method for determination of fracture toughness of rock materials being exposed to impact load, another type of dynamic loading induced in various rock engineering applications. Rock fracture toughness values under the impact loading condition are key parameters for various rock engineering applications such as percussion drilling, use

of various mechanical excavation machines, blasting operations, absorption of the rock bursting energy and etc. [11-15].

In this study, the Charpy impact test, a widely applied impact strength determination test for various materials such as metals, polymers, cementitious materials like concrete mixes and ceramics was performed to determine the fracture energy of 13 different granite type rock materials. Since it is practical and cheap for obtaining results quickly, the Charpy impact test was thought to be a potential test for being popular in impact strength determination of rock materials. In the Charpy impact test, notched beam specimens are hit by a hammer carried on a pendulum which is allowed to fall freely to supply impact energy. As the hammer hits to the opposite face directly behind the notch, an amount of energy is consumed for crack propa-

Article History:

Received: 2017/11/07

Accepted: 2018/12/26

Online: 2019/01/31

Correspondence to: Eren Komurlu
Giresun University, Department of Civil
Engineering
Tel: 0(454) 3101740
E-Mail: erenkomurlu@gmail.com

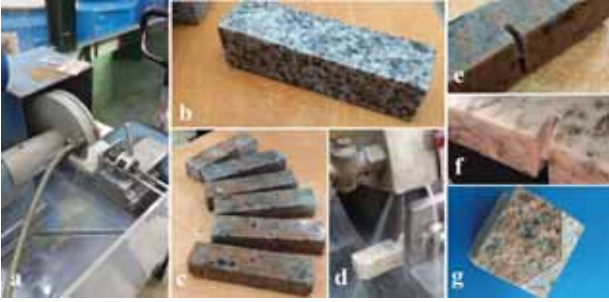


Figure 1. Block cutting (a, b, c), Chevron notch cutting and design (d, e, f, g)

gation. To measure the energy consumption amount, the height difference between the initial position and which the pendulum rises after failure is recorded by a pointer mounted on the dial.

Chevron notched granite specimens were prepared in this study to be applied both three-point flexural strength and Charpy impact tests for determination of the Mode I type fracture toughness and energy consumption for crack propagation values under different conditions of static and dynamic (impact) loading. The chevron-notches are artificial cracks and make initiation of the crack at the chevron tips. The chevron-notched geometry is made by the various machining operations, whose the simplest one is to use a rotating saw blade resulting in the sides of the notch, as done in this study.

MATERIALS AND METHODS

In this study, different Turkish granite blocks were cut into pieces to prepare specimens with dimensions of 25 mm x 25 mm x 80 mm. As seen in Fig. 1 which shows specimen preparation steps, the chevron notched artificial cracks were made using a circular saw with a diameter of 20 cm and a thickness of 1.3 mm. Because of the abrasion of rock samples during the cutting process, the notch width was mostly measured to vary between 2 mm and 3 mm, depending on the rock material. The chevron notch cutting depth was 8 mm for all specimens.

To determine Mode I type fracture toughness of the chevron-notched specimens under static loading, three-point flexural strength test was applied using an electric motor press with a maximum load level of 50 kN, which is a sensitive loading equipment to be used for low strength materials. The loading rate of 1mm/min was



Figure 2. A three point flexural strength test specimen before loading (a) and after failure (b)



Figure 3. Charpy impact strength test: the test equipment (a), a specimen put in the abutments (b), lifting hammer (c, d), hammer dropped and determination of maximum hammer height after crack propagation (e), a failed specimen (f)

chosen to determine failure load in the three-point flexural strength test of the chevron notched specimens put on the abutments with a distance of 4 cm between each other (Fig.2). Similarly, Charpy impact test specimens had a gap dimension of 4 cm between the abutments where the specimens were put in (Fig. 3). As the hammer with the weight of 5 kg is dropped from 1 meter height, an energy level of 50 Joule was applied on the chevron notched specimens used in the Charpy impact test. As in the static load test, the bending effect was induced as the falling hammer applies load to the specimens used in the Charpy impact test. It should be noted herein that specimens of static and dynamic load tests were cut to have the same size of 25 mm x 25mm x 80 mm. In the Charpy test, differences in falling hammer height before and after the failure of specimens were read from the gage to define the energy consumption for crack propagation through the specimens.

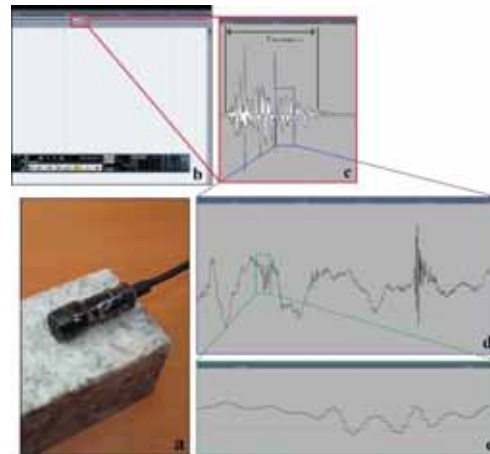


Figure 4. a) Contact microphone stuck on a specimen, b, c, d, e) recorded sound wave from a Granite 1 type specimen (t: crack propagation time)

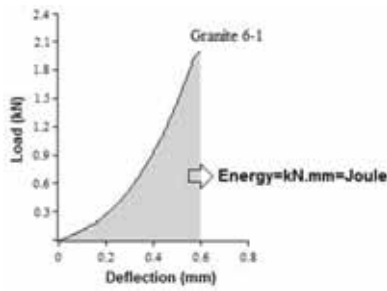


Figure 4. Logarithm of flow curves in rolling direction

A contact microphone was stuck on static load test specimens to record cracking sound for measuring the propagation time. The crack propagation time could be measured with a sensitivity of 0.01 millisecond, using a professional music production program and an external audio card for professional sound recording. An example of sound waves recorded during the crack propagation is given in Fig. 4. In addition to crack propagation time, deflections of the static load test specimens were measured by using the LVDT device. For 13 different granite materials named from Granite 1 to Granite 13, maximum loads, load-deflection graphs and crack propagation times were determined for static load specimens to investigate the relation between static load test results and energy consumption data obtained with the Charpy impact test.

RESULTS AND DISCUSSION

The maximum load and the area under the load-deflection curves of granite specimens tested in this study are respectively given in Table 1 and Table 2. Areas under the load-deflection curves were calculated to determine the energy level causing to break the resistance against the natural crack occurrence, as seen in Fig. 5. As another parameter measured during the static loading test, duration of the crack propagation data is given in Table 3. Depending on the crack propagation time, crack propaga-

Table 2. Areas under load-deflection curves (E: Energy, S.D: Standard Deviation)

Specimen name	E (milliJoule)	S.D. in E (milliJoule)	Specimen number
Granite 1	441	20	3
Granite 2	399	34	3
Granite 3	93	10	3
Granite 4	357	36	3
Granite 5	219	19	3
Granite 6	486	27	3
Granite 7	204	15	3
Granite 8	90	7	3
Granite 9	126	23	3
Granite 10	105	11	3
Granite 11	204	12	3
Granite 12	354	10	3
Granite 13	60	7	3

tion distance and energy levels given in Table 2, time-dependent energy consumption for crack propagation rate in Watt unit (J/s), energy-dependent crack propagation speed (m/Js=1/Ns) and energy consumption per a unit crack surface area occurrence (J/m²=N/m) are given in Table 4. The crack propagation distance was 23 mm from the tip of the notch to the specimen end. Because all the specimens tested in this study has the same crack surface area and same specimen dimensions, energy consumption per unit crack surface area is directly proportional to the crack propagation energy. Two-sided cracking surface cross-section area of 10 cm² (5 cm2x2) was considered to calculate values in Table 4. The energy consumption values determined by applying the Charpy impact test for crack propagation under the dynamic load are given in Table 5.

Table 1. Results obtained with static load test

Specimen name	Fmax (kN)	S.D. in Fmax (kN)	Specimen number
Granite 1	1.26	0.07	3
Granite 2	1.20	0.11	3
Granite 3	0.92	0.10	3
Granite 4	1.17	0.11	3
Granite 5	1.02	0.08	3
Granite 6	1.95	0.06	3
Granite 7	0.41	0.09	3
Granite 8	0.54	0.07	3
Granite 9	0.63	0.05	3
Granite 10	0.35	0.02	3
Granite 11	1.34	0.10	3
Granite 12	1.26	0.13	3
Granite 13	0.38	0.05	3

Table 3. Crack propagation durations

Specimen name	t (millisecond)	S.D. in t (millisecond)	Specimen number
Granite 1	90	8	3
Granite 2	65	7	3
Granite 3	105	7	3
Granite 4	157	10	3
Granite 5	119	5	3
Granite 6	18	2	3
Granite 7	29	4	3
Granite 8	26	2	3
Granite 9	323	34	3
Granite 10	305	23	3
Granite 11	40	3	3
Granite 12	61	9	3
Granite 13	246	16	3

Table 4. Energy consumption rate and crack propagation speed under static load

Specimen name	Energy Consumption rate (Watt)	Crack propagation speed (m/s)	Energy dependent crack propagation speed (1/Ns)	Energy consumption per crack surface area (mJ/cm ²)
Granite 1	4.90	0.26	0.59	44.1
Granite 2	6.14	0.35	0.88	39.9
Granite 3	0.89	0.22	2.37	9.3
Granite 4	2.27	0.15	0.42	35.7
Granite 5	1.84	0.19	0.87	21.9
Granite 6	27.00	1.28	2.63	48.6
Granite 7	7.03	0.79	3.87	20.4
Granite 8	3.46	0.88	9.78	9.0
Granite 9	0.39	0.07	0.56	12.6
Granite 10	0.34	0.08	0.76	10.5
Granite 11	5.10	0.58	2.84	20.4
Granite 12	5.80	0.38	1.07	35.4
Granite 13	0.24	0.09	1.50	6.0

It was seen that crack propagation characteristic of rock materials significantly differ depending on loading under static or dynamic conditions. As an example, specimens of Granite 6 having high fracture toughness and energy consumption level for crack propagation under the static load condition had significantly less fracture propagation energy under the impact load condition in comparison with that of Granite 11 with relatively low energy capacity under static loading condition. The relation between crack propagation energy and fracture toughness values was found to be dependent on rock material and not convenient for a generalization. Also, the energy levels measured from static load tests were not found related to the crack propa-

Table 5. Energy consumption values determined by the Charpy test (E: Energy)

Specimen name	E (Joule)	S.D. in E (Joule)	Specimen number
Granite 1	26	1.5	3
Granite 2	29	1.7	3
Granite 3	14	0.6	3
Granite 4	23	1.0	3
Granite 5	16	2.1	3
Granite 6	19	1.2	3
Granite 7	20	1.5	3
Granite 8	12	1.5	3
Granite 9	11	1.0	3
Granite 10	21	2.5	3
Granite 11	33	2.7	3
Granite 12	24	3.1	3
Granite 13	10	1.2	3

gation energy in dynamic load test that the ratio of energy level under the dynamic loading to energy level under static loading condition was measured to change between 39 and 200 for different 13 type of granite samples tested in this study. The energy level under the static load and deflection graphs which was found to be lower than energy levels obtained with the Charpy impact test for all rock materials tested in this study confirms that energy consumption for crack propagation increases with an increase in loading rate [16-19]. The crack propagation time increasing with a decrease in the loading rate is accepted to be a reason for the issue of measuring energy level under static load to be lower than those obtained from the impact test [20-22].

In fracture toughness tests, the load level for start of crack propagation is reached step by step under static loading condition. On the other hand, the load level for the start of crack propagation is immediately applied on the material under impact effect. In case of the crack propagation under the static load condition, a stress level applies on the crack boundaries as a dependent on the energy absorbed during the increase of static load [23-29].

Because the load level needed for crack propagation increases with an increase in the loading rate, higher load levels than those in the static loading condition are expected to reach in Charpy impact tests, which can be accepted as another reason for having higher energy absorption capacity under impact effect [30,31]. Because the crack propagation mode varies by a transition from a dominant main crack at the low load rates to one resulting from both main crack and micro-cracking ahead of the main crack at the high loading rates, the plastic dissipation in the fracture process zone increases with increasing loading rate as an issue that causes to increase the load level and energy consumption for cracking under impact load condition [32,33].

Energy consumption rate during crack propagation and crack propagation speed per energy level are some significant parameters in different Rock Engineering applications with immediate loading such in blasting operations. As an outcome of this study, time-dependent energy consumption rate (Watt) was not found related with fracture toughness value and energy consumption values measured in both dynamic loading and static loading conditions. Results of this study have not indicated that the crack propagation speed and fracture toughness values measured from different granite materials have a direct relationship. The energy-dependent crack propagation speed was found to be an inherent property of rock materials.

The crack propagation speed should be focussed on as an important parameter for bettering in different applications such as the determination of delaying time between

blasting holes to improve excavation performance [34-38]. According to the results, energy level dependent crack propagation speed was assessed to be an inherent material property with the unit of 1/Ns. As crack propagation speed and energy level to break the resistance against the start of crack propagation are known to vary with a change in initial impact energy of the falling hammer, a definite energy level to be applied in the Charpy impact test is suggested to investigate in the standardization studies [39-41].

The Charpy impact test, a popular test carried out to determine the impact strength of many different materials such as ceramics, concrete, steel materials is suggested to be also used for evaluation of crack propagation energy of rock materials under impact load condition. A standard Charpy impact test equipment development for the core specimens with widely used diameter dimensions like the NX core size is thought to be a significant contribution in the field of rock testing.

As a very basic assumption by considering the energy transformation, 1 meter height of drop makes the hammer to have 4.4 m/s speed when it contacts to the Charpy impact test specimen. In case of lower speed of crack propagation resulting from the response of rock materials to the impact energy than that of the impact hammer motion, crack propagation speed is expected to be artificially increased by the motion of the hammer. In different applications, crack propagation speed is varied due to the motion of tools such in the applications of various mechanical excavation machines. In addition to the impact energy level, tool speed is an individual effect on crack propagation energy [42-45]. For improvement of a new Charpy test equipment, the hammer fall velocity effect is found to be investigated for evaluation of crack propagation energies. Therefore, some modified versions of the test equipment would be used for different testing conditions considering hammer fall energy and speed differences. For instance, natural crack propagation speed can be determined under an immediate energy loading with a very slow hammer motion. To decrease the speed of hammer motion without having no decrease in the impact energy, it is suggested to use a weighty hammer and short drop heights. On the other hand, a high height of the fall and low weight hammers can be used for having relatively high velocities without an increase in the energy level applied in the Charpy impact test.

For the aim of making an advanced Charpy test equipment, high speed cameras are usable to measure crack propagation time and follow the crack propagation steps taking a time as short as microseconds [46-50].

CONCLUSION

The crack propagation resistivity of the rock materials

was determined to significantly change depending on testing under static or impact (dynamic) loading condition. Therefore, it is the proper way to determine fracture toughness values and crack propagation energy levels under the relevant load condition. The Charpy impact test is suggested to use for sensitive determination of the crack propagation energies of rock specimens and improve for being applied as an advanced impact test for rock materials.

REFERENCES

1. ISRM. The Orange Book-The ISRM Suggested Methods for Rock Characterization, Testing and Monitoring: 2007–2014 (ed. by Ulusay R). Springer, Cham, Switzerland, 2014.
2. ISRM. The Blue Book-The complete ISRM Suggested Methods for Rock Characterisation, Testing and Monitoring: 1974–2006 (ed. by Ulusay R, Hudson JA). Turkish National Group of ISRM, Ankara, 2007.
3. ISRM. Suggested method for determining mode I fracture toughness using cracked chevron notched Brazilian disk (CCNBD) specimens. *Int. J. Rock Mech. Min. Sci. Geomech. Abstr.* 32 (1995) 57–64.
4. ISRM. Suggested methods for determining the fracture toughness of rock. *International Journal of Rock Mechanics and Mining Sciences & Geomechanics Abstracts* 25 (1988) 71–96.
5. Backers T. Fracture Toughness Determination and Micromechanics of Rock Under Mode I and Mode II Loading, PhD Thesis. University of Potsdam, Germany, 2004.
6. Funatsu T, Shimizu N, Kuruppu M, Matsu K. Evaluation of mode I fracture toughness assisted by the numerical determination of K-resistance. *Rock Mechanics and Rock Engineering* 48 (2014) 143–157.
7. Tutluoglu L, Keles C. Mode I fracture toughness determination with straight notched disk bending method. *International Journal of Rock Mechanics and Mining Sciences* 48 (2011) 1248–1261.
8. Zhou YX, Xia K, Li XB, Li HB, Ma GW, Zhao J, Zhou ZL, Dai F. Suggested methods for determining the dynamic strength parameters and mode-I fracture toughness of rock materials. *International Journal of Rock Mechanics and Mining Sciences* 49 (2012) 105–112.
9. Whittaker BN, Singh RN, Sun G. *Rock Fracture Mechanics: Principles, Design and Applications*. Elsevier, Amsterdam, 1992.
10. Shetty DK, Rosenfield AR, Duckworth WH. Fracture toughness of ceramics measured a chevron-notched diametral-compression test. *Journal of American Ceramic Society* 68 (1985) C325–C327.
11. Altindag R. The evaluation of rock brittleness concept on rotary blast hole drills. *Journal of South African Institute of Mining and Metallurgy* 102 (2002) 61–66.
12. Altindag R. Correlation of specific energy with rock brittleness concepts on rock cutting. *Journal of South African Institute of Mining and Metallurgy* 103 (2003) 163–71.
13. Tiryaki B. Evaluation of the indirect measures of rock brittleness and fracture toughness in rock cutting. *Journal of South African Institute of Mining and Metallurgy* 106 (2006) 407–423.
14. Kaiser PK, Cai M. Design of rock support system under rockburst condition. *Journal of Rock Mechanics and Geotechnical Engineering* 4 (2012) 215–227.
15. Cai M. Prediction and prevention of rockburst in metal mines - A case study of Sanshandao gold mine. *Journal of Rock Mechanics*

- and Geotechnical Engineering 8 (2016) 204-211.
16. Zhang QB, Zou Y. Effect of loading rate on fracture behaviour of rock materials, in: Proceedings of Eurock 2014, Vigo, Spain, 2014, pp. 119-124.
 17. Zejian X, Yulong L. Study of loading rate effect on dynamic fracture toughness of high strength steel under impact loading. Strength, Fracture and Complexity 6 (2010) 17-23.
 18. Marsavina L, Linul E, Voiconi T, Sadowski T. A comparison between dynamic and static fracture toughness of polyurethane foams. Polymer Testing 32 (2013) 673-680.
 19. Fuenkajorn K, Sriapai T, Samsri P. Effects of loading rate on strength and deformability of Maha Sarakham salt. Engineering Geology 135-136 (2012) 10-23.
 20. Hsieh CT, Wang CL. The measurement of the crack propagation in rock slabs, in: Proceedings of the 2004 ISRM International Symposium: 3rd Asian Rock Mechanics Symposium, Kyoto, Japan, 341-346, 2004.
 21. Sahin S, Yayla P. Effects of testing parameters on the mechanical properties of polypropylene random copolymer. Polymer Testing 24 (2005) 613-619.
 22. Liang CY, Zhang QB, Li X, Xin P. The effect of specimen shape and strain rate on uniaxial compressive behavior of rock material. Bulletin of Engineering Geology and the Environment 72 (2016) 1669-1681.
 23. Hoek E, Bieniawski ZT. Brittle rock fracture propagation in rock under compression. Int. Journal of Fracture Mechanics 1 (1965) 137-155.
 24. Atkinson C, Cook JM. Effect of loading rate on crack propagation under compressive stress in a saturated porous material. Journal of Geophysical Research 98 (1993) 6383-6395.
 25. Goldston M, Remennikov A, Neaz Sheikh M. Experimental investigation of the behaviour of concrete beams reinforced with GFRP bars under static and impact loading. Engineering Structures 113 (2016) 220-232.
 26. Komurlu E, Kesimal A. Evaluation of Indirect Tensile Strength of Rocks using Different Types of Jaws. Rock Mechanics and Rock Engineering 48 (2015) 1723-1730.
 27. Cardu M, Giraudi A, Rocca V, Verga F. Experimental laboratory tests focused on rock characterisation for mechanical excavation. International Journal of Mining Reclamation and Environment 26 (2012) 199-216.
 28. Basarir H, Karpuz C. Preliminary estimation of rock mass strength using diamond bit drilling operational parameters. International Journal of Mining Reclamation and Environment 30 (2016) 145-164.
 29. Komurlu E, Cihangir F, Kesimal A, Demir S. Effect of Adhesive Type on the Measurement of Modulus of Elasticity Using Electrical Resistance Strain Gauges. Arabian Journal for Science and Engineering 41 (2016) 433-441.
 30. Chen R, Xia K, Dai F, Lu F, Luo SN. Determination of dynamic fracture parameters using a semi-circular bend technique in split Hopkinson pressure bar testing. Engineering Fracture Mechanics 76 (2009) 1268-1276.
 31. Zhang QB. Mechanical Behaviour of Rock Materials under Dynamic Loading, PhD Thesis. Swiss Federal Institute of Technology in Lausanne, Lausanne, 2014.
 32. Osovski S, Srivastava A, Ponson L, Bouchaud E, Tvergaard V, Ravichandar K, Needleman A. The effect of loading rate on ductile fracture toughness and fracture surface roughness. Journal of the Mechanics and Physics of Solids 76 (2015) 20-46.
 33. Murthy ARC, Palani GS, Iyer NR. State-of-the-art review on fracture analysis of concrete structural component. Sadhana 34 (2009) 345-367.
 34. Ergun A, Alpsar M, Elmaci E, Halıcılar G, İnal HS, İşçen Hİ, Öğün O, Özkazanç MO, Patır O. Explosives and Blasting Techniques (in Turkish). Nitromak Education Publications, Ankara, 2012.
 35. Wang Z, Fang C, Chen Y, Cheng W. A comparative study of delay time identification by vibration energy analysis in millisecond blasting. International Journal of Rock Mechanics and Mining Sciences 60 (2013) 389-400.
 36. Johansson D, Ouchterlony F. Shock wave interactions in rock blasting: the use of short delays to improve fragmentation in model-scale. Rock Mechanics and Rock Engineering 46 (2013) 1-18.
 37. Uyar Aldas GG. Explosive charge mass and peak particle velocity (PPV)-frequency relation in mining blast. Journal of Geophysics and Engineering 7 (2010) 223-231.
 38. Uyar Aldas GG. Investigation of blast design parameters from the point of seismic signals. International Journal of Mining Reclamation and Environment 24 (2010) 80-90.
 39. Lucon E. Estimating dynamic ultimate tensile strength from instrumented Charpy data. Materials & Design 97 (2016) 437-443.
 40. Lowe LA. Factors influencing accuracy of Charpy impact test data, in: Charpy impact test: Factors and Variables (ed. by Holt, M). ASTM Publication, Chelsea, Michigan, 1990.
 41. Shukla A. Comparison of static and dynamic energy release rates for different fracture specimens. Engineering Fracture Mechanics 18 (1983) 725-730.
 42. Zhang ZX. Estimate of Loading Rate for a TBM Machine Based on Measured Cutter Forces. Rock Mechanics and Rock Engineering 37 (2004) 239-248.
 43. Hemphill GB. Practical Tunnel Construction. John Wiley & Sons, New Jersey, 2013.
 44. Bazant PZ, Bai SP, Gettu R. Fracture of rock: effect of loading rate. Engineering Fracture Mechanics 45 (1993) 393-398.
 45. Bertram A, Kalthoff JF. Fracture toughness of fast propagating cracks in rock. Available from: <https://www.researchgate.net/publication/267948043>, 2005.
 46. Zhang QB, Zhao J. A Review of Dynamic Experimental Techniques and Mechanical Behaviour of Rock Materials. Rock Mechanics and Rock Engineering 47 (2014) 1411-1478.
 47. Kharchenko VV, Kondryakov EA, Zhmaka VN, Babutskii AA, Babutskii AI. The effect of temperature and loading rate on the crack initiation and propagation energy in carbon steel Charpy specimens. Strength of Materials 38 (2006) 535-541.
 48. Zou, C.; Wong, L.N.Y. Experimental studies on cracking processes and failure in marble under dynamic loading. Engineering Geology 173 (2014) 19-31.
 49. Komurlu, E.; Kesimal, A.; Demir, S. Determination of Indirect (Splitting) Tensile Strength of Cemented Paste Backfill Materials. Geomechanics and Engineering 10 (2016) 775-791.
 50. Durif E, Réthoré J, Combescure A, Fregonese M, Chaudet P. Controlling Stress Intensity Factors During a Fatigue Crack Propagation Using Digital Image Correlation and a Load Shedding Procedure. Experimental Mechanics 52 (2012) 1021-1031.

Thermodynamic Optimization of Turbine Lines for Maximum Exergy Efficiency in a Binary Geothermal Power Plant

Ali Kecebas 

Department of Energy Systems Engineering, Mugla Sıtkı Kocman University, Mugla, Turkey.

ABSTRACT

For engineering applications related to techniques that optimize power plants or thermal systems, optimization techniques are very important. Power plants with wasted geothermal resources and inefficient organic Rankine cycle (ORC) attract the attention of researchers, engineers and decision-makers. In this study, the pressure and mass flow rates on turbine lines are optimized to maximize exergy efficiency in a binary ORC geothermal power plant (GPP). With this aim, initially data collected from a real operating GPP are used to simulate the system. Then an artificial bee colony (ABC) algorithm is developed for this model. The results showed that, the total exergy efficiency of the system was 35.25% while its value increased with the ABC optimization in the maximum possible exergy efficiency of 38.45%. Optimizing the turbine lines in the system ensured improvement rate of 4-6% for the turbines. As a result, the thermodynamic performance of the system is estimated at the same moment and with reasonable accuracy, it can be ensured that the physical process used for improvements is better understood.

Keywords:

Geothermal energy; ORC; Turbine; Exergy efficiency; Optimization

Article History:

Received: 2017/11/24

Accepted: 2019/01/01

Online: 2019/02/05

Correspondence to: Ali Kecebas,
Department of Energy Systems
Engineering, Mugla Sıtkı Kocman
University, Mugla, Turkey
E-mail: alikecebas@mu.edu.tr;
Phone: +90 252 211 5471.

INTRODUCTION

In recent years due to the limited production and lifetime of fossil resources on earth, and their effects on the health of organisms and climate, awareness of renewable energy resources like geothermal energy has increased worldwide. Considering the issues mentioned in terms of Turkey, the importance of geothermal energy as renewable energy is obvious. Geothermal energy is a clean, safe and reliable source of renewable energy [1]. Generally high temperature resources ($T > 150$ °C) are used for electricity production, while moderate (90 °C $< T < 150$ °C) and low ($T < 90$ °C) temperature resources are used in more direct use areas. In recent times, very low temperature resources ($T < 35$ °C) have been used in heat pump applications. The situation in Turkey is that moderate and high temperature resources and, due to the large profit margin, electricity production from these resources are chosen more often compared to other uses. The results clearly show that the installed power from

geothermal energy in Turkey has risen from 624 MW in 2015 to 821 MW in 2016. According to the Turkish Energy Atlas, Turkey contains 32 geothermal power plants (GPPs) with a total installed power of 921.5 MW and this is corresponding to 1.2% of the 78497.4 MW installed power in Turkey at the end of 2016 [2].

Currently with advanced level development of GPPs, the total geothermal installed power globally has reached 12640 MW [3]. This installed power comprises 5079 MW from single flash cycle, 2863 MW from dry steam, 2544 MW from double flash, 1790 MW from binary, 182 MW from triple flash and 181 MW from back-pressure cycle and hybrid cycle. However, in Turkey 198 MW of the installed power comes from binary cycle, 178 MW from double flash and 20 MW from single flash [3]. In Turkey it appears that binary organic Rankine cycle (ORC) are used more often than the other cycles. As a result, the design of a power plant is often a function

of the temperature and pressure of the existing geothermal resource. Thus, to meet the increasing electricity demands globally and in Turkey, geothermal power continues to develop while engineers and policy makers desire data about feasibility and optimum design of GPPs within a spectrum of geothermal resource conditions and climates. Because of this reason, there is a need for scientifically prepared design, analysis and optimization guidelines.

After the petrol crisis occurring in the 1970s, it was understood that energy analysis alone did not determine how effectively energy is used. Thus, exergy analyses began to gain significant importance. İleri and Gürer [4] brought the energy use in addition to exergy use in Turkey up to 1995 to the agenda. The results of their study revealed how inefficient an apparently efficient system is when exergy analysis is completed.

When the literature about thermodynamic modelling and optimization of ORC is scanned, the following studies are found. To assess system performance, Wei et al. [5] presented a dynamic model to be used for design of an ORC system using waste heat recovery (WHR) with HFC-245fa as working fluid. The simulation software for this dynamic model was developed based on the platform of Modelica/Dymola. When the ambient temperature was too high, they concluded that net power and efficiency of the system deteriorated. Another study by Wei et al. [6] compared two model approaches based on moving boundaries and discretization techniques on the model developed for the same system under accuracy, complexity and simulation speed parameters. Rashidi et al. [7] conducted an optimization process for regenerative ORC with two feed water heaters for exergy efficiency and specific work by using artificial neural network (ANN) and artificial bee colony (ABC) algorithms. Sun et al. [8] proposed a ROSENB optimization algorithm to maximize the net power generation or the thermal efficiency of an ORC power plant with WHR. The effects of mass flow rates of working fluid and air-cooled condenser fans and inlet pressure of expander on thermal efficiency and net power generation of the system were investigated. Zhang et al. [9] recommended a multivariate control strategy for ORCs with WHR by combining a PI controller with a linear quadratic regulator to ensure both temporary performance and stable state energy saving. Bamgbopa and Uzgoren [10,11] developed a strategy using a finite volume approach to set evaporator flow rates to ensure stable working of a solar ORC power plant. Both stable and temporary models were developed for the system components (as pump, evaporator, expander and condenser). The model compared reasonable benchmarking numerical and experimental data in situations where the thermal inputs of the basic assumptions changed over time. The critical component of the system was determined to be the evaporator.

However, in the literature there are very few optimization studies for ORC cycles used with geothermal resources. Clarke et al. [12] compared the performance of a genetic algorithm (GA) with that of a particle swarm optimization (PSO) for constrained, nonlinear, simulation-based optimization of a double flash GPP. Another study by Clarke and McLeskey Jr. [13] used a PSO with Pareto-optimal set to determine the optimum use of a super heater and/or recuperator for a binary GPP at environmental and geothermal fluid temperatures. Saffari et al. [14] used an ABC optimization algorithm to optimize the thermal efficiency of a binary turbine based Kalina cycle with low-temperature. Additionally, the study researched the effects of separator input pressure and temperature, basic ammonia mass fraction and basic mass flow rate of working fluid on net power output and thermal efficiency of the cycle. Another study by Saffari et al. [15] compared the ABC, GA, PSO and differential evolution (DE) methods for the thermodynamic performance of the Husaviv power plant with geothermal Kalina cycle. They reported that ABC was more useful compared to the other methods. Proctor et al. [16] used the VMGSim simulation program to develop a dynamic model for a flash ORC GPP in New Zealand and confirmed it with real data from the power plant. Li et al. [17] performed an off-design performance analysis for a geothermal resource-based Kalina cycle with a thermodynamic platform (developed by Matlab and NIST Refprop). They used GA to maximize the net output power and to determine the thermodynamic parameters in the design stage. Wu et al. [18] optimized the thermodynamic performance of a GPP with trans critic ORC using CO₂-based binary zeotropic mixtures. They optimized the thermodynamic performance of the system using the pattern search algorithm (PSA) for 6 refrigerant mixtures in which CO₂ could be added. Thermodynamic and economic analyses were also completed.

As can be seen in the above literature review, the artificial bee colony (ABC) algorithm has not been used for optimization of parameters (pressure and mass flow rate) on system turbine lines to maximize exergy efficiency of a binary GPP. Additionally, the effects of the turbine line on other components of the system have not been researched. In this study, these original issues mentioned have been addressed. Firstly, the thermodynamic performance of the system and its components are assessed with exergy analysis. Then the parameters on the turbine line of the system are optimized with the ABC algorithm to maximize the thermodynamic performance of the system.

DESCRIPTION OF THE SYSTEM

As illustrated in Fig. 1, a geothermal power plant (GPP) with installed power of 24 MW operates in compliance with an air-cooled binary geothermal organic Rankine

cycle (ORC). In the GPP, to ensure mixing of the artesian geothermal fluid obtained from production wells, a vertical separator in each wellhead separates two phases as geothermal fluid and steam. From the separators, first 30% NCG (non-condensable gases) and nearly 70% geothermal fluid steam is obtained. Then liquid geothermal fluid is obtained from the separators.

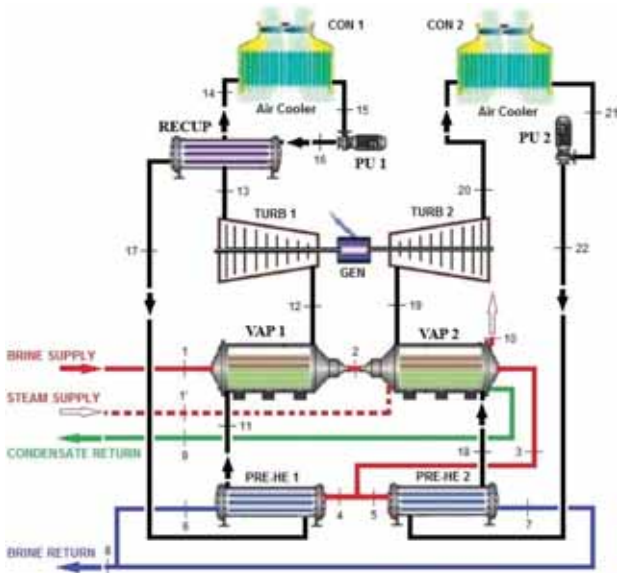


Figure 1. Schematic flow diagram of a geothermal power plant

As seen in Fig. 1, this section is outside the scope of the study, which only includes the power plant section. Binary ORC consists of two classic Rankine cycles that are side by side and different from each other. The first cycle with 160 kg/s is called level I (high pressure), while the second cycle with 196 kg/s is called level II (low pressure). The liquid geothermal fluid first passes through level I and then level II. However, due to the low temperature and pressure, the geothermal fluid steam produced from the separators is passed to level II. The geothermal fluid from both levels is pumped to re-injection wells. In both separate ORC levels, pentane as organic working fluid is used. In level I, different to level II, a recuperator is used to reduce the effect of the high temperature from the turbine output on the condenser.

Additionally, the turbines in levels I and II balance the generator in a certain cycle. Some of the electricity produced by the GPP is used to sustain the system, while the rest of generated electricity is transmitted to switchyard and to the interconnected power lines. In this study, the real operational data of temperature, pressure and mass flow rates for exergy analysis and optimization processes were collected from a GPP belonging to Maren Geothermal Inc. on 14 April 2013. The operating data belonging to the GPP on this date are listed in Table 1.

Table 1. The thermodynamics variables for line numbers on the system flow diagram illustrated in Fig. 1.

Line, <i>i</i>	<i>T</i> (<i>i</i>) [°C]	<i>P</i> (<i>i</i>) [kPa]	<i>m</i> (<i>i</i>) [kg/s]	<i>Ẋ</i> (<i>i</i>) [kW]
0	25	101		
1	164	1040	445	47507
1'	165	1040	5.83	631
1''	165	1040	2.50	382
2	136	730	445	31701
3	110	690	445	19174
4	110	690	222.50	9587
5	110	690	222.50	9587
6	89	590	222.50	5681
7	81	570	222.50	4423
8	85	590	445	9910
9	107	690	0.83	34
10	107	690	5.25	214
10	107	690	2.25	259
11	105	1261	160	4080
12	137	1261	160	18508
13	82	150	160	5581
14	60	150	160	4675
15	31	150	160	89
16	37	1261	160	388
17	55	1261	160	855
18	106	687	169	4270
19	109	687	169	14859
20	69	119	169	4013
21	33	119	169	117
22	39	687	169	278
23	18	101	2000	0
24	19	106	2000	8238
25	18	101	2000	0
26	19	106	2000	8238

MASS, ENERGY AND EXERGY ANALYSES

For thermodynamic modelling of a binary GPP with ORC, the following assumptions were used in the study:

- Steady-state and steady-flow conditions are used.
- Potential and kinetic energy changes are negligible.
- Heat losses of system components are negligible.
- Pressure loss in valves and pipes is negligible.
- The thermodynamic properties of water are used in place of geothermal fluid properties.
- The air is accepted as an ideal gas.

- In condensers the air has homogeneous distribution.
- Isentropic efficiencies of turbines, pumps and fans are fixed for the thermodynamic model and optimization process. In Level I and II, the values are 0.92 and 0.81 for turbines, and 0.96 and 0.97 for pumps, respectively.
- For level I and II, the effectiveness of vaporizers is 0.82 and 0.88, respectively.
- For level I and II, the effectiveness of preheaters is 0.92 and 0.95, respectively.
- For level I and II, the effectiveness of condensers is 0.68 and 0.75, respectively.
- The effectiveness of the recuperator is 0.49 for only level I.
- The reference state temperature and pressure are taken to be 25 °C and 101.325 kPa, respectively.

For a system, in general the mass, energy and exergy balances express as follows.

$$\sum \dot{m}_{out} - \sum \dot{m}_{in} = 0 \quad (1)$$

$$\dot{Q} - \dot{W} = \sum \dot{m}_{out} h_{out} - \sum \dot{m}_{in} h_{in} \quad (2)$$

$$\dot{I} = \sum \left(1 - \frac{T_0}{T_k} \right) \dot{Q}_k - \dot{W} + \sum \dot{m}_{in} \psi_{in} - \sum \dot{m}_{out} \psi_{out} \quad (3)$$

where \dot{m} , \dot{Q} , \dot{W} , h and \dot{I} denote the mass flow rate, heat rate, work rate, specific enthalpy and exergy destruction, respectively. \dot{Q}_k is the heat transfer rate crossing the boundary at temperature T_k at location k . The subscript 0 indicates properties at the restricted dead state of P_0 and T_0 , and ψ is the specific flow exergy as expressed below:

$$\psi = (h - h_0) - T_0(s - s_0) \quad (4)$$

where s denotes the entropy.

Using the data listed in Table 1, the above-mentioned assumptions and thermodynamic balance equations, a code is developed on the MATLAB program [19] platform. The thermodynamic properties of water, air and n-pentane in the developed code are provided by the COOLPROP program [20,21]. In the literature, there are many studies on thermodynamic modelling of binary GPP with ORC [22-25]. However, for the sake of simplicity, the thermodynamic balance equations at the component level used in the thermodynamic model of the system are not given in the text.

ARTIFICIAL BEE COLONY AS OPTIMIZATION ALGORITHM

Optimization algorithms are used in the majority of energy system applications. In this study, the artificial bee colony (ABC) developed by Karaboğa [26] to determine the optimum exergy efficiency of a thermal system

is used. This optimization algorithm simulates the intelligent food search behavior of bee colonies [27]. Thus, it attempts to iteratively find the point providing the problem's minimum or maximum solution in space. As an optimization method for the majority of multi modal/ dimensional and multipurpose problems, the ABC algorithm contains fewer control parameters and provides better or equal performance than other optimization methods [14,15,28,29].

The optimization process of the ABC algorithm comprises the following steps [27,30-32]:

1. It occurs by generating a random value between the upper and lower limits of each parameter using Eq. (5). In this situation the ABC algorithm randomly produces the first solutions to the problem. Random values are produced between the lower and upper limits for each parameter as in the follow.

$$x_{ij} = x_j^{\min} + rand(0,1)(x_j^{\max} - x_j^{\min}) \quad \begin{cases} i = 1, \dots, SN \\ j = 1, \dots, D \end{cases} \quad (5)$$

where SN and D denote the food sources number and the parameters number to be optimized, respectively.

2. After finding food sources, worker bees then begin to carry nectar to the hive. The number of worker bees assigned represents the cost function ($fi=f(xi)$) of each (xi) solution. A fitness value (fit) is calculated for the solution to the problem within the limits as given in:

$$fit_i = \begin{cases} \frac{1}{1 + f_i}, & f_i \geq 0 \\ 1 + |f_i|, & f_i < 0 \end{cases} \quad (6)$$

3. Then each worker bee provides information to observer bees about the state of the food source (is the food source abundant or is a new source needed). This information is provided through dance displayed in the dance area [33]. In the basic ABC algorithm, this is fulfilled using a roulette wheel selection process linked to the fit value [34]. This is presented in the below.

$$p_i = \frac{fit_i}{\sum_{i=1}^{SN} fit_i} \quad (7)$$

4. If the source is consumed, the explorer bee is directed to search for a new source. The worker bee determines a new food source near the food source it is working and assesses its quality. The new source is stored in memory if the new source is better. The simulation of determination of new sources adjacent to current sources is given by

$$v_{ij} = x_{ij} + \phi_{ij}(x_{ij} - x_{kj}) \quad \begin{cases} j = 1, 2, \dots, SN \\ k = 1, 2, \dots, SN \end{cases} \quad (8)$$

where ϕ is a random number in range of [-1,1] and $j \neq k$. The difference between the random values of x_{ij} and x_{kj} decreases; in this instance, solutions become more similar. Therefore, the amount of variation in the x_{ij} parameter diminishes. A greedy selection process is applied related to the nectar amounts of x_i and v_i as the fit value [34]. The nectar amount from the new v_i solution is higher than the previous amount (x_i), thus the old one is deleted from the memory of the worker bee, and the newly v_i source is stored.

5. In the ABC algorithm, a repetitive optimization process continues until the required solution is obtained.

The parameters used in the ABC algorithm are listed in Table 2. In Table 2, the optimized number of parameters (D) is 1 and the single target function is the total exergy efficiency of the system. Within these parameters, there are a total of 4 decision variable parameters of the 2 turbine output pressures on the turbine line and the 2 mass flow rates for the working fluid on level I and level II. The minimum and maximum limits for these decision variables are presented in Table 2. The ABC algorithm parameters for the optimization process are set to the parameters in Table 2. In conclusion, an attempt was made to find appropriate results by repeating each optimization process at least once.

Table 2. The parameters of the ABC algorithm.

Parameters	Symbol	Value or Unit	Constraint range
Number of colony size	NP		20
Number of food sources	Food number		20
Food source which could not be improved though trials	Limit		100
Number of cycles for foraging	Max cycle		100
Number of parameters to be optimized (for single objective)	D		1
Turbine outlet pressure at level I	P_{13}	kPa	159.6–161.6
Turbine outlet pressure at level II	P_{20}	kPa	167–172
Mass flow rate of n-pentane at level I	\dot{m}_{12}	kg/s	115–185
Mass flow rate of n-pentane at level II	\dot{m}_{19}	kg/s	90–150

In thermodynamic evaluation (ExA), the exergy efficiency in system and component levels can respectively be expressed as

$$\varepsilon_{sys} = 1 - \frac{\dot{I}_{sys}}{\dot{E}x_{in,sys}} \quad (\text{single objective function}) \quad (9)$$

and

$$\varepsilon_k = 1 - \frac{\dot{I}_k}{\dot{E}x_{in,k}} \quad (10)$$

In the optimization process (ABC algorithm), the maximum possible exergy efficiency in system and component levels can respectively be given as

$$\varepsilon_{\max \text{ possible, sys}} = 1 - \frac{\dot{I}_{sys, \min}}{\dot{E}x_{in, sys}} \quad (11)$$

and

$$\varepsilon_{\max \text{ possible, k}} = 1 - \frac{\dot{I}_{k, \min}}{\dot{E}x_{in, k}} \quad (12)$$

RESULTS AND DISCUSSION

Primarily, exergy analysis (ExA) is considered to assess the effect of the turbines on maximum exergy efficiency in a binary GPP system. The results obtained from exergy analysis are listed in Table 3. Regarding Table 3, nearly 17101 kW of the total exergy input into the system is the exergy destruction rate due to components in the whole system. The highest exergy destruction rate in the system occurs in condenser CON 2 with 3342 kW. This is followed by condenser CON 1, vaporizer VAP 2 and turbine TURB 2 with 3251 kW, 2443 kW and 1840 kW, respectively. The exergy destruction rate for turbine TURB 1 is calculated as 871 kW. The components mentioned above are the components that require priority improvement to maximize the performance of the system. As can be seen in Table 3, the total exergy efficiency of the system is 35.25%. This value is the single objective function chosen for the optimization process.

Table 3. The exergetic variables for the system and its components.

Component, k	$\dot{I}(k)$ [kW]	ε (sys) [%]
Level I		
PRE-HE 1	681.90	
VAP 1	1378.46	
TURB 1	871.37	
RECUP	438.10	
CON 1	3251.48	
PU 1	611.68	
Level II		
PRE-HE 2	1171.77	
VAP 2	2443.01	
TURB 2	1840.19	
CON 2	3342.00	
PU 2	1070.67	
Overall system, sys	17100.63	17100.63

The artificial bee colony (ABC) algorithm is used to maximize the total exergy efficiency of the system. Therefore, the real and optimum values for the selected decision variables along the two turbine lines are given in Table 4. It can be observed from Table 4 that the collected values for output pressure from the turbines are close to the optimum values, while the mass flow rates collected from the turbine

lines are distant from the optimum values. For example, the collected value for \dot{m}_{19} was 119 kg/s, while the optimized value was nearly 149 kg/s. As a result, if the decision variables can reach the optimum values, the exergy efficiency of the whole system will reach maximum.

Table 4. The collected and optimized values of the decision variables for the turbine lines.

Decision variables	Collected value	Optimum value
P_{13} - Turbine outlet pressure at level I	160	159.96
P_{20} - Turbine outlet pressure at level II	169	167.73
\dot{m}_{12} - Mass flow rate of n-pentane at level I	150	161.20
\dot{m}_{19} - Mass flow rate of n-pentane at level II	119	148.54

The convergence behavior of the ABC algorithm during the maximizing process (optimization) of the exergy efficiency of the system is shown in Fig. 2. Regarding Fig. 2, the total exergy efficiency of the system is maximized in the third cycle. As seen on Fig. 3, the total exergy efficiency of the system is 35.25%. The results of optimization process with the ABC algorithm can increase this value to 38.45%. This value is called as the maximum possible exergy efficiency (ϵ_{\max} possible).

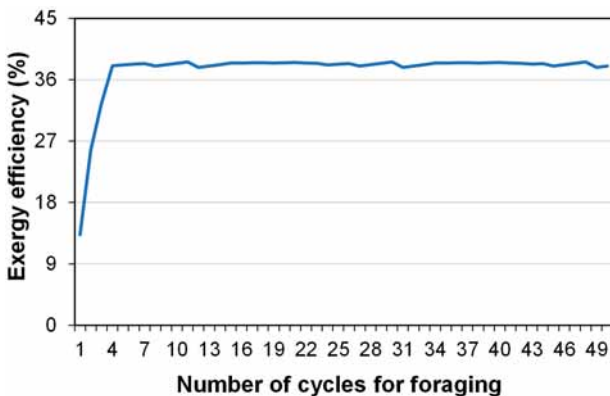


Figure 2. Convergence behavior of the ABC algorithm for optimization process

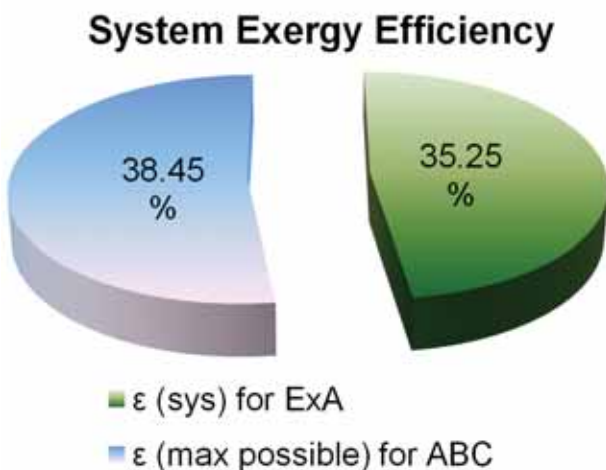


Figure 3. Total system exergy efficiency for the ExA and ABC methods

For the exergy analysis and the ABC algorithm, the changes of exergy destruction rates of system components in the GPP are presented in Fig. 4. From Fig. 4, on the route to maximize the total exergy efficiency, the exergy destruction results for system components with ABC optimization completed for decision variables chosen on the turbine line is observed to lower the exergy analysis results even further. As seen on Fig. 4, condensers CON 1 and CON 2 have highest exergy destruction rates. These values are 3342 kW and 3251 kW, respectively, while after the optimization process these values may be lowered to 2535 kW and 1675 kW. Additionally, these are the components with greatest reductions among system components of 24% and 48%, respectively. However, the result of the optimization process causes a 21% increase in the exergy destruction rate due to the recuperator RECUP. The effects of the optimization process on other system components may be observed.

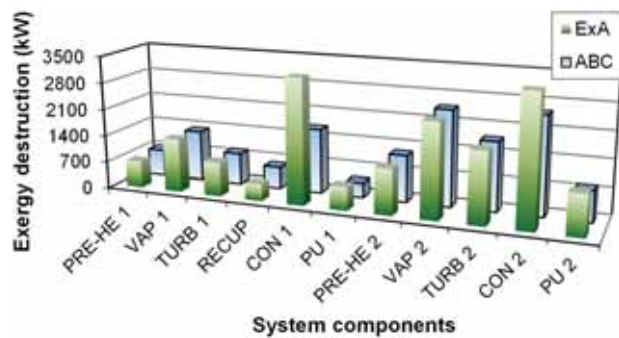


Figure 4. Changes in exergy destruction rate of the system components

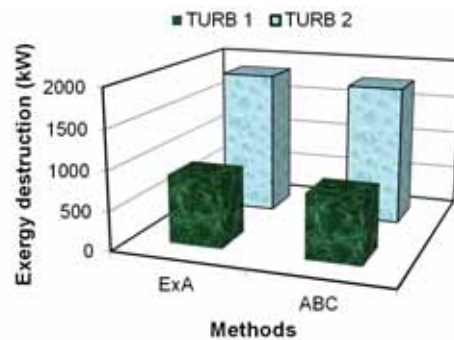


Figure 5. Changes in exergy destruction rate of the turbines in level I and II

Referring to Fig. 5, the exergy destruction rates for turbines TURB 1 and TURB 2 are 871 kW and 1840 kW, respectively, while these values could only be optimized by 6% and 4% (816 kW and 1773 kW). With the ABC optimization process, the exergy destruction rates from turbines are reduced though by a small value, as clearly seen on Fig. 5.

Fig. 6 shows the variation in maximum possible exergy efficiency for system components obtained from the ABC optimization process. As seen on the figure, when the ABC optimization process is completed, the exergy efficiency values for all system components are high, apart from the

recuperator. This means that optimization processes completed on the turbine lines in the system will only produce maximum possible exergy efficiency for system components. As observed on Fig. 6, the greatest increase in exergy efficiency occurs in the condensers with 31% for CON 2 and 30% for CON 1. However, there is a 14% reduction in exergy efficiency observed for the recuperator RECUP. In Fig. 7, the variation in exergy efficiency of the turbines on level I and II is given. While the exergy efficiency for turbines TURB 1 and TURB 2 were 93.26% and 83.03%, respectively, after optimization of the system turbine lines the maximum possible exergy efficiencies were observed to be 93.45% and 83.47%.

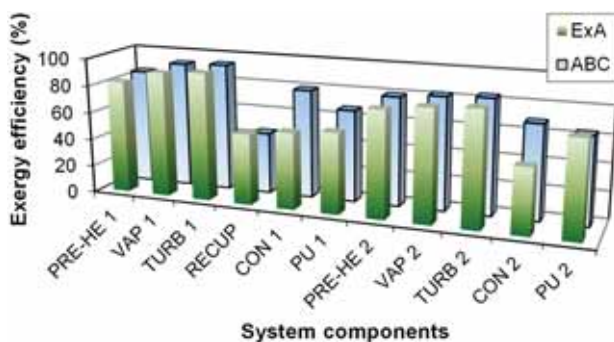


Figure 6. Changes in exergy efficiency of the system components

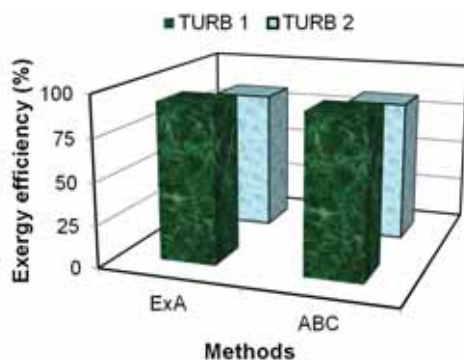


Figure 7. Changes in exergy efficiency of the turbines in level I and II

Finally, to maximize the total exergy efficiency of a binary GPP, the mass flow rates and turbine output pressures for the working fluid are optimized on level I and level II. The results of the optimization process found that the flow rates and turbine output pressures in the cycle levels should be larger than the operating system values.

CONCLUSION

In this study, the artificial bee colony (ABC) algorithm is used to maximize the total exergy efficiency of a binary GPP with ORC. For the optimization process, decision variables on the turbine lines of level I and II of the system are used. These variables are mass flow rate and the turbine output pressure of the working fluid on the turbine lines. The results of the study show that the total exergy efficiency and maximum possible exergy efficiency of

the system were 35.25% and 38.45%, respectively. While the total exergy destruction rate for system components was 17101 kW, with the ABC algorithm this value could be lowered to 14227 kW. As a difference of these values, more exergy may be produced at 2874 kW. While improving system components, the system components with greatest optimization possible are the condensers CON 2 and CON 1. Optimizing the turbine lines in the system with the ABC optimization algorithm ensures improvement rates of 4-6% for the turbines. Thus, the rotational imbalances that occur in the connection of two turbines to the generator with the same shaft in binary cycles and the quality of steam content at the turbine outlet to prevent corrosion in turbine blades may be improved. Finally, the ABC optimization method can provide higher quality information than the exergy analysis.

ACKNOWLEDGEMENTS

The authors gratefully acknowledges the support provided by the Maren Geothermal Inc.

NOMENCLATURE

D	number of parameters to be optimized
(-)	
$\dot{E}x$	exergy rate (kW)
f	cost function (-)
fit	fitness value (-)
h	specific enthalpy (kJ/kg)
\dot{I}	exergy destruction (kW)
\dot{m}	mass flow rate (kg/s)
NP	number of colony size (-)
P	pressure (kPa)
\dot{Q}	heat transfer rate (kW)
s	specific entropy (kJ/kgK)
SN	number of food sources (-)
T	temperature ($^{\circ}$ C or K)
\dot{W}	work rate, power (kW)

Greek symbols

ϵ	exergy or second law efficiency (%)
ϕ	random number [-1,1]
ψ	flow exergy (kJ/kg)

Subscripts

in	input
min	minimum
out	output
sys	system
0	reference state

Abbreviations

ABC	artificial bee colony
ANN	artificial neural network
ExA	exergy analysis
CON	condenser
GPP	geothermal power plant
NCG	non-condensable gases
ORC	organic Rankine cycle
PRE-HE	preheater
PU	pump
RECUP	recuperator
TURB	turbine
VAP	vaporizer
WHR	waste heat recovery

References

- Schiel K, Baume O, Carus G, Leopold U. GIS-based modelling of shallow geothermal energy potential for CO₂ emission mitigation in urban areas. *Renewable Energy* 86 (2016) 1023-36.
- TEIAS. Turkish Electricity Transmission Corporation, <http://www.teias.gov.tr/>, Accessed date: 15.04.2017.
- Bertani R. Geothermal power generation in the world 2010-2014 update report. *Geothermics* 60 (2016) 31-43.
- Ileri A, Güler T. Energy and exergy utilization in Turkey during 1995. *Energy* 23 (1998) 1099-106.
- Wei D, Lu X, Lu Z, Gu J. Performance analysis and optimization of organic Rankine cycle (ORC) for waste heat recovery. *Energy Conversion and Management* 48 (2007) 1113-9.
- Wei D, Lu X, Lu Z, Gu J. Dynamic modeling and simulation of an organic Rankine cycle (ORC) system for waste heat recovery. *Applied Thermal Engineering* 28 (2008) 1216-24.
- Rashidi MM, Galanis N, Nazari F, Parsa AB, Shamekhi L. Parametric analysis and optimization of regenerative Clausius and organic Rankine cycles with two feed water heaters using artificial bees colony and artificial neural network. *Energy* 36 (2011) 5728-40.
- Sun J, Li WH. Operation optimization of an organic Rankine cycle (ORC) heat recovery power plant. *Applied Thermal Engineering* 31 (2011) 2032-41.
- Zhang J, Zhang W, Hou G, Fang F. Dynamic modeling and multivariable control of organic Rankine cycles in waste heat utilizing processes. *Computers and Mathematics with Applications* 64 (2012) 908-21.
- Bamgbopa MO, Uzgoren E. Numerical analysis of an organic Rankine cycle under steady and variable heat input. *Applied Energy* 107 (2013) 219-28.
- Bamgbopa MO, Uzgoren E. Quasi-dynamic model for an organic Rankine cycle. *Energy Conversion and Management* 72 (2013) 117-24.
- Clarke J, McLay L, McLeskey Jr JT. Comparison of genetic algorithm to particle swarm for constrained simulation-based optimization of a geothermal power plant. *Advanced Engineering Informatics* 28 (2014) 81-90.
- Clarke J, McLeskey Jr JT. Multi-objective particle swarm optimization of binary geothermal power plants. *Applied Energy* 138 (2015) 302-14.
- Sadeghi S, Saffari H, Bahadormanesh N. Optimization of a modified double-turbine Kalina cycle by using Artificial Bee Colony algorithm. *Applied Thermal Engineering* 91 (2015) 19-32.
- Saffari H, Sadeghi S, Khoshzat M, Mehregan P. Thermodynamic analysis and optimization of a geothermal Kalina cycle system using Artificial Bee Colony algorithm. *Renewable Energy* 89 (2016) 154-67.
- Proctor MJ, Yu W, Kirkpatrick RD, Young BR. Dynamic modelling and validation of a commercial scale geothermal organic Rankine cycle power plant. *Geothermics* 61 (2016) 63-74.
- Li H, Hu D, Wang M, Dai Y. Off-design performance analysis of Kalina cycle for low temperature geothermal source. *Applied Thermal Engineering* 107 (2016) 728-37.
- Wu C, Wang SS, Jiang X, Li J. Thermodynamic analysis and performance optimization of transcritical power cycles using CO₂-based binary zeotropic mixtures as working fluids for geothermal power plants. *Applied Thermal Engineering* 115 (2017) 292-304.
- MathWorks, Matlab, <http://www.mathworks.com/products/matlab/>, Accessed date: 15.04.2017.
- Bell IH, Quoilin S, Wronski J, Lemort V. CoolProp: an open-source reference quality thermophysical property library, in: ASME ORC 2nd International Seminar on ORC Power Systems, Rotterdam, Netherlands; (2013).
- Bell IH, Wronski J, Quoilin S, Lemort V. Pure and pseudo-pure fluid thermophysical property evaluation and the open-source thermophysical property library coolprop. *Industrial and Engineering Chemistry Research*, 53 (6) (2014) 2498-508.
- Kanoglu M, Bolattürk A. Performance and parametric investigation of a binary geothermal power plant by exergy. *Renewable Energy* 33 (11) (2008) 2366-74.
- Keçebaş A, Gökgedik H. Thermodynamic evaluation of a geothermal power plant for advanced exergy analysis. *Energy* 88 (2015) 746-55.
- Gökgedik H, Yürüsoy M, Keçebaş A. Improvement potential of a real geothermal power plant using advanced exergy analysis. *Energy* 112 (2016) 254-63.
- Koroneos C, Polyzakis A, Xydis G, Stylos N, Nanaki E. Exergy analysis for a proposed binary geothermal power plant in Nisyros Island, Greece. *Geothermics* 70 (2017) 38-46.
- Karaboga D. An ideal based on honey bee swarm for numerical optimization, Technical Report - TR06, Erciyes University, Engineering Faculty, Department of Computer Engineering, Kayseri, Turkey; (2005).
- Karaboga D, Akay B. A comparative study of Artificial Bee Colony algorithm. *Applied Mathematics and Computation* 214 (1) (2009) 108-32.
- Uzlu E, Akpınar A, Öztürk HT, Nacar S, Kankal M. Estimates of hydroelectric generation using neural networks with the Artificial Bee Colony algorithm for Turkey. *Energy* 69 (2014) 638-47.
- Delgarm N, Sajadi B, Delgarm S. Multi-objective optimization of building energy performance and indoor thermal comfort: A new method using Artificial Bee Colony (ABC). *Energy and Buildings* 131 (2016) 42-53.
- Karaboga D, Ozturk C. A novel clustering approach: Artificial

- Bee Colony (ABC) algorithm. *Applied Soft Computation* 11 (1) (2011) 652-57.
31. Baykasoglu A, Ozbakir L, Tapkan P. Artificial Bee Colony algorithm and its application to generalized assignment problem, in: F.T.S. Chan, M.K. Tiwari (Eds.), *Swarm Intelligence: Focus on Ant and Particle Swarm Optimization*, ITech Education and Publishing, Vienna, Austria; (2007) pp. 113-44.
 32. Karaboga D, Basturk B. A powerful and efficient algorithm for numerical function optimization: Artificial Bee Colony (ABC) algorithm. *Journal of Global Optimization* 39 (3) (2007) 459-71.
 33. Karaboga D, Basturk B. Artificial Bee Colony (ABC) optimization algorithm for solving constrained optimization problems. *Foundations of Fuzzy Logic and Soft Computing* 4529 (2007) 789-98.
 34. Dhahri H, Alimi AM, Abraham A. Designing beta basis function neural network for optimization using Artificial Bee Colony (ABC). In: *IEEE World Congress on Computational Intelligence Brisbane–Australia*; (2012) pp. 10-5.

Effects of Arc-Shaped Partitions in Corners of A Shallow Cavity on Natural Convection

Mert Gurturk¹  Hakan F. Oztop², Fatih Selimefendigil³, Khaled Al-Salem⁴

¹Firat University, Department of Energy Systems Engineering, Elazığ, Turkey

²Firat University, Department of Mechanical Engineering, Elazığ, Turkey

³Celal Bayar University, Department of Mechanical Engineering, Manisa, Turkey

⁴King Saud University, Department of Mechanical Engineering, Riyadh, Saudi Arabia

ABSTRACT

In this study, a numerical analysis carried out to determine the effects of arc-shaped partitions in corners of a shallow cavity on heat transfer which is natural convection and fluid flow. Partitions are accepted as conductive and two different partitions materials are chosen as wood and aluminum. The finite volume approach is used to discretize the governing equations for Rayleigh numbers (Ra) and shape ratio of the arc-shaped partition. It is found that arc-shaped partitions have effect on characteristic parameters of fluid flow and heat transfer. Specially, aluminum arc-shaped partition affects the average heat transfer enhancement, because it has high heat transfer coefficient. Also, possibilities of occurring dead regions are examined and streamlines obtained for without partitions and high Rayleigh numbers which are $Ra=10^5$ and $Ra=10^6$ show that dead regions occur in corners of the shallow cavity. Results obtained from the analysis using partitions and considering different Rayleigh numbers and partition materials show that using partition which is arc-shaped prevent occurring dead regions.

Keywords:

Natural convection; Conjugate heat transfer; Heat transfer; Shallow cavity; Arc-shaped.

Article History:

Received: 2017/12/11

Accepted: 2018/10/14

Online: 2019/01/31

Correspondence to: Mert Gurturk,
Firat University, Department of Energy
Systems Engineering, Elazığ, Turkey
E-Mail: mgurturk@firat.edu.tr

INTRODUCTION

Natural convection phenomena occurs in nature and different applications. Specially, in the cooling of electronic devices is gaining importance. In the recent years, different projects and designs for natural convection applications have been performed. In the natural convection investigations, many different geometries were examined. In the last trend about this phenomena, partitions have been placed at corner or edge of the geometry. These studies were considered square cavity and examined many different parameters related to heat transfer and fluid flow. The square cavity is most popular geometric shape than shallow cavity in the similar analysis. However, studies about shallow cavity placed different shape partitions have been raised. Some of them in the literature were considered in this part of the study. Polat and Bilgen [1] focused on natural convection in inclined shallow cavities, in their study. They heated the side facing the opening a constant heat flux, insulated sides perpendicular to the heated side. The authors solved equations of mass, energy and momentum considering steady state conditions and Boussinesq

approximation. They calculated heat and mass transfer for Rayleigh number from 10^3 to 10^{10} . Shiralkar and Tien [2] studied on heat transfer in a horizontal cavity. The authors considered as adiabatic walls which are horizontal and isothermal side walls of the horizontal cavity for different aspect ratios. Drummond and Korpela [3] studied on natural convection in a shallow enclosure. Only one side of the shallow enclosure was heated. Top and bottom walls were considered as both insulated and conducting. Paoletti and Chenoweth [4] studied on a rectangular cavity for determining heat transfer characteristics. Their problem was two dimension and they considered different aspect ratios and Rayleigh numbers for solution parameters which are Nusselt numbers, temperature and velocity distributions. Zhang et al. [5] studied on a vertical rectangular for determining temperature distribution, the flow characteristics, and the overall heat transfer rate. Novak and Nowak [6] studied on theoretically natural convection in a cavity with different aspect ratios. They used the finite difference technique in their study. Bhave et al.

[7] studied on a square enclosure by using finite volume formulation. They solved governing equations which are mass, momentum and energy via using that numerical method. The problem was considered as two dimensional for determining heat transfer characteristics which is natural convection. Horizontal walls and vertical walls of the enclosure were considered as adiabatic and differentially heated, respectively. Karatas and Derbentli [8] studied the natural convection inside the vertical shallow cavity. Benos et al. [9] performed a work on natural convection in the shallow cavity which is horizontal. Alloi and Vasseur [10] studied the natural convection in a shallow cavity in the presence of micropolar fluids. Also, Alloi et al. [11] tested the natural convection phenomena in the presence of nanofluid for shallow cavities.

This study is to make a control of different parameters in a shallow cavity by inserting arc-shaped passive equipment to the corner. Thus, energy efficiency will be increase due to ignored of dead regions at the corners. In the analysis, different parameters are considered. These parameters are the arc-shape aspect ratios which is symbolized as R, different Rayleigh numbers from $Ra=10^4$ to $Ra=10^6$, different partition materials which are wood and aluminum. About detail solution method and approach are explained next part of this study.

MATERIAL AND METHODS

The physical model is presented in Fig. 1 (a) where boundary conditions shows. It is a shallow cavity with $H < L$ and horizontal wall has an isothermal heaters. Vertical walls are considered as adiabatic. Bottom wall of the shallow cavity is defined steady temperature boundary condition which is symbolized as T_H , and temperature value of the top wall is lower than bottom wall. The temperature of the top wall is indicated as T_C . The shallow cavity has two arc-shaped partitions that these partitions made from different materials. In Fig. 1 (a), g is gravity and R is aspect ratio of the of the arc-shape partitions. Thus, they have different thermal conductivity values. The radius of conductive material is changed as a governing parameter on fluid flow and heat transfer. Fig. 1 (b) shows grid distribution of the shallow cavity.

The governing equations are based on the conservati-on laws. While the energy equation was written, Boussinesq approximation was considered. It means that fluid properties which is physical are considered as constant, but density of the fluid change in body force term of the momentum equation. Viscous dissipation is neglected and, radiation heat transfer and pressure work are neglected too. The finite volume method is used to solve the governing equations. The SIMPLE algorithm is used to treat the pressure term

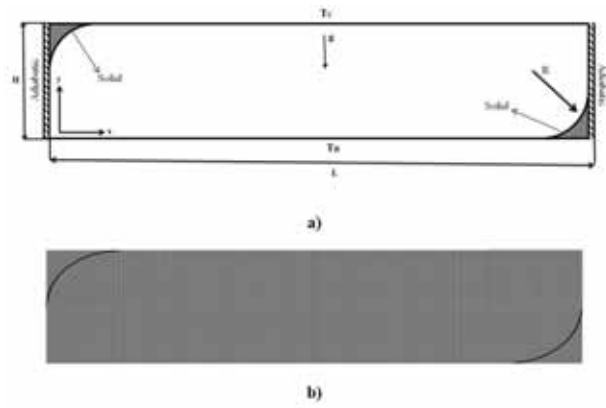


Figure 1. a) Shallow cavity, b) Grid Distribution

[12]. QUICK scheme [13] is used for the discretization of the convective terms in the momentum and energy equations. The calculations are done using FLUENT [14] commercial software. Considering with these assumptions, the governing equations can be written as,

$$\frac{\partial u}{\partial x} + \frac{\partial v}{\partial y} = 0 \quad (1)$$

$$u \frac{\partial u}{\partial x} + v \frac{\partial u}{\partial y} = -\frac{1}{\rho} \frac{\partial p}{\partial x} + \nu \left(\frac{\partial^2 u}{\partial x^2} + \frac{\partial^2 v}{\partial y^2} \right) \quad (2)$$

$$u \frac{\partial v}{\partial x} + v \frac{\partial v}{\partial y} = -\frac{1}{\rho} \frac{\partial p}{\partial y} + \nu \left(\frac{\partial^2 v}{\partial x^2} + \frac{\partial^2 v}{\partial y^2} \right) + g\beta(T - T_c) \quad (3)$$

$$u \frac{\partial T}{\partial x} + v \frac{\partial T}{\partial y} = \frac{k}{\rho C_p} \left(\frac{\partial^2 T}{\partial x^2} + \frac{\partial^2 T}{\partial y^2} \right) \quad (4)$$

For solid region, the governing equation can be considered Eq. (5).

$$\frac{\partial^2 T}{\partial x^2} + \frac{\partial^2 T}{\partial y^2} = 0 \quad (5)$$

The governing equations in terms of velocity and pressure can be written in a dimensionless form as,

$$\frac{\partial U}{\partial X} + \frac{\partial V}{\partial Y} = 0 \quad (6)$$

$$U \frac{\partial U}{\partial X} + V \frac{\partial U}{\partial Y} = -\frac{\partial P}{\partial X} + Pr \left(\frac{\partial^2 U}{\partial X^2} + \frac{\partial^2 U}{\partial Y^2} \right) \quad (7)$$

$$U \frac{\partial V}{\partial X} + V \frac{\partial V}{\partial Y} = -\frac{\partial P}{\partial Y} + Pr \left(\frac{\partial^2 V}{\partial X^2} + \frac{\partial^2 V}{\partial Y^2} \right) + Ra Pr \theta \quad (8)$$

$$U \frac{\partial \theta}{\partial X} + V \frac{\partial \theta}{\partial Y} = \left(\frac{\partial^2 \theta}{\partial X^2} + \frac{\partial^2 \theta}{\partial Y^2} \right) \quad (9)$$

For solid region,

$$\frac{\partial^2 \theta}{\partial x^2} + \frac{\partial^2 \theta}{\partial y^2} = 0 \quad (10)$$

For dimensionless variables, Eq. (11) can be used:

$$X = \frac{x}{L}, Y = \frac{y}{L}, U = \frac{uL}{\alpha}, V = \frac{vL}{\alpha},$$

$$P = \frac{(p + \rho gy)L^2}{\rho \nu^2}, \theta = \frac{T - T_c}{T_h - T_c} \quad (11)$$

Boundary conditions for walls are follow as,

$$X = 1, 0 \leq Y \leq 1, U = 0, V = 0, \theta = 1 \quad (12)$$

$$X = 0, 0 \leq Y \leq 1, U = 0, V = 0, \theta = 0 \quad (13)$$

$$0 \leq X \leq 1, Y = 0, U = 0, V = 0, \frac{\partial \theta}{\partial Y} = 0 \quad (14)$$

The thermal boundary condition for conductive of the arc-shaped partition is written as,

$$k_{fluid} \left(\frac{\partial \theta}{\partial n} \right)_{fluid} = k_{solid} \left(\frac{\partial \theta}{\partial n} \right)_{solid} \quad (15)$$

$$T_{fluid} = T_{solid} \quad (16)$$

Prandtl number, Grashof number and Rayleigh number are given as

$$Pr = \frac{\nu}{\alpha}, Gr = \frac{g \beta \Delta T H^3}{\nu^2}, Ra = Gr \cdot Pr \quad (17)$$

The detail information about the method, algorithm and using software can be found in references [12 – 14]. The Nusselt numbers which are local and aveage are calculated by using Eqs. (18) and (19).

$$Nu = - \left. \frac{\partial \theta}{\partial X} \right|_{X=0} \quad (18)$$

$$Nu_{ave} = \int_0^H Nu_w dy \quad (19)$$

The present code is validated by earlier works to supply the validity of the code. In this case, the study is performed for the same Rayleigh number with literature and differentially heated cavity without any partition. Average Nusselt numbers are calculated and compared with two different works in the literature as shown in Table 1.

As can be seen in Table 1, results obtained show good agreement with literature [15, 16]. Fluid flow and natural convection characteristics are determined in the physical model which is shallow cavity. Many different parameters are considered for using with and without partitions, and

Table 1. Average Nusselt number

<i>Nu</i>	<i>Ra=10⁴</i>	<i>Ra=10⁵</i>	<i>Ra=10⁶</i>
<i>DC Wan et al. [15]</i>	2.254	4.598	8.976
<i>G Barakos et al. [16]</i>	2.245	4.510	8.806
<i>Present Study</i>	2.235	4.509	8.904

these parameters are streamlines, local and average Nusselt number, temperature distribution inside of the shallow cavity. These results are shared in next section.

RESULTS AND DISCUSSION

In this study, a numerical analysis carried out to determine the effects of arc-shaped partitions in corners of a shallow cavity on heat transfer which is natural convection and fluid flow. Partition shapes are made from aluminum and wood. Aluminum is used for many heat transfer applications due to having high thermal conductive. Materials which have low thermal conductive are used for heat transfer control. In this perspective, wood is chosen as material having low thermal conductive and effects of these materials on heat transfer and fluid flow characteristics are examined and compared. The effects of the varying Rayleigh number on the distributions which are streamline and isotherm are demonstrated in Fig. 2-4 for without partitions, wood and aluminum partition (*R=1.1*) cases.

Temperature values unit in the isotherms is Kelvin. As

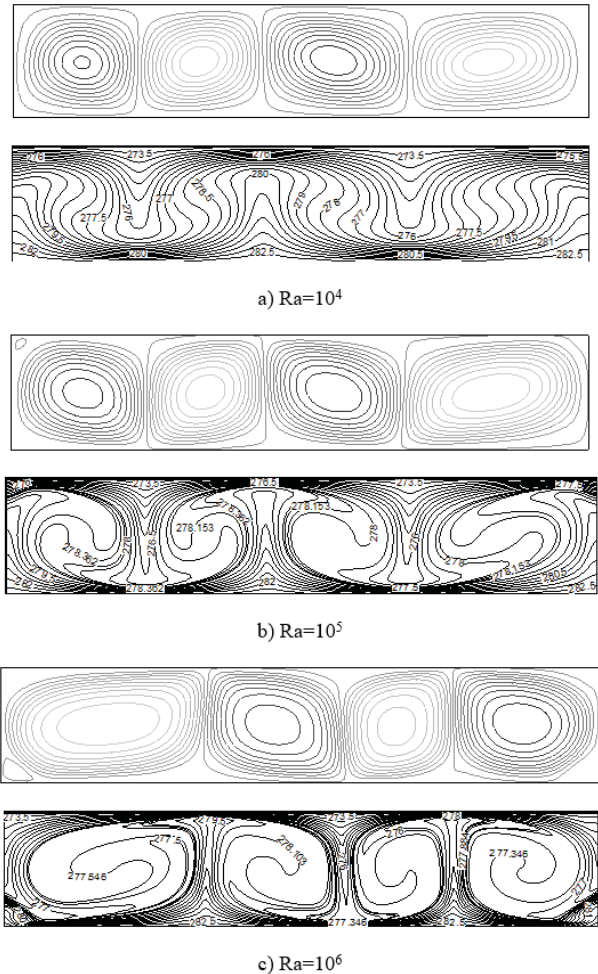


Figure 2. Streamlines (on the top) and isotherms (on the bottom) without partition for various Rayleigh numbers

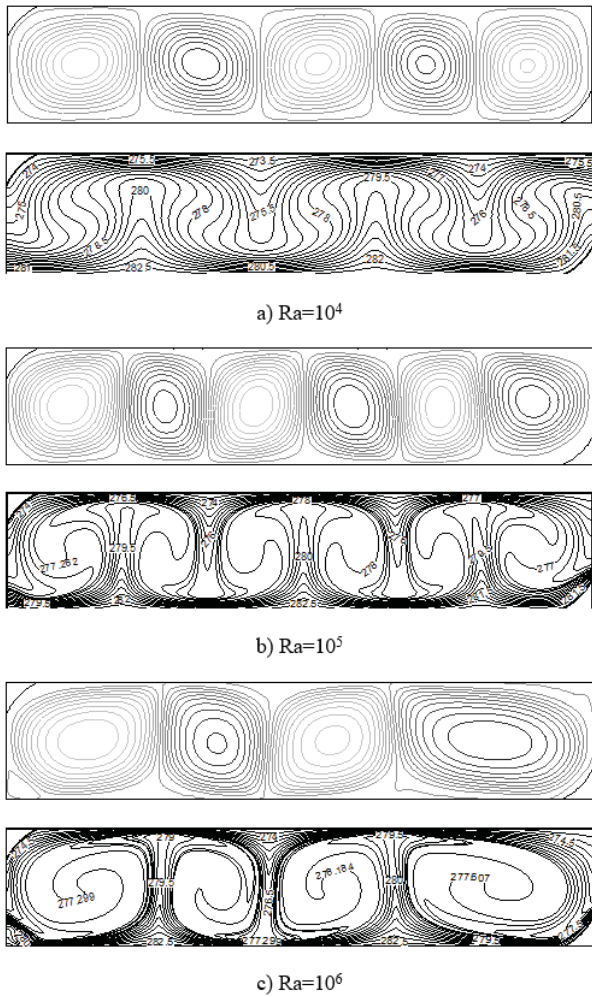


Figure 3. Streamlines (on the top) and isotherms (on the bottom) with aluminum partition for various Rayleigh numbers, $R=1.1$

can be seen at streamlines in Fig. 2, the results obtained from the analysis show that dead regions at the corners occur for $Ra=10^5$ and $Ra=10^6$. Fig. 3 shows results obtained from the streamlines and isotherms with aluminum partition for different Ra numbers.

In the Fig. 3, dead region occur only for $Ra=10^6$ and $R=1.1$. This result shows that dead region can be prevented by using partition, but dead region can occur based on flow characteristic in corners where partition is not placed.

The number of cells is four within the cavity for the case without partition and, when the Rayleigh number increases, the strength of the natural convection increases. The shape of the cells gets distorted in different directions with increasing the Rayleigh number and isotherms are affected due to increasing convection effects of buoyancy. Adding a partition effects the number of cells and temperature distribution within the cavity as can be seen in Figs. 3-4. When the aluminum partition is used, the number of cells is first increased to six and then decreased to four with increasing the Rayleigh number. When the wood material is used the number of cells is decreased to three for the highest Ray-

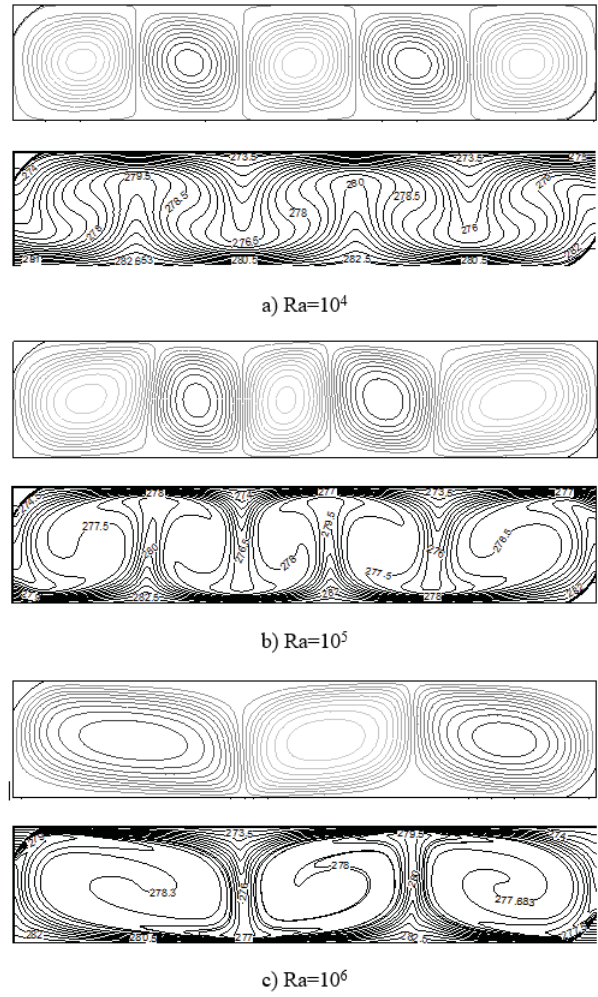


Figure 4. Streamlines (on the top) and isotherms (on the bottom) with wood partition for various Rayleigh numbers, $R=1.1$

leigh number of interest. The effects of Ra number on the local Nu number distributions are depicted in Fig. 5.

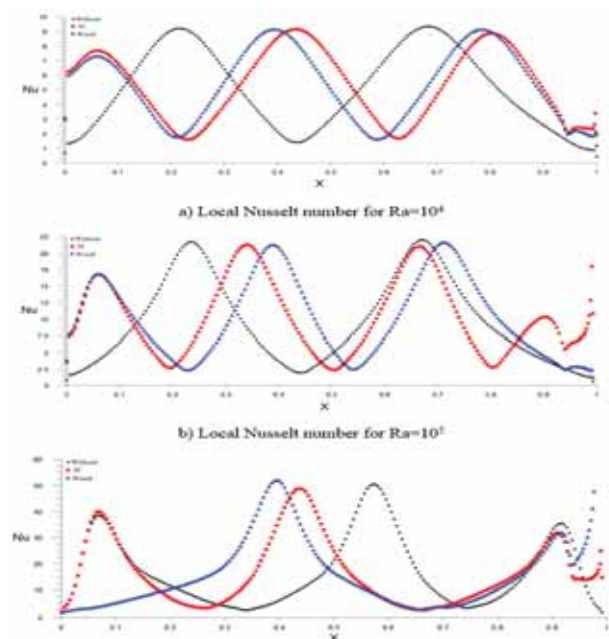


Figure 5. Variation of local Nusselt Number along the horizontal direction for various Rayleigh numbers, $R=1.1$

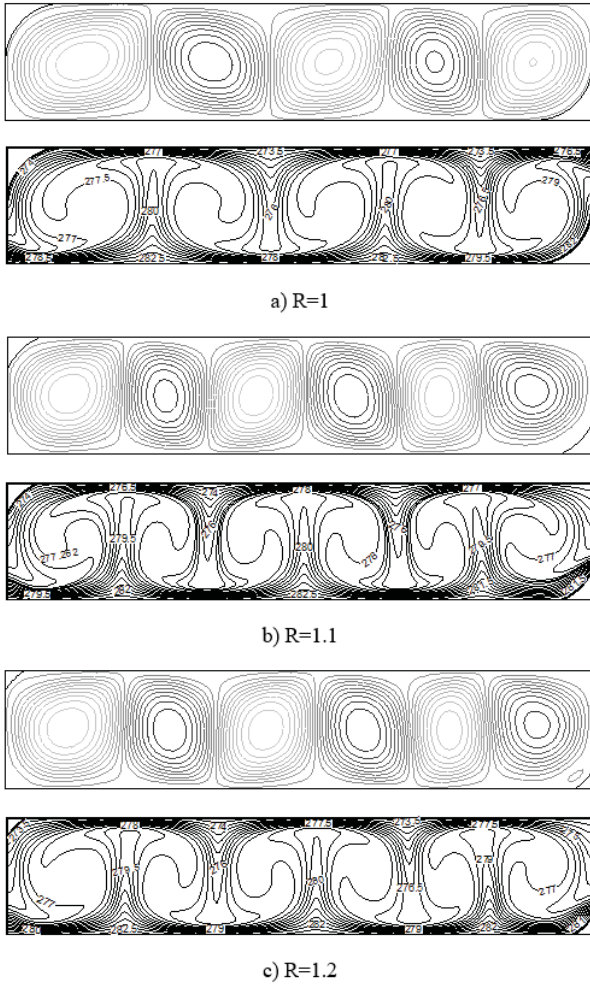


Figure 6. Effects of curvature on the streamlines (on the top) and isotherms (on the bottom) with aluminum partition, $Ra=10^5$

The number of peaks in the Nusselt number increases with the addition of the partition due to the increased number of cells at $Ra=10^4$ and $Ra=10^5$. The discrepancy between the aluminum and wood partition is more visible at $Ra=10^6$. Effects of the curvature of the partition are presented in Fig. 6 for aluminum and in Fig. 7 for wood partition ($Ra=10^5$).

The results obtained from the analysis show that dead regions at the corners occur for $Ra=10^5$ and $Ra=10^6$. The dead region occurs only for $Ra=10^6$ and $R=1.1$ and dead regions are not seen in all others situations which are used partitions. When the radius of the curvature increases, the number of the cells is increased from five to six for aluminum partition. The size and strength of the cells on the left and right ends of the cavity decrease as the radius of the curvature increases for the aluminum partition. When the wood partition is used in Fig. 7, although the number of cells remains the same, the size of the cells on the left and right ends of the cavity first increases then decreases when the radius of the curvature is increased. Fig. 8 demonstrates the effect of varying the radius of curvature on the local Nu number along the horizontal wall of the cavity at $Ra=10^5$.

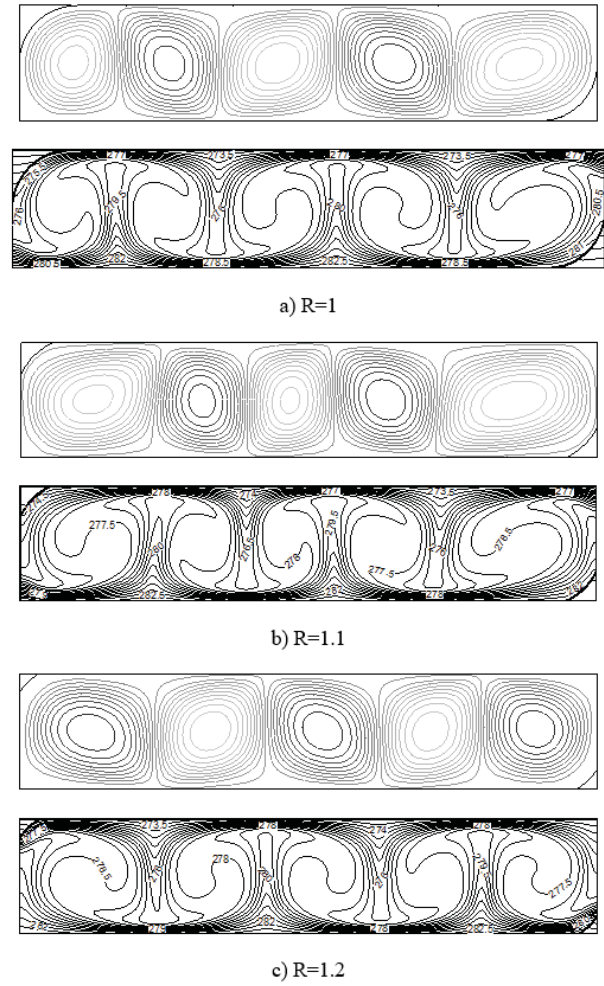


Figure 7. Effects of curvature on the streamlines (on the top) and isotherms (on the bottom) with wood partition, $Ra=10^5$

In all situations which are placed partition, local Nusselt number values increase. As can be seen in the figures

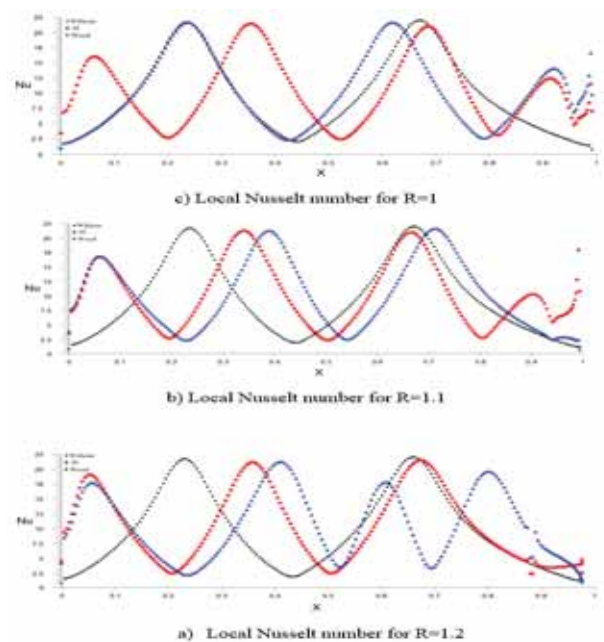


Figure 8. Variation of local Nusselt Number along the horizontal direction for various radius of curvature, $Ra=10^5$

Table 2. Average Nu

R	$Ra=10^4$		$Ra=10^5$		$Ra=10^6$	
	Average Nu_{ave}		Average Nu_{ave}		Average Nu_{ave}	
	Al	Wood	Al	Wood	Al	Wood
0	5.05	5.05	9.63	9.63	16.809	16.809
1	5.763	5.656	11.264	11.28	20.076	19.327
1.1	5.542	5.54	10.456	10.629	16.762	14.956
1.2	5.439	5.23	10.524	10.15	17.141	18.361

related to local Nusselt number, local Nu value changes along the x-axis. Especially, local Nu numbers are very variable at origin of x and y axis ($x=0$ and $y=0$) and end of the x axis. The partition which is arc-shaped causes this variable. For example, when results obtained all situations which are both with and without partition are compared, effects of without partition can be shown in the local Nusselt numbers obtained from without partition situation. The local Nusselt number values change between 1 and 50 for $R=1.1$ and $Ra=10^6$. Also, the local Nu values change between 1 and 9 for $R=1.1$ and $Ra=10^4$. The number of peaks increases when the partition is added due to the increased number of cells for $R=1$ and $R=1.1$. The discrepancy between the aluminum and wood partition is more apparent for $R=1.2$. The radius of curvature and thermal conductivity of the partition can be used as passive element to control the heat transfer and fluid flow within the cavity. Average Nusselt number values allow us to make a general assessment about results obtained from this study. Averaged Nusselt numbers along the horizontal wall of the cavity are shown in Table 2.

Adding a partition enhances the heat transfer. At $Ra=10^4$ and $Ra=10^5$, averaged heat transfer decreases as the radius of curvature increases for aluminum and wood partitions. At the highest Rayleigh number of interest, an increase and then a decrease in the averaged heat transfer is seen as the radius of curvature increases. When the average Nu number is considered with and without partitions, heat transfer increasing rate is determined as 12.37% for $R=1$, using aluminum partition and $Ra=10^4$. In this perspective and similar conditions, heat transfer increasing rate is calculated as 10.71% for using wood partition. When values obtained for $R=1.2$ and $Ra=10^6$ are considered, rates of increase in heat transfer for without partition and using aluminum and wood partitions are 1.93% and 8.45%, respectively. The greatest rate of increase in heat transfer is obtained for $R=1$, using aluminum partition and $Ra=10^6$. In these conditions, rate of increase in heat transfer is calculated as 16.27%. For using wood partition, rate of increase in heat transfer is determined as 13.02% in same conditions. It can be said that using partition in shallow cavity increases heat transfer rate in all of conditions of $Ra=10^4$. Results obtained for $R=1.1$ and $Ra=10^6$ show that heat transfer decrease. Rate of decrease

in heat transfer for using aluminum partition and $R=1.1$ at $Ra=10^6$ is 0.27% and in similar conditions, rate of decrease in heat transfer for using wood is 11.02%. When aluminum and wood partition are compared, aluminum shows better results than wood. However results obtained from situation using wood partition show that material having low thermal conductive can be used for heat transfer control. Especially, results obtained from this study can be considered in applications which are cooling of electronic devices, conditioning of rooms and so on. When streamlines obtained from the analysis which are with and without partitions are examined, the partitions effect on fluid flow characteristic as well as heat transfer. While four cell occur in the streamlines obtained for without partition and $Ra=10^4$, $Ra=10^5$ and $Ra=10^6$, different cells are obtained for with partitions. For example, five cell occur at result obtained for $Ra=10^4$ and aluminum, six and four cell occur for $Ra=10^5$, $Ra=10^6$ and aluminum, respectively. As can be seen in Fig. 4, five and three circular flow occur for using with wood partition and $Ra=10^4$, $Ra=10^5$ and $Ra=10^6$ in the streamlines. The heat transfer and fluid flow characteristics strongly influenced depending on these parameters which are using partition and partition material type, Ra and R.

CONCLUSION

Numerical study of natural convection in arc-shaped partitions in corners of a shallow cavity filled with air was performed. The effects of arc-shaped partitions in corners of a shallow cavity on heat transfer which is natural convection and fluid flow. Partitions are accepted as conductive and two different partitions materials are chosen as wood and aluminum. Also, possibilities of occurring dead regions are examined and streamlines obtained for without partition and high Rayleigh numbers which are $Ra=10^5$ and $Ra=10^6$ show that dead regions occur in corners of the shallow cavity. Some important conclusion can be indicated from this numerical study as:

- Characteristic parameters of the flow and heat transfer are affected by adding a arc-shaped partitions to the shallow cavity.

- Curvature of the partition affects the average heat transfer enhancement and this can be used as control parameter.

- The results obtained from the analysis show that dead regions at the corners occur for $Ra=10^5$ and $Ra=10^6$. The dead region occur only for $Ra=10^6$ and $R=1.1$ and dead regions are not seen in all others situations which are used partitions.

- Results obtained from the analysis using partitions and considering different Rayleigh numbers and partition materials show that using partition which is arc-shaped prevent occurring dead regions.

- At $Ra=10^4$, heat transfer enhancements of 14%, 9.74% and 7.7% were obtained for $R=1$, $R=1.1$ and $R=1.2$ compared to flat cavity. These results were obtained for aluminum arc-shaped partition. In the same conditions and for wood arc-shaped partition, heat transfer enhancements of 12%, 9.7% and 3.36% were obtained.

The different materials can be used as partitions and many different parameters can be examined considering Ra , R , fluid and so on. In this study, fluid is air but different studies can be carried out by using nanofluid. Also, this problem can be considered for unsteady flow.

References

1. Polat O, Bilgen E. Conjugate heat transfer in inclined open shallow cavities. *International Journal of Heat Mass Transfer* 46 (2003) 1563-1573.
2. Shiralkar GS, Tien CL. A numerical study of laminar natural convection in shallow cavities. *Transactions of ASME* 103 (1981) 226-231.
3. Drummond JE, Korpela SA. Natural convection in a shallow cavity. *Journal Fluid Mechanic* 182 (1987) 543-564.
4. Paolucci S, Chenoweth DR. Natural convection in shallow enclosures with differentially heated endwalls. *Transactions of ASME* 110 (1988) 625-634.
5. Zhang Z, Bejan A, Lage JL. Natural convection in a vertical enclosure with internal permeable screen. *Transactions of ASME* 113 (1991) 377-383.
6. Novak MH, Nowak ES. Natural convection heat transfer in slender window cavities. *Transactions of ASME* 115 (1993) 476-479.
7. Bhawe P, Narasimhan A, Rees DAS. Natural convection heat transfer enhancement using adiabatic block: Optimal block size and Prandtl number effect. *International Journal of Heat and Mass Transfer* 49 (2006) 3807-3818.
8. Karatas H, Derbentli T. Natural convection and radiation in rectangular cavities with one active vertical wall. *International Journal of Thermal Sciences* 123 (2018) 129-139.
9. Benos LTh, Kakarantzas SC, Sarris IE, Grecos AP, Vlachos NS. Analytical and numerical study of MHD natural convection in a horizontal shallow cavity with heat generation. *International Journal of Heat and Mass Transfer* 75 (2014) 19-30.
10. Alloui Z, Vasseur P. Natural convection in a shallow cavity filled with a micropolar fluid. *International Journal of Heat and Mass Transfer* 53 (2010) 2750-2759.
11. Alloui Z, Vasseur P, Reggio M. Natural convection of nanofluids in a shallow cavity heated from below. *International Journal of Thermal Sciences* 50 (2011) 385-393.
12. Patankar SV. *Numerical Heat Transfer and Fluid Flow*, Hemisphere, NewYork, 1980.
13. Hayase J, Humphrey AC, Greif AR. A Consistently formulated QUICK scheme for fast and stable convergence using finite-volume iterative calculation procedures. *Journal of Computational Physics* 98 (1992) 108-118.
14. Fluent, 12.0 User Guide. 2009.
15. Barakos G, Mitsoulis E, Assimacopoulos D. Natural convection flow in a square cavity revisited: laminar and turbulent models with wall functions. *International Journal for Numerical Methods in Fluids* 18 (1994) 695-719.
16. Wan DC, Patnaik BSV, Wei GW. A new benchmark quality solution for the buoyancy-driven cavity by discrete singular convolution. *Numerical Heat Transfer, Part B: Fundamentals* 40 (2001) 199-228.

Identification of Antioxidant Activity by Different Methods of a Freshwater Alga (*Microspora* sp.) Collected From a High Mountain Lake

Bulent Akar¹  Zeynep Akar²  Bulent Sahin³ 

¹Gumushane University, Department of Food Engineering, Gumushane, Turkey

²Gumushane University, Department of Genetic and Bioengineering, Gumushane, Turkey

³Karadeniz Technical University, Department of Biology Education, Trabzon, Turkey

ABSTRACT

Algae contain a large amount of biological active compounds functioning as antioxidant, antimicrobial and anti-tumour. In the present research, antioxidant activity of freshwater alga *Microspora* sp. (Chlorophyta) extract prepared in different solvents (methanol, acetonitrile, ethanol, acetone and ethyl acetate) was determined with three different methods; 2,2-diphenyl-1-picrylhydrazyl (DPPH•), Iron (III) Reduction / Antioxidant Power (FRAP) Assay and Copper (II) Reductive Antioxidant Activity (CUPRAC). The alga samples collected from the high mountain lake (2733 m above sea level) localized in Gümüşhane province of Turkey. The algal extracts prepared in different solvents showed antioxidant activity. The values of DPPH• varied from 8.97% (in acetonitrile extract) to 31.15% (in methanol extract). As in the DPPH• method, the lowest and highest values in the FRAP method were measured based on μM TEAC (Trolox Equivalent Antioxidant Capacity) in methanol and acetonitrile extracts as 60.303 μM and 359.394 μM respectively. While the lowest value of CUPRAC test was determined in acetonitrile extract (0.041 μM TEAC) as in the other tests, highest value was measured in ethanol extract (0.101 μM TEAC). The values of highest antioxidant activity in both DPPH• and FRAP methods was measured in the methanol solvent whilst was determined in the ethanol solvent for CUPRAC.

Keywords:

Algae; *Microspora* sp.; Antioxidant; DPPH•; FRAP; CUPRAC

INTRODUCTION

Algae having both macroscopic and microscopic forms and growing in all environments including the extreme conditions are photosynthetic organisms that contribute greatly to primer production of aquatic ecosystems. There are many records about they have been used as food and drug since centuries [1-3]. Particularly, their use in the food and pharmaceutical industry depends on presence of large number of various bioactive compounds. The variety of these bioactive compounds is related to the stress conditions in the extreme environments such as high altitude regions [4].

In order to survive, algae are resistant to stress factors such as high salinity, high and low temperature, low nutrients, hot alkaline and acidic environments,

and non-thermal acidic environments, high and low light conditions. Thus, they well adapt to extreme environmental conditions with synthesizing many natural products also called as secondary metabolites [5-7]. The natural products of algae include compounds such as polyphenols, flavonoids, amino acids, lignins, terpenoids, tocopherols, fatty acid, phenolic acids and have antioxidant, antimicrobial, antifungal and antiviral activity [8, 9]. Generally, researchers have focussed terrestrial plants (flower, fruits, seed, leaf, stem, bark and root) in determining antioxidant substances. However, the source of natural antioxidants is not only terrestrial plants, but also algae have been reported to be rich in natural antioxidant compounds [9-11]. Algae having species richness are potential sources of natural bioactive compounds for new demand in medicine and food industry

Article History:

Received: 2018/02/05

Accepted: 2018/05/13

Online: 2019/03/28

Correspondence to: Bulent AKAR,
Gumushane University, Faculty of
Engineering and Natural Sciences,
Department of Food Engineering,
Gumushane, Turkey
Tel: +90(4562331000)
Fax: +90(4562331075)
E-mail: akarblnt@gmail.com

[4, 12]. Among these natural compounds, phenolics composed of one or more aromatic rings containing hydroxyl groups are considered to be one of the most important classes of natural antioxidants [13]. Especially, marine macroalgae have a large number of these compounds. Red algae (Rhodophyta), brown algae (Phaeophyta) and green algae (Chlorophyta) contains some phenolic compounds such as phlorotannins, bromophenols, terpenoids, mycosporine-like amino acids, meroditerpenoids, coumarins, vanillic acid. The phlorotannins are the most studied phenolic compounds in marine algae and are used in preparation of nutraceutical, cosmeceutical, and pharmaceutical products [13, 14].

Genus *Microspora* Thuret is classified in the Chlorophyta division that distributed in both freshwater and marine environments. It has H-shaped cell wall, cells slightly swollen, cylindrical, and quadrate, arranged uniseriate. The filaments are unbranched and occurring free or basically attached. Chloroplast is parietal or coarse net or net, not present pyrenoid. Aplanospores or akinetes are present [15, 16].

Although Turkey has a rich diversity of freshwater algae [17, 18], there are few studies to determine their chemical composition and biological activity [19-24]. Although, there are many systematic, taxonomic and ecological studies on the genus *Microspora*, the number of studies based on its chemical composition, antioxidant and antimicrobial activity is limited in the literature [25-27]. The purpose of this study was to determine the efficiency of antioxidant activity of an alga *Microspora* sp. in different solvents with commonly used three antioxidant activity determination methods and to provides availability of freshwater algae for research in the food and pharmaceutical industry.

MATERIALS AND METHODS

Samples Collection

The samples of *Microspora* sp. were collected from the Acembol Lakes (Lake AC-3) of the Artabel Lakes Natural Park located in the Gümüşhane province in August 2016. The lake was 2733 m above sea level and located at 40° 25' 03" N – 39° 03' 28" E. Samples of *Microspora* sp., which occurred blooms on the surface of the lake, are collected from the 0 - 0.5 m below surface. The samples were washed several times with distilled water for removal epiphytic organisms and other substance in the laboratory. Then, algae samples were dried at room temperature for 2 weeks and blandered into powder [24]. However some algal specimen was stored in 4% formaldehyde solution. Algae identified according to related books [15, 16].

Preparation of Algal Extracts

Five different extracts (acetone, acetonitrile, ethanol, ethyl acetate and methanol) were prepared from powde-

red *Microspora* sp. samples at room temperature. In the preparation of each extract 20 g of the sample (powder) was dissolved in 50 mL of solvent. Extractions were mixed by a magnetic stirrer for 2 hours. Then the extracts were filtered consecutively with filter paper and syringe filter (Minisart, NY 0.45 µm). Clear solutions obtained at the end of the process were stored at room temperature and in a cool, dark place until the test.

2,2-diphenyl-1-picrylhydrazyl (DPPH•) Scavenging Activity

DPPH• method developed by Cuendet et al. [28] was used for determining antioxidant activity extracts prepared with different solvents of *Microspora* sp. Firstly, 100 µM DPPH• radical solution was prepared and the solution was dissolved in the magnetic stirrer for 30 minutes. Each of algal extract was pre-tested and diluted 1/5 and analyzed in triplicate. However, each concentration of samples were run for a samples and reagent blank after 50 minutes, the absorbance values of the tubes mixed by the DPPH• reagent were read at 517 nm at spectrophotometer and the % inhibition (DPPH• purification) values were calculated as follows

$$\% \text{ Inhibition (radical cleaning power)} = [(ADPPH - ASample) / ADPPH] \times 100$$

ADPPH : Absorbance value of the DPPH solution

ASample : Absorbance value of the sample extract

Iron (III) Reduction / Antioxidant Power (FRAP) Assay

Absorbance in this method occurs at 595 nm and forms $K_3(Fe)CN_6$ color complex [29]. As a standard, the antioxidant Trolox was used at different concentrations (1000-500-250-125-62.5 µM). Different extracts of *Microspora* sp. were run from stock solutions (20 g + 50 mL solvent). Three replications were prepared for all standard and extracts. Firstly, 50 µl samples and standard solutions were transferred. Then 50 µl of sample solvents (methanol and distilled water) were transferred to the reagent blind tubes. After transferring 50 µL of the sample solutions to the sample blind tubes, 1.5 mL of FRAP solution (60% methanol pure water) was added. Thus, 1.5 mL newly prepared FRAP reagent was added to the other tubes at 20 second intervals. The tubes were mixed and after 20 minutes the absorbance values were read at 595 nm spectrophotometer device. The results were calculated as TEAC in comparison with the standard antioxidant Trolox.

Copper (II) Reductive Antioxidant Activity (CUPRAC)

Copper metal is used in CUPRAC and this method is based on the reduction of antioxidant substance Cu (II) to

Cu (I) [30]. In this method, Cu (II) chloride solution, neocuproin solution with 96% ethanol, ammonium acetate buffer (pH = 7) and analysis solutions were added, respectively. Then, 4.1 mL of the final solution was completed and it was kept at room temperature during 30 minutes. At the end of this procedure, absorbance values were measured at 450 nm and antioxidant capacities of the samples were calculated as Trolox equivalent [31].

RESULTS AND DISCUSSION

There are some synthetic antioxidants used in the food industry commercially available. However, some studies indicate that synthetic antioxidants have toxicological and carcinogenic effects on cell of experimental animals [32]. Due to these unfavorable effects, use of synthetic antioxidants was restricted in food industry. Therefore, natural antioxidants are increasingly interested by producers and consumers [10, 32]. Natural antioxidants were commonly obtained from terrestrial plants. But it is not limited to them. Also, aquatic organisms, especially algae have organic and inorganic substances such as polysaccharides, lipids, proteins, carotenoids, phenolic compounds, vitamins and minerals. The content play important role in exhibiting high antioxidant activity of algae [9, 33].

In the present study, *Microspora* extracts were prepared in the five different solvents. Antioxidant activities of each of the algal extracts in these solvents were determined with three different method DPPH•, FRAP and CUPRAC and antioxidant activities results for each methods are compared each other (Table 1).

Table 1. Antioxidant activity (DPPH•, FRAP and CUPRAC) of *Microspora* sp. extracts in different solvents

	% DPPH•	FRAP (μ MTEAC)	CUPRAC (μ MTEAC)
<i>Methanol</i>	31.15 \pm 2.139	359.394 \pm 53.431	0.085 \pm 0.002
<i>Ethanol</i>	26.01 \pm 0.571	345.455 \pm 23.689	0.101 \pm 0.002
<i>Acetonitrile</i>	8.97 \pm 0.713	60.303 \pm 7.348	0.041 \pm 0.003
<i>Acetone</i>	13.00 \pm 0.142	294.545 \pm 36.056	0.098 \pm 0.009
<i>Ethyl acetate</i>	22.58 \pm 0.571	315.455 \pm 22.212	0.079 \pm 0.002

Values are means \pm standard deviations of three (n=3) measurements

DPPH• which is the most commonly used scavenging activity detection method showed the efficacy of highest and lowest in methanol extract (scavenging activity 31.15%) and acetonitrile extract (scavenging activity 8.97%) respectively (Fig. 1). In the less number of antioxidant activity studies carried on *Microspora*, For example, Laungsuwon and Chulalaksananukul [25] determined % DPPH• radical scavenging activity of *Microspora floccosa* in different solvent extracts which consist of water (6.6% \pm 1.4), ethyl acetate (8.9% \pm 1.6), methanol (9.3% \pm 2.2) and hexane (19.7% \pm 1.4). Order of % DPPH• values of solvents of *Microspora floccosa*

is methanol > ethyl acetate compatible with our results partially. However there are differences between % values of DPPH• in both studies. However, Suanmali et al. [27] indicated that environmental factors are effective in changing the antioxidant activity values and reported that values of the % DPPH• varied from 23 to 49.6 in methanol extracts of *Microspora* collected from five different areas. However there are differences between % values of DPPH• in both studies. In addition to this, Suanmali et al. [27] indicated that environmental factors are effective in changing the antioxidant activity values and reported that values of the % DPPH• varied from 23 to 49.6 in methanol extracts of *Microspora* collected from five different areas. In some studies on other filamentous algae in the Chlororophyta, for example Laungsuwon and Chulalaksananukul [25] also measured values of % DPPH• for *Cladophora glomerata*. (Linnaeus) Kützing and the values were determined in different solvent such as methanol (16.7 \pm 2.6), water (18.4 \pm 2.5), hexane (37.4 \pm 2.3), ethyl acetate (49.8 \pm 2.7). In contrary to present study, the lowest value of % DPPH• was detected the in methanol extract of *Cladophora glomerata*. Each species of algae include antioxidant compounds in different qualities and quantities, and the solvents used in extraction is also an important factor for determining the antioxidant capacity because of polarity differences of compounds in algae [34].

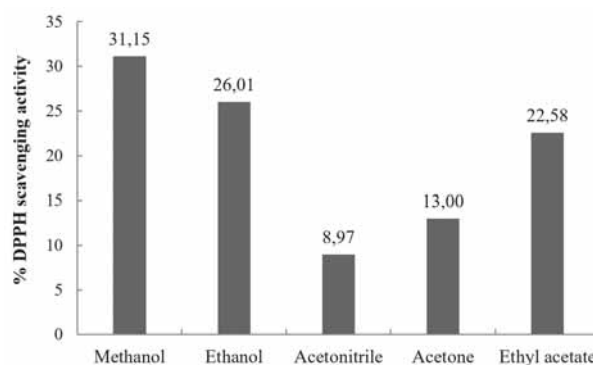


Figure 1. % DPPH scavenging activity

In the FRAP method belonging to the electron-transfer reaction group; Fe (III) salt, Fe (III) (TPTZ)₂Cl₃ (TPTZ = 2,4,6-tripyridyl s-triazine) is used as oxidant [29]. At low pH, the Fe (III) -TPTZ complex is reduced to Fe (II) form. This complex is dark blue in color and the absorption maximum is 595 nm [35]. Due to its simplicity, speed and low cost, the method is useful for the identification of hydrophilic and lipophilic antioxidants. In determination of Iron (III) reduction/antioxidant power (FRAP) Trolox standard calibration graphic with different concentrations was designed (Fig. 2). According to the calibration graphic, μ M TEAC (Trolox Equivalent Antioxidant Capacity) values of algae extracts prepared with different solvents were determined. μ M TEAC values of the algae extracts were ranged from 359.54 μ M (for methanol solvent extracts) to 60.303 μ M, (acetonitrile solvent extracts) (Fig. 3). Therefore, accor-

ding to the FRAP antioxidant assay method, the highest and the lowest antioxidant activity were observed in methanol extract and the acetonitrile extract respectively. The order of the antioxidant values of the solvent extracts measured in the FRAP and DPPH methods is similar (Methanol > Ethanol > Ethyl acetate > Acetone > Acetonitrile).

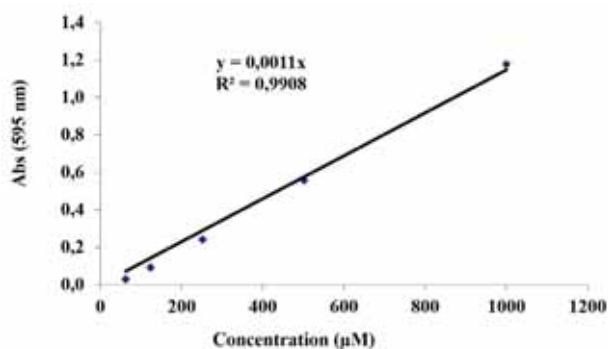


Figure 2. Calibration curve of Trolox equivalent by FRAP Method

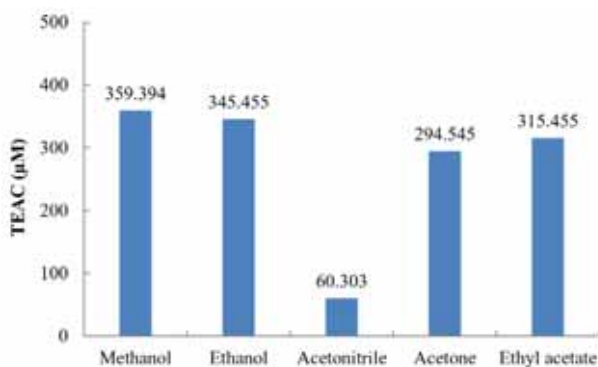


Figure 3. Comparison of FRAP values ($\mu\text{M TEAC}$) of different solvent extracts

CUPRAC is a method based on the reduction of Cu (II) to Cu (I) with present antioxidants in a sample. Simple sugars and citric acid, which cause interference in the FRAP method, are not oxidized by the CUPRAC reagent [31]. It is fast enough to oxidize thiol-type antioxidants. In the method, Trolox standard calibration graphic was designed with six different concentrations of the standart (Fig. 4). $\mu\text{M TEAC}$ values of each algae extract prepared with different solvents were calculated bases on values of the calibration graphic. However, values ($\mu\text{M TEAC}$) of CUPRAC antioxidant activity test of the algal extract were measured in each solvents that are ethanol (0.101 μM), acetone (0.098 μM), methanol (0.085), ethylacetate (0.079 μM), and acetonitrile (0.041 μM) (Fig. 5). Methanol solvent extracts showed the highest antioxidant activity in DPPH• and FRAP methods, while its activity value in CUPRAC method was significant. Safafar et al. [10] pointed out methanol is the most preferred solvent in terms of antioxidative power compared to others.

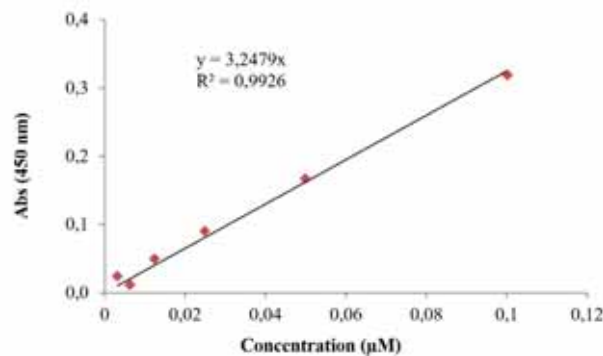


Figure 4. Calibration curve of Trolox equivalent by CUPRAC Method

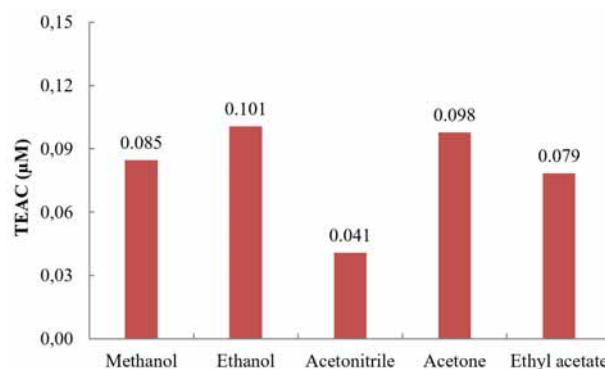


Figure 5. Comparison of CUPRAC values ($\mu\text{M TEAC}$) of different solvent extracts

CONCLUSION

It has been shown that *Microspora sp.* has antioxidant activity in three antioxidant activity assay methods. However, each of the five different solvents extracts have antioxidant activity In DPPH• and FRAP antioxidant assay methods showed the highest and lowest values of antioxidant activity in methanol extract and the acetonitrile extract respectively. While the lowest value of CUPRAC test is determined in acetonitrile extract as in the other tests, highest value is measured in ethanol extract as different from the others. Further studies should be undertaken on the identification of others biological activities of the alga *Microspora sp* and other freshwater algae in order to determine their potential use in the food and drug industry.

References

1. Barsanti L, Gualtieri P. Algae: Anatomy, Biochemistry, and Biotechnology, CRC Press, Taylor& Francis Group, Boca Raton, FL, USA, 2006.
2. Gantar M, Svircev Z. Microalgae and cyanobacteria: food for thought. Journal of Phycology 44 (2008) 260–268.
3. Dias DA, Urban S, Roessner U. A historical overview of natural products in drug discovery. Metabolites 2 (2012)

- 303–336.
4. Challouf R, Dhieb RB, Omrane H, Ghozzi K, Ouda, HB. Antibacterial, antioxidant and cytotoxic activities of extracts from the thermophilic green alga, *Cosmarium* sp. African Journal of Biotechnology 11 (2012) 14844–14849.
 5. Fogg GE. Algal adaptation to stress—some general remarks, in: Rai LC, Gaur JP (Eds.) Algal adaptation to environmental stresses Physiological, Biochemical and Molecular Mechanisms. Springer-Verlag, Berlin Heidelberg, pp. 1–19, 2001.
 6. Seckbach J. Algae and cyanobacteria in extreme environments. Springer Science and Business Media, Dordrecht, 2007.
 7. Maschek JA, Baker BJ. The chemistry of algal secondary metabolism, in Amsler CD (Ed.) Algal chemical ecology. Springer, Berlin, Heidelberg, pp. 1–24, 2008.
 8. Taskin E, Ozturk M, Taskin E, Kurt O. Antibacterial activities of some marine algae from the Aegean Sea (Turkey). African journal of Biotechnology 6 (2007) 2746–2751.
 9. Cox S, Abu-Ghannam N, Gupta S. An assessment of the antioxidant and antimicrobial activity of six species of edible Irish seaweeds. International Food Research Journal 17 (2010) 205–220.
 10. Safafar H, Van Wagenen J, Møller P, Jacobsen C. Carotenoids, phenolic compounds and tocopherols contribute to the antioxidative properties of some microalgae species grown on industrial wastewater. Marine Drugs 13 (2015) 7339–7356.
 11. Balakrishnan D, Kandasamy D, Nithyanand P. A review on Antioxidant activity of marine organisms. International Journal of Chem Tech Research 6 (2014) 3431–3436.
 12. Ertürk O, Taş, B. Antibacterial and antifungal effects of some marine algae. Kafkas Univ Vet Fak Derg, 17 (2011) 121–124.
 13. Machu L, Mísurcova L, Vavra Ambrozova J, Orsavova J, Mlcek J, Sochor J, Jurikova T. Phenolic content and antioxidant capacity in algal food products. Molecules 20 (2015) 1118–1133.
 14. Freile-Pelegrín Y, Robledo D. Bioactive Phenolic Compounds from Algae, in: Hernández-Ledesma B, Herrero M (Eds.) Bioactive Compounds from Marine Foods: Plant and Animal Sources. First Edition, John Wiley & Sons, Ltd, The Atrium, West Sussex, UK, pp. 113–129, 2014.
 15. Prescott, G. W. Algae of the western Great Lakes area, Fourth printing., Cranbrook Institute of Science Bulletin, USA, 1970
 16. Sheath RG, Wehr JD. Freshwater algae of North America: ecology and classification, Academic Press, An imprint of Elsevier Science, San Diego, California, 2003.
 17. Gönüloğlu A, Öztürk M, Öztürk MA. check-list of the freshwater algae of Turkey. OMÜ Fen Edeb Fak Fen Dergisi 7 (1996) 8–46.
 18. Aysel V. Check-list of the freshwater algae of Turkey. Journal of Black Sea/Mediterranean Environment 11 (2005) 1–124.
 19. Orhan I, Sener B, Atıcı T, Brun R, Perozzo R, Tasdemir D. Turkish freshwater and marine macrophyte extracts show in vitro antiprotozoal activity and inhibit FabI, a key enzyme of *Plasmodium falciparum* fatty acid biosynthesis. Phytomedicine 13 (2006) 388–393.
 20. Katircioglu H, Beyatli Y, Aslim B, Yüksekdag Z, Atici T. Screening for Antimicrobial Agent Production of Some Freshwater. Microbiology 2 (2006) 1–5.
 21. Kartal M, Orhan I, Abu-Asaker M, Senol FS, Atici T, Sener B. Antioxidant and anticholinesterase assets and liquid chromatography–mass spectrometry preface of various fresh-water and marine macroalgae. Pharmacognosy Magazine 5 (2009) 291–297.
 22. Demiriz T, Cokmus C, Pabuccu K. Antimicrobial Activity of Some Algal Species Belonging to Cyanobacteria and Chlorophyta. Asian Journal of Chemistry 23 (2011) 1384–1386.
 23. Cakmak YS, Kaya M, Asan-Ozusaglam M. Biochemical composition and bioactivity screening of various extracts from *Dunaliella salina*, a green microalga. EXCLI Journal 13 (2014) 679–690.
 24. Taş B, Ertürk Ö, Yılmaz Ö, Çol Ayvaz M, Ertürk EY Chemical components and biological activities of two freshwater green algae from Ordu, Turkey. Turkish Journal of Biochemistry 40 (2015) 508–517.
 25. Laungsuwon R, Chulalaksananukul W. Antioxidant and anticancer activities of freshwater green algae, *Cladophora glomerata* and *Microspora floccosa*, from Nan River in northern Thailand. Maejo International Journal of Science and Technology 7 (2013) 181–188.
 26. Kosasu T, Wongklom A, Moonsin P. Total phenolics, flavonoids and antioxidant activity of fresh water macroalgae from Ubon Ratchathani. Thailand. Journal of Food Science and Agricultural Technology 1 (2015) 207–210.
 27. Suanmali W, Moonmaun S, Phoomyai P. Efficiency of Antioxidant Compounds from Macro Edible Algae. Journal of Energy and Power Engineering 11 (2007) 173–178.
 28. Cuendet M, Hostettmann K, Potterat O, Dyatmiko W. Iridoid glucosides with free radical scavenging properties from *Fagraea blumei*. Helvetica Chimica Acta 80 (1997) 1144–1152.
 29. Benzie IF, Strain JJ. The ferric reducing ability of plasma (FRAP) as a measure of “antioxidant power”: the FRAP assay. Analytical Biochemistry 239 (1996) 70–76.
 30. Prior RL, Wu X, Schaich K. Standardized methods for the determination of antioxidant capacity and phenolics in foods and dietary supplements. Journal of Agricultural and Food Chemistry 53 (2005) 4290–4302.
 31. Apak R, Güçlü K, Özyürek M, Karademir SE. Novel total antioxidant capacity index for dietary polyphenols and vitamins C and E, using their cupric ion reducing capability in the presence of neocuproine: CUPRAC method. Journal of Agricultural and Food Chemistry 52 (2004) 7970–7981.
 32. Kumar KS, Ganesan K, Rao PS. Antioxidant potential of solvent extracts of *Kappaphycus alvarezii* (Doty) Doty—An edible seaweed. Food Chemistry 107 (2008) 289–295.
 33. El-Aty AMA, Mohamed AA, Samhan FA. In vitro antioxidant and antibacterial activities of two fresh water Cyanobacterial species, *Oscillatoria agardhii* and *Anabaena sphaerica*. Journal of Applied Pharmaceutical Science, 4 (2014) 69–75.
 34. Mancini-Filho J, Vidal-Novoa A., Silva, AMO. Antioxidant properties of algal components and fractions. In Herminia Dommiguez (Eds.) Functional Ingredients from Algae for Foods and Nutraceuticals, Woodhead Publishing Series in Food Science, Technology and Nutrition: Number 256, pp. 255–286, 2013.
 35. Benzie IF. An automated, specific, spectrophotometric method for measuring ascorbic acid in plasma (EFTSA). Clinical Biochemistry. 29 (1996) 111–116.

Selfadjoint Singular Quasi-Differential Operators of First Order

Zameddin I. Ismailov¹  Pembe Ipek AI² 

¹Karadeniz Technical University, Department of Mathematics, Trabzon, Turkey

²Karadeniz Technical University, Institute of Natural Sciences, Trabzon, Turkey

ABSTRACT

In this work, using the Calkin-Gorbachuk method firstly all selfadjoint extensions of the minimal operator generated by first order linear singular quasi-differential expression in the weighted Hilbert space of vector-functions on right semi-axis have been described. Lastly, the structure of the spectrum set of these extensions has been investigated.

Keywords:

Selfadjoint operator; Quasi-differential operator; Spectrum.

AMS 2010 Subject Classification:

47A10, 47B25

INTRODUCTION

In the first years of previous century, J. von Neumann [13] and M. H. Stone [12] investigated the theory of selfadjoint extensions of linear densely defined closed symmetric operators in a Hilbert spaces. Applications to scalar linear even order symmetric differential operators and description of all selfadjoint extensions in terms of boundary conditions were done by I. M. Glazman in his seminal work [5] and by M. A. Naimark [10] in his book. In this sense the famous Glazman-Krein-Naimark (or Everitt-Krein-Glazman-Naimark) Theorem in mathematical literature should be noted. In mathematical literature there is another so-called Calkin-Gorbachuk method (see [6], [11]).

Our motivation in this paper originates from the interesting researches of W. N. Everitt, L. Markus, A. Zettl, J. Sun, D. O'Regan, R. Agarwal [2], [3], [4], [14] in scalar cases. Throughout this paper A. Zettl's and J. Sun's view about these topics is to be taken into consideration in [14]: A selfadjoint ordinary differential operator in Hilbert space is generated by two things:

- (1) a symmetric (formally selfadjoint) differential expression;
- (2) a boundary condition which determined selfadjoint differential operators.

Article History:

Received: 2018/02/14

Accepted: 2018/08/12

Online: 2019/01/31

Correspondence to: Pembe Ipek AI,
Karadeniz Technical University, Institute of
Natural Sciences, 61080, Trabzon, Turkey
E-Mail: ipekpembe@gmail.com
Phone: +90 542 253 66 20

And also for a given selfadjoint differential operator, a basic question is: What is its spectrum?

In this work, in Section 3 the representation of all selfadjoint extensions of a symmetric quasi-differential operator, generated by first order symmetric quasi-differential expression in the weighted Hilbert space of vector-functions defined at the right semi-axis in terms of boundary conditions have been described. In Section 4, the structure of spectrum of these selfadjoint extensions is investigated.

STATEMENT OF THE PROBLEM

In the weighted Hilbert space $L_w^\alpha(H, (a, \infty))$ where H is a separable Hilbert space and $\alpha \in \mathbb{R}$, we will consider the following quasi-differential expression given by

$$l(u) = i \frac{\alpha(t)}{w(t)} (\alpha u)'(t) + Au(t).$$

Here

$$(1) \quad \alpha, w : (a, \infty) \rightarrow (0, \infty),$$

$$(2) \quad \alpha, w \in C(a, \infty),$$

$$(3) \quad \int_a^\infty \frac{w(s)}{\alpha^2(s)} ds < \infty,$$

$$(4) \quad A : D(A) \subset H \rightarrow H \text{ is a selfadjoint operator.}$$

In this case, since

$$\begin{aligned} & (l(u), v)_{L_w^2(H, (a, \infty))} \\ &= \int_a^\infty \left(i \frac{\alpha(t)}{w(t)} (\alpha u)'(t), v(t) \right)_H w(t) dt + (Au, v)_{L_w^2(H, (a, \infty))} \\ &= i \int_a^\infty \left((\alpha u)'(t), (\alpha v)(t) \right)_H dt + (u, Av)_{L_w^2(H, (a, \infty))} \\ &= i \left[(\alpha u, \alpha v)(\infty) - (\alpha u, \alpha v)(a) \right] \\ &\quad - i \int_a^\infty \left((\alpha u)(t), (\alpha v)'(t) \right)_H dt + (u, Av)_{L_w^2(H, (a, \infty))} \\ &= \int_a^\infty \left(u(t), i \frac{\alpha(t)}{w(t)} (\alpha v)'(t) \right)_H w(t) dt + (u, Av)_{L_w^2(H, (a, \infty))} \\ &= (u, l^+(v))_{L_w^2(H, (a, \infty))} \\ &= (u, l(v))_{L_w^2(H, (a, \infty))}, \end{aligned}$$

then the differential-operator expression $l(\cdot)$ is formally symmetric.

The minimal L_0 and maximal L operators corresponding to differential-operator expression in $L_w^2(H, (a, \infty))$ can be defined by using the classical techniques (see [7]).

On the other hand one can easily see that

$$\begin{aligned} D(L) &= \{u \in L_w^2(H, (a, \infty)) : l(u) \in L_w^2(H, (a, \infty))\}, \\ D(L_0) &= \{u \in D(L) : (\alpha u)(a) = (\alpha u)(\infty) = 0\}. \end{aligned}$$

DESCRIPTION OF SELFADJOINT EXTENSIONS

In this section using the Calkin-Gorbachuk method we will investigate the general representation of all selfadjoint extensions of the minimal operator L_0 .

First, let us prove the following assertion.

Lemma 3.1 The deficiency indices of the minimal operator L_0 in $L_w^2(H, (a, \infty))$ are in form

$$(n_+(L_0), n_-(L_0)) = (\dim H, \dim H).$$

Proof. For the simplicity of calculations it will be taken $A=0$. It is clear that the general solutions of differential equations

$$i \frac{\alpha(t)}{w(t)} (\alpha u_\pm)'(t) \pm i u_\pm(t) = 0, t > a$$

can be given as

$$u_\pm(t) = \frac{1}{\alpha(t)} \exp\left(\mp \int_a^t \frac{w(s)}{\alpha^2(s)} ds\right) f, f \in H, t > a.$$

From these representations we have

$$\begin{aligned} & \|u_+\|_{L_w^2(H, (a, \infty))}^2 \\ &= \int_a^\infty w(t) \|u_+(t)\|_H^2 dt \\ &= \int_a^\infty \left\| \frac{1}{\alpha(t)} \exp\left(-\int_a^t \frac{w(s)}{\alpha^2(s)} ds\right) f \right\|_H^2 w(t) dt \\ &= \int_a^\infty \frac{w(t)}{\alpha^2(t)} \exp\left(-2\int_a^t \frac{w(s)}{\alpha^2(s)} ds\right) dt \|f\|_H^2 \\ &= \int_a^\infty \exp\left(-2\int_a^t \frac{w(s)}{\alpha^2(s)} ds\right) d\left(\int_a^t \frac{w(s)}{\alpha^2(s)} ds\right) \|f\|_H^2 \\ &= \frac{1}{2} \left(1 - \exp\left(-2\int_a^\infty \frac{w(s)}{\alpha^2(s)} ds\right)\right) \|f\|_H^2 < \infty. \end{aligned}$$

Consequently, $n_+(L_0) = \dim \ker(L + iE) = \dim H$.

On the other hand, it is clear that for any $f \in H$, one can obtain

$$\begin{aligned} & \|u_-\|_{L_w^2(H, (a, \infty))}^2 \\ &= \int_a^\infty w(t) \|u_-(t)\|_H^2 dt \\ &= \int_a^\infty \frac{w(t)}{\alpha^2(t)} \exp\left(2\int_a^t \frac{w(s)}{\alpha^2(s)} ds\right) dt \|f\|_H^2 \\ &= \int_a^\infty \exp\left(2\int_a^t \frac{w(s)}{\alpha^2(s)} ds\right) d\left(\int_a^t \frac{w(s)}{\alpha^2(s)} ds\right) \|f\|_H^2 \\ &= \frac{1}{2} \left(\exp\left(2\int_a^\infty \frac{w(s)}{\alpha^2(s)} ds\right) - 1\right) \|f\|_H^2 < \infty. \end{aligned}$$

Consequently, $n_-(L_0) = \dim \ker(L - iE) = \dim H$. This completes the proof.

As a result, the minimal operator L_0 has at least one selfadjoint extension (see [6]).

In order to describe these extensions we need to obtain the space of boundary values.

Definition 3.2 [6] Let \mathcal{H} be any Hilbert space and $S : D(S) \subset \mathcal{H} \rightarrow \mathcal{H}$ be a closed densely defined symmetric operator in the Hilbert space \mathcal{H} having equal finite or infinite deficiency indices. A triplet $(\mathbf{H}, \gamma_1, \gamma_2)$ where \mathbf{H} is a Hilbert space, γ_1 and γ_2 are linear mappings from $D(S^*)$ into \mathbf{H} , is called a space of boundary values for the operator S if for any $f, g \in D(S^*)$

$$\begin{aligned} & (S^* f, g)_\mathcal{H} - (f, S^* g)_\mathcal{H} \\ &= (\gamma_1(f), \gamma_2(g))_\mathbf{H} - (\gamma_2(f), \gamma_1(g))_\mathbf{H} \end{aligned}$$

while for any $F_1, F_2 \in \mathbf{H}$, there exists an element $f \in D(S^*)$

such that $\gamma_1(f) = F_1$ and $\gamma_2(f) = F_2$.

Lemma 3.3 The triplet (H, γ_1, γ_2) ,

$$\begin{aligned} \gamma_1 : D(L) \rightarrow H, \gamma_1(u) &= \frac{1}{\sqrt{2}}((\alpha u)(\infty) - (\alpha u)(a)), \\ \gamma_2 : D(L) \rightarrow H, \gamma_2(u) &= \frac{1}{i\sqrt{2}}((\alpha u)(\infty) + (\alpha u)(a)) \\ , u \in D(L) \end{aligned}$$

is a space of boundary values of the minimal operator L_0 in $L_w^2(H, (a, \infty))$.

Proof. For any $u, v \in D(L)$,

$$\begin{aligned} & (Lu, v)_{L_w^2(H, (a, \infty))} - (u, Lv)_{L_w^2(H, (a, \infty))} \\ &= \left(i \frac{\alpha}{w} (\alpha u)' + Au, v \right)_{L_w^2(H, (a, \infty))} \\ & \quad - \left(u, i \frac{\alpha}{w} (\alpha v)' + Av \right)_{L_w^2(H, (a, \infty))} \\ &= \left(i \frac{\alpha}{w} (\alpha u)', v \right)_{L_w^2(H, (a, \infty))} - \left(u, i \frac{\alpha}{w} (\alpha v)' \right)_{L_w^2(H, (a, \infty))} \\ &= \int_a^\infty \left(i \frac{\alpha(t)}{w(t)} (\alpha u)'(t), v(t) \right)_H w(t) dt \\ & \quad - \int_a^\infty \left(u(t), i \frac{\alpha(t)}{w(t)} (\alpha v)'(t) \right)_H w(t) dt \\ &= i \left[\int_a^\infty ((\alpha u)'(t), (\alpha v)(t))_H dt + \int_a^\infty ((\alpha u)(t), (\alpha v)'(t))_H dt \right] \\ &= i \int_a^\infty ((\alpha u)(t), (\alpha v)(t))_H' dt \\ &= i \left[((\alpha u)(\infty), (\alpha v)(\infty))_H - ((\alpha u)(a), (\alpha v)(a))_H \right] \\ &= (\gamma_1(u), \gamma_2(v))_H - (\gamma_2(u), \gamma_1(v))_H. \end{aligned}$$

Now for any given element $f, g \in H$ one can find the function $u \in D(L)$ such that

$$\begin{aligned} \gamma_1(u) &= \frac{1}{\sqrt{2}}((\alpha u)(\infty) - (\alpha u)(a)) = f, \\ \gamma_2(u) &= \frac{1}{i\sqrt{2}}((\alpha u)(\infty) + (\alpha u)(a)) = g. \end{aligned}$$

From this it is obtained that $(\alpha u)(\infty) = (ig + f) / \sqrt{2}$ and $(\alpha u)(a) = (ig - f) / \sqrt{2}$.

If we choose the function $u(\cdot)$ as below

$$\begin{aligned} u(t) &= \frac{1}{\alpha(t)} (1 - e^{-at}) (ig + f) / \sqrt{2} \\ &+ \frac{1}{\alpha(t)} e^{-at} (ig - f) / \sqrt{2} \end{aligned}$$

then it is clear that $u \in D(L)$ and $\gamma_1(u) = f, \gamma_2(u) = g$.

The following result can be established by using the method given in [6].

Theorem 3.4 If \tilde{L} is a selfadjoint extension of the minimal operator L_0 in $L_w^2(H, (a, \infty))$, then it is generated by the differential-operator expression $l(\cdot)$ and boundary condition

$$(\alpha u)(a) = W(\alpha u)(\infty),$$

where $W : H \rightarrow H$ is a unitary operator. Moreover, the unitary operator W in H is determined uniquely by the extension \tilde{L} , i.e. $\tilde{L} = L_W$ and vice versa.

Proof. It is known that all selfadjoint extension of the minimal operator L_0 are described by the differential-operator expression $l(\cdot)$ with boundary condition

$$(V - E)\gamma_1(u) + i(V + E)\gamma_2(u) = 0,$$

where $V : H \rightarrow H$ is a unitary operator. Therefore from Lemma 3.3 we obtain

$$\begin{aligned} & (V - E)((\alpha u)(\infty) - (\alpha u)(a)) \\ & + (V + E)((\alpha u)(\infty) + (\alpha u)(a)) = 0, u \in D(\tilde{L}). \end{aligned}$$

From this, it implies that

$$(\alpha u)(a) = -V(\alpha u)(\infty).$$

Choosing $W = -V$ in last boundary condition, we have

$$(\alpha u)(a) = W(\alpha u)(\infty).$$

THE SPECTRUM OF THE SELFADJOINT EXTENSIONS

In this section the structure of the spectrum set of the selfadjoint extensions of the minimal operator L_0 in $L_w^2(H, (a, \infty))$ will be examined.

Theorem 4.1 The spectrum of any selfadjoint extension L_W is in form

$$\begin{aligned} \sigma(L_W) &= \left\{ \lambda \in \mathbb{R} : \lambda = \left(\int_a^\infty \frac{w(s)}{\alpha^2(s)} ds \right)^{-1} (arg \mu + 2n\pi) \right. \\ & \left. \mu \in \sigma \left(W \exp \left(iA \int_a^\infty \frac{w(s)}{\alpha^2(s)} ds \right) \right), n \in \mathbb{Z} \right\}. \end{aligned}$$

Proof. Consider the following problem to spectrum of the extension L_W , i.e.

$$\begin{aligned} l(u) &= \lambda u + f, u, f \in L_w^2(H, (a, \infty)), \lambda \in \mathbb{R}, \\ (\alpha u)(a) &= W(\alpha u)(\infty), \end{aligned}$$

that is,

$$i \frac{\alpha(t)}{w(t)} (\alpha u)'(t) + Au(t) = \lambda u(t) + f(t), t > a,$$

$$(\alpha u)(a) = W(\alpha u)(\infty).$$

The general solution of the last differential equation,

$$(\alpha u)'(t) = i \frac{w(t)}{\alpha^2(t)} (A - \lambda E)(\alpha u)(t) - i \frac{w(t)}{\alpha(t)} f(t)$$

is in form

$$u(t; \lambda) = \frac{1}{\alpha(t)} \exp \left(i(A - \lambda E) \int_a^t \frac{w(s)}{\alpha^2(s)} ds \right) f_\lambda$$

$$+ \frac{i}{\alpha(t)} \int_a^t \exp \left(i(A - \lambda E) \int_s^t \frac{w(\tau)}{\alpha^2(\tau)} d\tau \right) \frac{w(s)}{\alpha(s)} f(s) ds,$$

$$f_\lambda \in H, t > a.$$

In this case

$$\left\| \frac{1}{\alpha(t)} \exp \left(i(A - \lambda E) \int_a^t \frac{w(s)}{\alpha^2(s)} ds \right) f_\lambda \right\|_{L_w^2(H, (a, \infty))}^2$$

$$= \int_a^\infty \frac{w(t)}{\alpha^2(t)} dt \|f_\lambda\|_H^2 < \infty$$

and

$$\left\| \frac{i}{\alpha(t)} \int_a^t \exp \left(i(A - \lambda E) \int_s^t \frac{w(\tau)}{\alpha^2(\tau)} d\tau \right) \frac{w(s)}{\alpha(s)} f(s) ds \right\|_{L_w^2(H, (a, \infty))}^2$$

$$= \int_a^\infty \frac{1}{\alpha^2(t)} \left\| \int_a^t \exp \left(i(A - \lambda E) \int_s^t \frac{w(\tau)}{\alpha^2(\tau)} d\tau \right) \frac{w(s)}{\alpha(s)} f(s) ds \right\|_H^2 w(t) dt$$

$$\leq \int_a^\infty \frac{1}{\alpha^2(t)} \left[\int_a^t \left\| \exp \left(i(A - \lambda E) \int_s^t \frac{w(\tau)}{\alpha^2(\tau)} d\tau \right) \right\|_H \left\| \frac{w(s)}{\alpha(s)} f(s) \right\|_H ds \right]^2 w(t) dt$$

$$\leq \int_a^\infty \frac{1}{\alpha^2(t)} \left(\int_a^t \frac{\sqrt{w(s)}}{\alpha(s)} \sqrt{w(s)} \|f(s)\|_H ds \right)^2 w(t) dt$$

$$\leq \int_a^\infty \frac{1}{\alpha^2(t)} \left(\int_a^t \frac{w(s)}{\alpha^2(s)} ds \right) \left(\int_a^t w(s) \|f(s)\|_H^2 ds \right) w(t) dt$$

$$\leq \int_a^\infty \frac{w(t)}{\alpha^2(t)} dt \int_a^\infty \frac{w(s)}{\alpha^2(s)} ds \int_a^\infty w(s) \|f(s)\|_H^2 ds$$

$$\leq \left(\int_a^\infty \frac{w(t)}{\alpha^2(t)} dt \right)^2 \|f\|_{L_w^2(H, (a, \infty))}^2 < \infty.$$

Hence, $u(\cdot, \lambda) \in L_w^2(H, (a, \infty))$ for $\lambda \in \mathbb{R}$.

From this and boundary condition, we have

$$\left(E - W \exp \left(i(A - \lambda E) \int_a^\infty \frac{w(s)}{\alpha^2(s)} ds \right) \right) f_\lambda$$

$$= -i \int_a^\infty \exp \left(i(A - \lambda E) \int_s^a \frac{w(\tau)}{\alpha^2(\tau)} d\tau \right) \frac{w(s)}{\alpha(s)} f(s) ds.$$

Therefore in order to $\lambda \in \sigma(L_w)$ the necessary and sufficient condition is

$$\exp \left(i \lambda \int_a^\infty \frac{w(s)}{\alpha^2(s)} ds \right) = \mu \in \sigma \left(W \exp \left(i A \int_a^\infty \frac{w(s)}{\alpha^2(s)} ds \right) \right).$$

Since the operator $W \exp \left(i A \int_a^\infty \frac{w(s)}{\alpha^2(s)} ds \right)$ is an isometric operator, then $|\mu| = 1$.

Consequently,

$$\lambda \int_a^\infty \frac{w(s)}{\alpha^2(s)} ds = \arg \mu + 2n\pi, n \in \mathbb{Z}.$$

On the other hand since $\int_a^\infty \frac{w(s)}{\alpha^2(s)} ds > 0$, then

$$\lambda = \left(\int_a^\infty \frac{w(s)}{\alpha^2(s)} ds \right)^{-1} (\arg \mu + 2n\pi),$$

$$\mu \in \sigma \left(W \exp \left(i A \int_a^\infty \frac{w(s)}{\alpha^2(s)} ds \right) \right), n \in \mathbb{Z}.$$

This completes the proof.

Remark 4.2 Note that the similar problems in different singular multipoint cases in the corresponding direct sums of Hilbert spaces of vector-functions have been investigated in [1], [8], [9].

References

1. Bairamov E, Öztürk Mert R, Ismailov Z. Selfadjoint extensions of a singular differential operator. Journal of Mathematical Chemistry 50 (2012) 1100-1110.
2. El-Gebeily MA, O'Regan D, Agarwal R. Characterization of self-adjoint ordinary differential operators. Mathematical and Computer Modelling 54 (2011) 659-672.
3. Everitt WN, Markus L. The Glazman-Krein-Naimark Theorem for ordinary differential operators. Operator Theory, Advances and Applications 98 (1997) 118-130.
4. Everitt WN, Poulkou A. Some observations and remarks on differential operators generated by first order boundary value problems. Journal of Computational and Applied Mathematics 153 (2003) 201-211.
5. Glazman IM. On the theory of singular differential operators.

- Uspekhi Matematicheskikh Nauk 40 (1962) 102-135, (English translation in American Mathematical Society Translations 4 (1962) 331-372).
6. Gorbachuk VI, Gorbachuk MI. Boundary Value Problems for Operator Differential Equations, Mathematics and its Applications, Kluwer, Dordrecht, 1991.
 7. Hörmander L. On the theory of general partial differential operators. Acta Mathematica 94 (1955) 161-248.
 8. Ismailov ZI, Öztürk Mert R. Selfadjoint extensions of a singular multipoint differential operator of first Order. Electronic Journal of Differential Equations 129 (2013) 1-11.
 9. Ismailov ZI, Yılmaz B, Öztürk Mert R. On the spectrum of some class of selfadjoint singular differential operators. Communications Faculty of Sciences University of Ankara Series A1: Mathematics and Statistics 65 (2016) 137-145.
 10. Naimark MA. Linear Differential Operators II, NewYork, Ungar, 1968.
 11. Rofe-Beketov FS, Kholkin AM. Spectral Analysis of Differential Operators, World Scientific Monograph Series in Mathematics 7, USA, 2005.
 12. Stone MH. Linear Transformations in Hilbert Space and Their Applications in Analysis, American Mathematical Society Colloquium Publications 15, USA, 1932.
 13. von Neumann J. Allgemeine eigenwerttheories hermitescher funktionaloperatoren. Mathematische Annalen 102 (1929-1930) 49-31.
 14. Zettl A, Sun J. Survey Article: Self-adjoint ordinary differential operators and their spectrum. Rosky Mountain Journal of Mathematics 45 1 (2015) 763-886.

Synthesis, Characterization, Swelling Behavior and Metal Uptake Studies of Dichloroglyoxime Crosslinked Chitosan Derivative

Mahir Timur 

Altinozu Vocational School, Mustafa Kemal University, Hatay, Turkey

ABSTRACT

New crosslinked derivative of chitosan was prepared by the condensation reaction of chitosan (CS) and dichloro glyoxime. Structural analysis of chitosan derivative (CSL) was performed by elemental analysis (C, H, N), SEM measurements, FT-IR, solid-state ¹³C CP/MAS NMR, XRD-powder and TGA. Crosslinking ratio was determined from the elemental analysis by using the C/N and found to be 70%. The swelling behavior of derivative was investigated on pH 3-7 and 10 at 25 and 37°C. Metal ion uptake capacity was studied towards of selected transition metals Cu(II), Ni(II), Co(II), Fe(II) and (Cd(II) cations in aqueous medium. According to the results of the analyses; water retention capacity and metal uptake capacity of new cross-linked chitosan derivative is higher than chitosan and metal uptake sequence are Cu(II) > Fe(II) > Cd(II) > Co(II) > Ni(II) respectively.

Article History:

Received: 2018/02/26

Accepted: 2018/04/07

Online: 2019/01/31

Correspondence to: Mahir Timur,
Altinozu Vocational School,
Mustafa Kemal University, Hatay,
Turkey

E-mail: mahirtimur@gmail.com

Phone: +90 505 545 13 72:

Fax: +90 326 311 22 75

Keywords:

Crosslink; Chitosan; Swelling; Metal-ion uptake

INTRODUCTION

Hydrogels are physically or chemically cross-linked hydrophilic polymeric structures. They are absorb a large amount of water (or fluids) and swell [1]. The hydrogels are separated into two groups, natural (biopolymer based) and synthetically [2]. Today, there is growing interest to hydrogels due to their, biocompatibility, biodegradability and tissue mimicking properties. [3].

Biopolymers are derived from natural materials such as crustaceans, fungi and wood. Among the biopolymers, Chitosan has great potential in hydrogel preparation. [4].

Chitosan biopolymer is an amino polysaccharide which is biocompatible, biodegradable, non-toxic and

also antimicrobial. It is open to chemical and mechanical modification in order to gain new features and functions [5,6].

Chitin and CS are important biopolymers because of the presence of the amino groups, they can be easily derivatized to desired reactive properties, biological compounds and soluble polymers [7,8].

The derivatization of chitosan can increase the complexing capacity of chitosan with metals, which enhances the adsorption properties of chitosan. [9,10].

Cross-linked polymers with the ability to swell by holding more solvent than 20% of their mass are termed xerogel. When the solvent is water, these crosslinked

structures take the name of hydrogel [11].

Hydrogels in the aqueous medium swell by holding water. Due to this ability they are used in adsorbing on areas such as water purification, heavy metal removal, dewatering, controlled release of fertilizers and medicines, ion exchange applications, chromatographic applications, solvent extraction, removal of water from industrial wastes containing petroleum and oil, and prevention of corrosion in telecommunication [12,13].

It is important to examine swelling properties in the characterization of cross-linked polymers that exhibit swelling behavior. For this purpose, it must first be created in the swelling curves. Swelling curves are formed by monitoring changes in the mass or volume of the polymer containing the appropriate solvent over time [14,15].

At acidic pH (3.5-5.5), the complex formation between the metal ion and the chitosan derivative reduce as the free amine groups of the chitosan are protonated [16]. Amino groups are present as free amines at pH 6.5-7.0 and the metal retention capacity of the chitosan derivative increases as the phenolic OH groups which may be present in the chitosan derivative at this pH value are deprotonated [16,17].

The aim of this work is crosslink of chitosan with dichloroglyoxime and characterization of this new crosslinked chitosan derivative. In addition, we aimed to investigate their metal ions uptake capacities and examination of swelling behaviors as application parts of this study.

MATERIALS AND METHODS

Materials

Dichloro glyoxime was synthesized and purified according to reported literature procedure [18].

Crosslinked chitosan derivative was prepared from dichloroglyoxime and chitosan. All reagents and solvents

were reagent-grade quality and they were obtained from commercial suppliers and were purified before use.

Stock solutions of Cu(II), Ni(II), Co(II), Fe(II) and Cd(II) were prepared by dissolving the analytical grade metal salt in deionized water.

C, H and N elemental analyses of the compounds were made with LECO-CHNS-932. FTIR analysis was carried out with Perkin Elmer spectrum two FTIR spectrophotometer, equipped with a diamond tipped ATR accessory. The cell was cleaned with acetone after each spectrum. ^{13}C NMR spectrum was obtained by a Bruker Superconducting FT/NMR Spectrometer Avance TM 300 MHz WB with CP/MAS technique (cross-polarization, magic-angle-spinning). The X-ray diffraction patterns of sample were recorded at room temperature on a using a Rigaku System RadB X-Ray Diffractometer, using monochromated Cu $\text{K}\alpha$ radiation in the range $2-40^\circ$ (2θ), at 25°C . Thermogravimetric analysis (TGA) of the sample was performed with DuPont 951 thermal analyzer under air atmosphere, heated from 20°C to 800°C at a heating rate of $10^\circ\text{C min}^{-1}$. Morphological analysis of images obtained by the scanning electron microscopy JEOL 5500 / OXFORD Inca-X (SEM). Metal analyses were carried out by MP-AES: Agilent 4100.

Methods

Synthesis of Crosslinked Chitosan Derivative (CSL)

1 g Chitosan was stirred in a 1% solution of 100 ml of acetic acid at 60°C for 1 hour to obtain a homogeneous mixture. To the resulting chitosan solution, solution of dichloroglyoxime (5.83 mmol, 0.91 g) in 50 mL of ethanol was added and boiled under reflux for 12 hours. The temperature of the solution was reduced to room temperature by stirring and at the end the mixture was precipitated in the form of Chitosan derivative gel by adding 1 M NaHCO_3 . The gel was filtered and dried at 70°C in vacuum oven. The gel was purified by soxhlet extraction using ethanol as solvent.

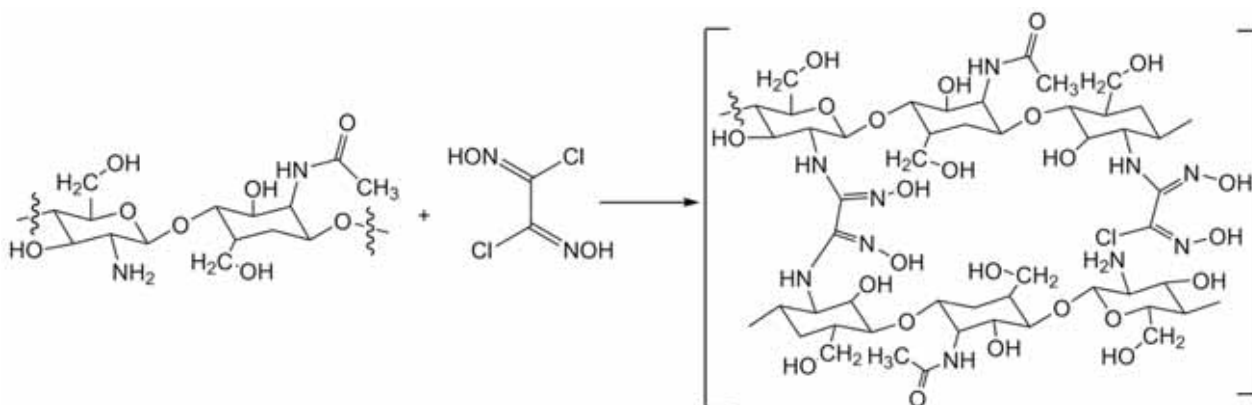


Figure 1. Synthesis of crosslinked chitosan derivative

The synthetic route is shown in Fig. 1. chitosan amine group displaced the chloride of dichloro glyoxime and gave the desired crosslinked product.

Metal Ion Uptake Studies

Study of metal ion uptake was performed at 25 °C by batch technique in aqueous metal solutions. The CSL powder was added to a known volume and concentration of the metal solution and the heterogeneous mixture was agitated two hours over orbital shaker. pH of the solution was adjusted using acetic acid/sodium acetate buffer for pH 6.

The studies were carried out by shaking 50 mg of CSL in 50 ml of 100 ppm Cu(II), Ni(II), Cd(II), Co(II) and Fe(II) solutions on an orbital shaker in buffered medium for three hours at 25 °C. After that, the suspension was filtered and diluted (1:20) and amounts of metal ions in the filtrate were determined by MP-AES.

As a result of MP-AES analysis the contents of Cu(II), Co(II), Ni(II), Cd(II) and Fe(II) in the diluted filtrate were found as 0.26; 2.86; 3.05; 1.65 and 1.10 ppm respectively.

According to the calculations, percent of the metal uptake of Cu(II), Co(II), Ni(II), Cd(II) and Fe(II) were found as: 94.80%; 42.80%; 39.00%; 67.00% and 78.00% and the amount of metal for per gram CSL was found as: 94.8; 42.8; 39.00; 67.00 and 78.00 mg/g respectively.

Swelling Studies

The swelling experiments of the derivative were carried out in the water medium at 25 and 37 °C and pH 3.0, 7.0 and 10.0. 0.1 M NaOH and 0.1 M HCl were used to prepare the pH solutions. The samples were weighed at a sensitivity of 0.0001 g and placed in a water environment sensitive to ± 0.1 °C. When the hydrogel was left in the solution, t=0 was taken and the hydrogel removed from the water at certain time intervals was dried and weighed. After 180 minutes, the experiment was terminated because of the swelling slowed.

RESULTS AND DISCUSSION

Solubility

Chitosan is insoluble in water, organic solvents and aqueous bases, but soluble in acids such as acetic, nitric, hydrochloric, perchloric and phosphoric acid. [8,19].

As a result of the derivatization, the solubility of the chitosan derivative decrease due to the decrease of free amine groups by cross-linking of chitosan. Consequently, crosslinked chitosan derivative lesser soluble in acids than chitosan.

Elemental Analyses

The C, H and N elemental analysis results of CS and CSL were given in Table 1 and the C/N ratio was calculated and added to the chart. In the chitosan derivative, C% and H% content were remained constant and N% was increased due to the dioxime compound (include nitrogen atom) entering the reaction. This change is more easily detected by calculating C/N ratios. Therefore, it can be easily understood the reason of the decrease in the carbon to nitrogen ratio (C/N).

When the C/N ratios were examined, it was seen that the C/N ratio of CSL is lower than chitosan. This shows that the new chitosan derivative was obtained.

We can determine the degree of cross-linking and the rate of realization by substitution degree. The number of carbonyls attached to each NH₂ group in the chitosan was calculated as the binding degree (DS) by the following equation [20].

$$DS = \frac{a(C/N)_m - (C/N)_0}{n} \quad (1)$$

(C/N)_m is the derivatized chitosan C/N ratio, (C/N)₀ is the initial chitosan C/N ratio, 'a' and 'n' are the number of nitrogen and carbon contained after the chitosan has been modified, respectively. The substitution degree (DS) of CSL was calculated as 72.11%. Table 1.

Table 1. Operating conditions of the gas turbine power plant at -1 °C

	%C	%H	%N	C/N	DS	a	n
CS	40.95	6.96	7.41	5.53			
CSL	39.67	6.63	7.46	5.31	72.11	2	7

FT-IR spectra

In order to characterize the CSL, a spectrum of chitosan was also recorded. The main bands appearing in the IR spectra of the oxime compounds, the C=N stretching vibrations in the range of 1600-1665 cm⁻¹, the N-O vibration in the range of 940-885 cm⁻¹ and the O-H vibration in the range of 3500-3200 cm⁻¹ which were overlapped to the stretching vibration of N-H [21,22]. The vibrations in the range of 1680-1480 cm⁻¹ are attributed to amide (C=O), the vibrations in the range from 1160 cm⁻¹ to 1000 cm⁻¹, the bands near 1080-1025 cm⁻¹ are attributed to etheric CO and the peak at ~890 cm⁻¹ corresponds to wagging of the saccharide structure of chitosan appear [23,24].

It was observed that the FTIR spectra of chitosan (CS) and CSL were different from each other when they were compared. Despite the overlapping the peaks that the secondary amide band (1645 cm⁻¹), stretching vibrations of

OH groups and primary amine ($3500 - 3000 \text{ cm}^{-1}$) and CH deformation of the β -glycosidic bond ($\sim 890 \text{ cm}^{-1}$) of chitosan with the C=N band ($1600-1665 \text{ cm}^{-1}$), the N-O vibration bands ($940-885 \text{ cm}^{-1}$) and the O-H vibration bands ($3500-3200 \text{ cm}^{-1}$) of the glyoxime respectively.

The FT-IR spectra of CS and CSL are shown in Fig. 2. In the spectrum of the CSL, the NH stretching vibrations of chitosan disappeared and OH stretching vibrations were observed as a broad band in the range from 3000 to 3600 cm^{-1} , and the 1651 band shifted to 1658 cm^{-1} which can be attributed to the C=N of azomethine group respectively. These changes in the peaks show that the synthesis takes place.

On the other hand, similar spectra are obtained for the CSL-metals.

Morphology

The scanning electron micrographs (SEM) of chitosan (a) and CSL (b) were given in Fig. 3.

Chitosan film has a smooth surface. The SEM micrographs were indicating to significant differences among morphologies of chitosan and CSL. Therefore, these differences can be attributed to the formation of CSL.

X-Ray diffraction (XRD) study

The XRD spectra of pure chitosan (CS) and CSL were given in Fig. 4. It was previously reported that, CS exhibits

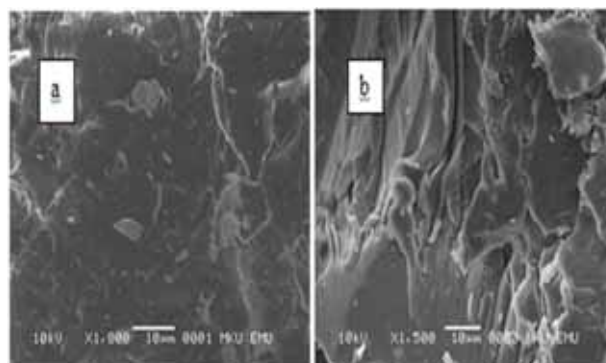


Figure 3. The scanning electron micrographs (SEM) of chitosan (a) and CSL (b)

two sharp crystalline peaks at $2\theta = 10^\circ$ and $2\theta = 20^\circ$ [25]. In the XRD patterns of CSL, the intensity of peaks decreased and broadening of the peaks was observed when compared with the free chitosan. These results suggest that CSL has less crystalline and more amorphous structure than the pure chitosan.

It is known that intermolecular and intramolecular hydrogen bondings which form between amino group and a hydroxyl group stabilize the crystalline structure of chitosan.

Crystallinity decreases by the deformation of some of inter and intramolecular hydrogen bonds, because of both the decreasing free amino group and steric hindrance after crosslinking [26-28].

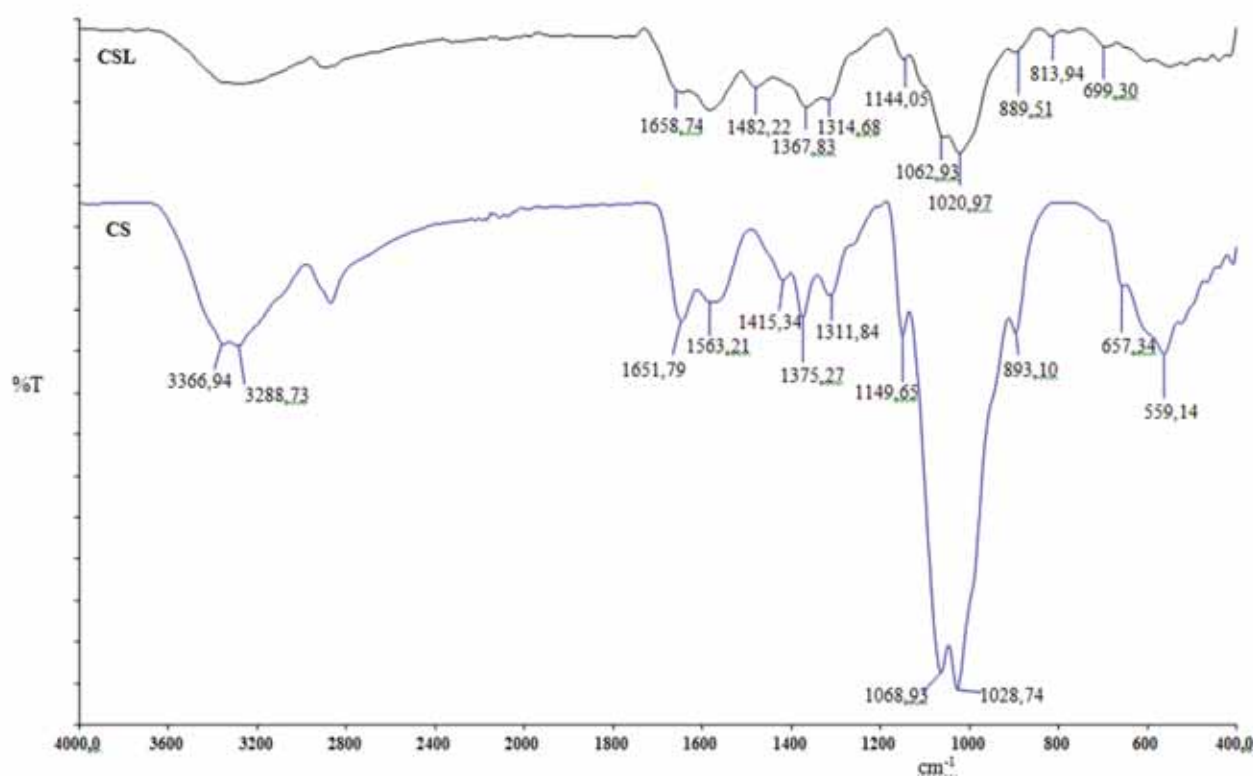


Figure 2. FT-IR spectra of CS and CSL

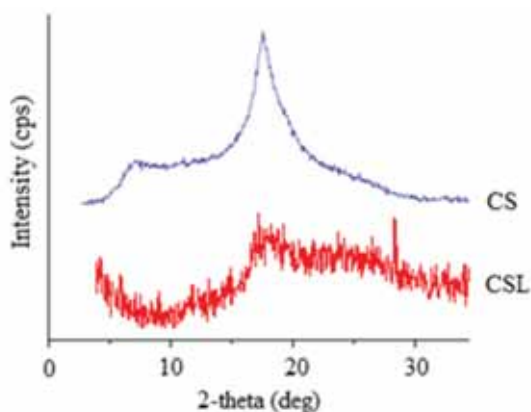


Figure 4. XRD Diffractograms of chitosan and its derivative

¹³C NMR analysis

¹³C CP-MAS solid-state NMR chemical shift values of chitosan were observed at 23 ppm (-CH₃), 58 ppm (C2), 61 ppm (C6), 76 ppm (C5,C3), 85 ppm (C4), 106 ppm (C1), 174 ppm (C=O) [29] and dichloroglyoxime azomethine (C=N) carbon were observed in the range 150-160 ppm [30,31].

When compared CSL with chitosan, in addition to the peaks of chitosan, observation of the azomethine peak of glyoxime at 160 ppm (azomethine C=N), confirming the formation of crosslinked chitosan derivative (Fig. 5).

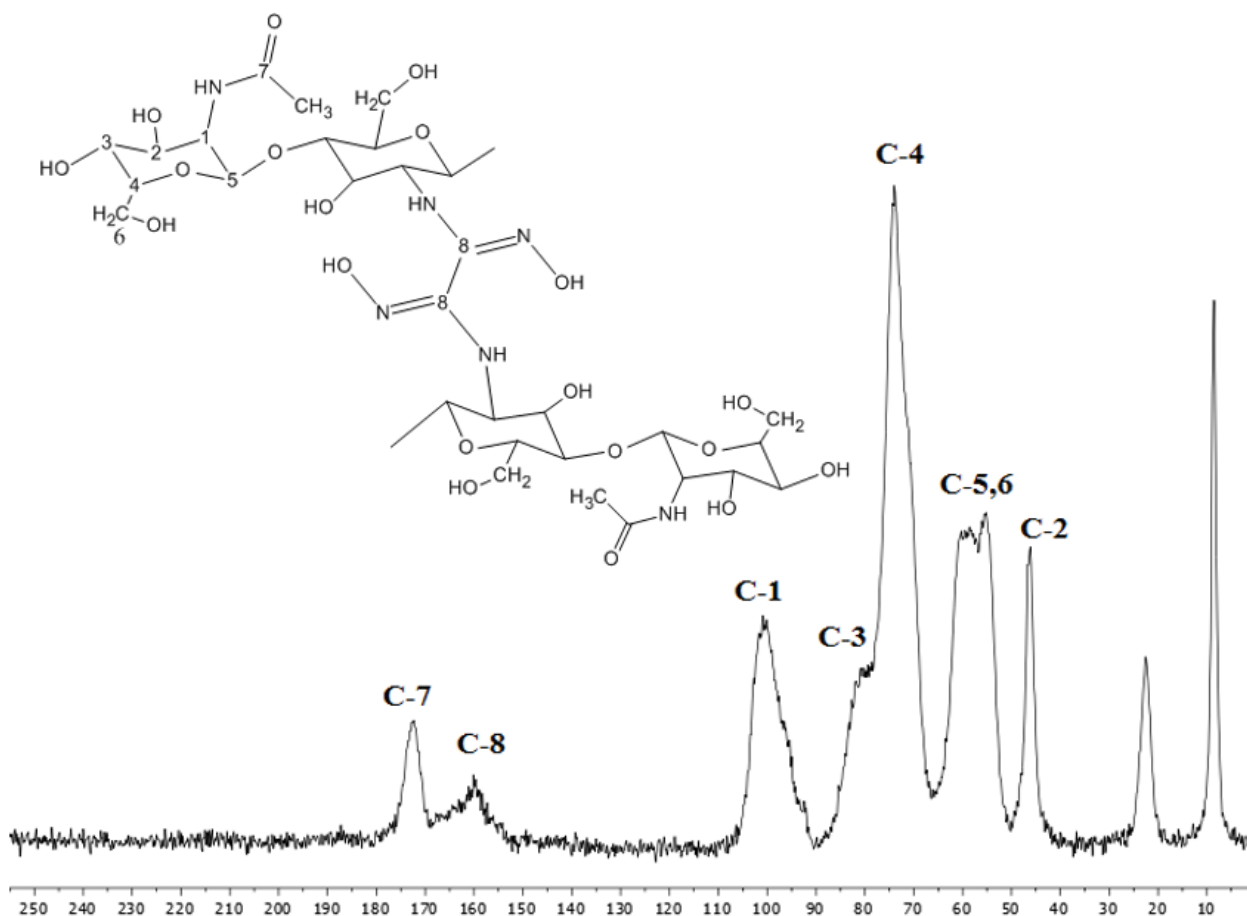


Figure 5. ¹³C CP-MAS NMR Spectrum of CSL

TGA analysis

The thermal property of the CSL was investigated by TGA techniques under air atmosphere. The TGA curve of CSL was given in Fig. 6. It is well known that chitosan have two mass loss stages as water elimination and the decomposition. These stages were observed at 40–100 °C range and 280–400 °C range, respectively [32]. Therefore, in the thermogram of the CSL a weight loss of about 7-8% in the range of 50-150 °C was observed by means of the loss of water. In addition to the loss of water, CSL also displays other significant weight losses (40.75%) in the region 250-350 °C, attributable to the decomposition of chitosan chains. On the other hand, another weight loss (39.12%) was observed at 450-600 °C range, which attributed to the degradation and interchain crosslink of the chitosan as an exothermic process [33].

When the results of CSL compared with the results of the chitosan in terms of the thermal behaviors; there are many important differences can be observed might be due to the interaction between chitosan and dichloroglyoxime.

As a result, CSL exhibited a better final degradation temperature than chitosan.

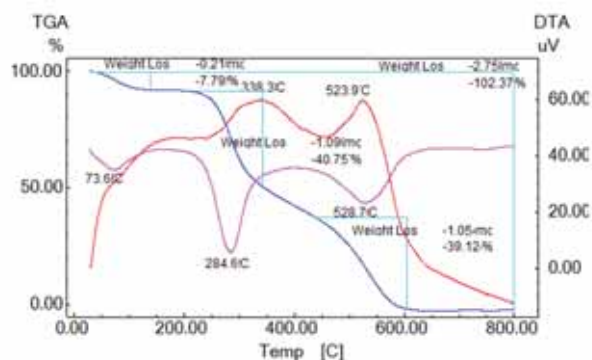


Figure 6. TGA curves of CSL

Metal Ion Uptake Results

Metal retention capacity of CSL (mg/g) was calculated by the following equation.

$$C = Wa/Wp \quad (2)$$

Where C is the metal holding capacity in mg/g, the amount of metal retained as Wa (mg), and Wp is the mass of the derivative in grams.

The results of metal ion uptake studies were given in mg/g for metal ion bound on the CSL. CSL exhibit higher uptake capacity for Cu(II) ion (94.8 mg/g) than the other metal ions used in the study. The capacities for the other metal ions were found as Ni(II) (39.00 mg/g), Fe(II) (78.00 mg/g), Cd(II) (67.00 mg/g) and Co(II) (42.8 mg/g). Thus, the obtained data showed that the order of the overall uptake capacity of the CSL as Cu(II) > Fe(II) > Cd(II) > Co(II) > Ni(II). As a result of this study CSL shows selectivity toward Cu(II), Fe(II) and Cd(II) ions.

Swelling Behaviors

Percent Swelling

Swelling % (S %); is calculated by the following equation.

$$S\% = \frac{W_t - W_o}{W_o} \times 100 \quad (3)$$

Where S%, W_t and W_o are percent of swelling, weight at different times and initial weight of the sample, respectively.

At equilibrium, hydrogel has the greatest swelling value.

With the help of the obtained data, swelling kinetics of network polymers can be determined by calculating values such as equilibrium percent swelling, swelling rate, constant initial swelling rate and theoretical equilibrium percent swelling [34].

Percent swelling rate (S%) was calculated according to equation 3. The values of percent swelling of CSL are given in Table 2.

Table 2. The values of percent swelling of CSL at different temperature and pH.

	25°C			37°C		
CSL (S%)	pH 3	pH 7	pH 10	pH 3	pH 7	pH 10
	86.4	99.6	128.3	99.2	101.0	158.8

In chitosan films, as the cross-linker concentration increased, the water retention capacity and the release of active substance from the film decrease [35].

The swelling curves at different temperatures and pH of CSL are given in Fig. 7 and 8.

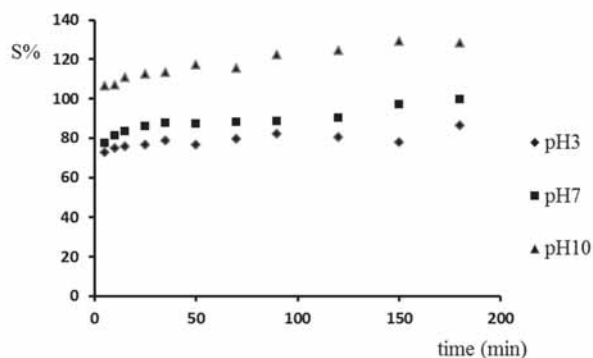


Figure 7. % Swelling values, at 25 °C and different pH values

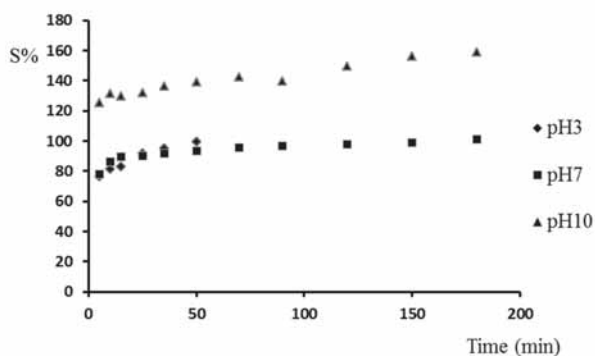


Figure 8. % Swelling values, at 37 °C and different pH values

Equilibrium Water Content (EWC)

Cross-linked polymers, after a certain time after having been exposed to the solvent environment, the rate at which the solvent enters and leaves the structure becomes equal and the balance is reached. At this point, hydrogel has the greatest swelling value.

For hydrogels in equilibrium with solvent, the equilibrium water content is calculated by equation 4. [36]

$$EWC = \frac{W_e - W_o}{W_e} \quad (4)$$

In equation, W_e ; At equilibrium (swollen) polymer mass, W_o ; shows the mass of dry polymer

The equilibrium liquid content is a parameter which is calculated for the hydrogel in this case and is very important for biocompatibility. The EWC values of hydrogel was given in Table 3.

Table 2. The EWC values of CSL.

	25 °C			37 °C		
	pH 3	pH 7	pH 10	pH 3	pH 7	pH 10
CSL	0.46	0.50	0.56	0.50	0.50	0.61

Swelling Kinetics Studies

For calculation swelling of polymers, the following second order kinetics equation can be used [37].

$$\frac{t}{s} = A + Bt \quad (5)$$

Where t is time, S is swelling at t, $B = 1/S_{max}$ is the inverse of the maximum or equilibrium swelling, $A = 1/kS_{max}^2$ is the reciprocal of the initial swelling rate $[(dS/dt)_0]$ of the hydrogel, and kS is swelling rate constant.

The initial swelling rate, the swelling rate constant and the values of theoretical equilibrium swelling of the hydrogel was calculated from the slope and the intersection of the lines, respectively. (see the Supporting Information) (Fig. S9-14) The results are presented in Table 4.

Table 2. The EWC values of CSL.

	25 °C			37 °C		
	pH 3	pH 7	pH 10	pH 3	pH 7	pH 10
CSL						
r_0	35.97	20.87	32.57	36.90	33.90	31.25
S_{max}	83.33	99.01	129.87	104.12	101.01	101.01
$k_s \times 10^3$	5.18	2.13	1.93	3.40	3.32	1.24

CONCLUSIONS

In this work, a crosslinked chitosan derivative (CSL) was synthesized by using chitosan and dichloroglyoxime. The all data support that the chitosan is crosslinked with dichloro glyoxime.

Also, we have investigated swelling behaviors and Cu(II), Ni(II), Co(II), Cd(II), and Fe(II) metal uptake properties of the new derivative.

Highly crosslinked hydrogels have a tighter structure, and swell less than lower crosslinked hydrogels. Crosslinking hinders the mobility of polymer chain, hence lowering the swelling ratio.

It can be said that Chitosan was cross-linked too much when considering the swelling ratios. This is supported by

the DS. Increasing the degree of crosslinking of the system will result in a stronger gel and a higher degree of crosslinking creates a more brittle structure.

EWC value (0.61) of CSL at 37 °C and pH 10 is close to the percent water content values of the body 0.60 (or 60%). Accordingly, CSL exhibits liquid contents similar to living tissues and it can be use as hydrogel.





The CSL metal uptake order is Cu(II) > Fe(II) > Cd(II) > Co(II) > Ni(II). As a result of this study CSL shows selectivity toward Cu(II), Fe(II) and Cd(II) ions.

References

1. Peppas NA, Bures P, Leobandung W, Ichikawa H, Modular Hydrogels for Drug Delivery, *European Journal of Pharmaceutics and Biopharmaceutics* 50 (2000) 27–46.
2. Mogosanu GD, Grumezescu AM, Natural and synthetic polymers for wounds and burns dressing, *International Journal of Pharmaceutics* 463 (2014) 127–136.
3. Jayakumar R, Prabakaran M, Kumar PTS, Nair SV, Tamura H, Biomaterials based on chitin and chitosan in wound dressing applications, *Biotechnology Advances* 29 (2011) 322–337.
4. Boonsongrit Y, Mitrevej A, Mueller BW, Chitosan Drug Binding by Ionic Interaction, *European Journal of Pharmaceutics and Biopharmaceutics* 62 (2006) 267–274.
5. Pillai CKS, Paul W, Sharma CP, Chitin and chitosan polymers: Chemistry, solubility and fiber formation, *Progress in Polymer Science* 34 (2009) 641–678.
6. Jayakumar R, Prabakaran M, Nair SV, Tokura S, Tamura H, Selvmurugan N, Novel carboxymethyl derivatives of chitin and chitosan materials and their biomedical applications, *Progress in Materials Science* 55 (2010) 675–709.
7. Muzzarelli RAA, "Chitin", Pergamon Press, Oxford. 309, 1977.
8. Rinaudo M, Chitin and chitosan: Properties and application, *Progress in Polymer Science* 31 (2006) 603–632.
9. Rodrigues CA, Laranjeira MCM, De-Fávere VT, Stadler E, Interaction of Cu(II) on N-(2-pyridylmethyl) and N-(4-pyridylmethyl) chitosan, *Polymer* 39 (1998) 5121–5126.
10. Wan MW, Kan CC, Rogel BD, Dalida MLP, Adsorption of copper(II) and lead(II) ions from aqueous solution on chitosan-coated sand, *Carbohydrate Polymers* 80 (2010) 891–899.
11. Laftah WA, Hashim S, Ibrahim AN, Polymer hydrogels: A review, *Polymer Plastics Technology and Engineering* 50 (2011) 1475.
12. Rivas BL, Geckeler KE, Synthesis and metal complexation of poly(ethylenimine) and derivatives, *Advances in Polymer Science* 102 (1992) 173–183.
13. Rosso F, Barbarissi A, Barbarissi M, Petillo O, Margarucci S, Calarco A, Peluso G, New polyelectrolyte hydrogels for biomedical applications, *Materials Science and Engineering* 23 (2003) 371–376.
14. Evmenenko G, Alexev V, Budtova T, Buyanov A, Frenkel S, Swelling-induced changes of polyelectrolyte gels, *Polymer* 40 (1999) 2975–2979.

15. Dolbow J, Eliot F, Ji H, Chemically induced swelling of hydrogels. *Journal of the Mechanics and Physics of Solids* 52 (2004) 51-84.
16. Yang Z, Shu J, Zhang L, Wang Y, Preparation and adsorption behavior for metal ions of cyclic polyamine derivative of chitosan, *Journal of Applied Polymer Science* 100 (2006) 3018-3023.
17. Trimukhe KD, Varma AJ, A morphological study of heavy metal complexes of chitosan and crosslinked chitosans by SEM and WAXRD, *Carbohydrate Polymer* 71 (2008) 698-702.
18. Lance KA, Goldsby KA, Busch DH, Effective new cobalt(II) dioxygen carriers derived from dimethylglyoxime by the replacement of the linking protons with difluoroboron(1+), *Inorganic Chemistry* 29 (1990) 4537-4544.
19. Sankararamkrishnan N, Sanghi R, Preparation and characterization of a novel xanthated chitosan, *Carbohydrate Polymers* 66 (2006) 2, 160-167.
20. Sheldrick GM, SHELX 97 Programs for the refinement of Crystal Structures, University of Göttingen: Germany 1997.
21. Taner B, Deveci P, Bereket S Solak AO, Ozcan E, The first example of calix[4]pyrrole functionalized vic-dioximeligand: synthesis, characterization, spectroscopic studies and redox properties of the mononuclear transition metal complexes, *Inorg Chimica Acta* 363 (2010) 4017-4023.
22. Coşkun A, Yılmaz F, Akçemici EG, Synthesis, characterization and electrochemical investigation of a novel vic-dioximeligand and its some transition metal complexes, *Journal of Inclusion Phenomena and Macrocyclic Chemistry* 60 (2008) 393-400.
23. Brugnerotto J, Lizardi J, Goycoolea FM, Arguelles-Monal W, Desbrieres J, Rinaudo M, An infrared investigation in relation with chitin and chitosan characterization, *Polymer* 42 (2001) 3569-3580.
24. Kasaai MR, A review of several reported procedures to determine the degree of N-acetylation for chitin and chitosan using infrared spectroscopy, *Carbohydrate Polymers* 71(2008) 497-508.
25. Baran T, Açiksöz E, Menteş A, Highly efficient, quick and green synthesis of biaryl with chitosan supported catalyst using microwave irradiation in the absence of solvent, *Carbohydrate Polymers* 142 (2016) 189-198.
26. Wang X, Du Y, Fan L, Liu H, Hu Y, Chitosan- metal complexes as antimicrobial agent: synthesis, characterization and Structure-activity study, *Polymer Bulletin* 55 (2005) 105-113.
27. Franca EF, Lins RD, Freitas LCG, Straatsma TP, Characterization of chitin and chitosan molecular structure in aqueous solution, *Journal of Chemical Theory and Computation* 4(12) (2008) 2141-2149.
28. Wan Y, Creber KAM, Peppley B, Bui VT, Ionic conductivity and tensile properties of hydroxyethyl and hydroxypropyl chitosan membranes, *Polymer Physics* 42(8) (2004) 1379-1397.
29. Jothimani B, Sureshkumar S, Venkatachalapathy B, Hydrophobic structural modification of chitosan and its impact on nanoparticle synthesis-A physicochemical study, *Carbohydrate Polymers* 173 (2017) 714-720.
30. Serin S, New vic-dioxime transition metal complexes, *Transition Metal Chemistry* 26(3) (2001) 300-306.
31. Voloshin YZ, Kostromina NN, Roland K, Clathrochelates synthesis, structure and properties, Elsevier, Amsterdam, Netherlands, 2002.
32. Demetgül C, Serin S, Synthesis and Characterization of a New vic-dioxime of Chitosan Derivative and Its Transition Metal Complexes, *Carbohydrate Polymers* 72(3) (2008) 506-512.
33. Sharma AL, Saxena V, Annapoorni S, Malhotra BD, Synthesis and characterization of a copolymer: Poly(aniline-co-fluoroaniline), *Journal of Applied Polymer Science*, 81(6) (2001) 1460-1466.
34. Üzümlü ÖB, Karadağ E, Dye sorption and water uptake properties of crosslinked acrylamide/sodium methacrylate copolymers and semi-interpenetrating polymer networks composed of PEG, *Separation Science and Technology*, 46(2011) 489-499.
35. Duman SS, Şenel S, Kitosan ve Veteriner Alandaki Uygulamaları, *Veteriner Cerrahi Dergisi* 10(3-4) (2004) 62-72.
36. Saraydın D, Karadağ E, Isıkver Y, Sahiner N, Güven O, The influence of preparation methods on the swelling and network properties of acrylamide hydrogels with crosslinkers, *Journal of Macromolecular Science Part; A_ Pure and Applied Chemistry* A41(4) (2004) 421-433.
37. Karadağ E, Saraydın D, Swelling of Superabsorbent Acrylamide/Sodium Acrylate Hydrogels Prepared by Using Multi-Functional Cross-Linkers, *Turkish Journal of Chemistry* 26 (2002) 863-875.

An Investigation of the Effect of Pyrolytic Liquid Obtained From Waste Tire on the Corrosion Behaviours of MgO-C Refractories

Tuba Bahtli¹  Veysel Murat Bostanci²  Derya Yesim Hopa³  Nesibe Sevde Ulvan³  Serife Yalcin Yasti⁴ 

¹ Necmettin Erbakan University, Department of Metallurgical and Materials Engineering, Konya, Turkey

² Afyon Kocatepe University, Department of Chemical Engineering, Afyonkarahisar, Turkey

³ Necmettin Erbakan University, Department of Mechanical Engineering, Konya, Turkey

⁴ Selcuk University, Department of Ceramic, Konya, Turkey

ABSTRACT

In this study, corrosion behaviours of MgO-C refractories by incorporating different binders as phenolic resin and pyrolytic liquid obtained by waste tire pyrolysis were investigated. Moreover, the effect of porosity on the corrosion resistance of those refractories according to types of binders was examined. The microstructures of corroded MgO-C refractories were characterized by Scanning Electron Microscopy (SEM) and Energy Dispersive X-Ray Analyser (EDX). The results showed that K1 refractory produced with only phenolic resin had the lowest amount of porosity (1.37%) and K2 refractory produced by the use of pyrolytic liquid had the highest amount of porosity (5.37%) due to lower binder effect of pyrolytic liquid. According to the results, the refractories produced by the use of pyrolytic liquid had higher porosity and lower corrosion resistance than that of refractories produced by incorporation of phenolic resin as a binder.

Keywords:

Waste tire; Pyrolytic liquid; Binder; MgO-C refractory; Corrosion

INTRODUCTION

Magnesia-carbon (MgO-C) refractories contain about 12–18% total carbon. The primary source of carbon in magnesia-carbon refractories is graphite. Magnesia-carbon (MgO-C) refractory is extensively used in basic furnace and electric arc furnace due to its desirable properties that are obtained by the presence of graphite used as a carbon source. Some of the desirable properties of MgO-C refractories are: high refractoriness, no low melting phase occurs between MgO and C, high melting point, the excellent thermal shock resistance, low thermal expansion, high thermal conductivity, low elasticity, high corrosion resistance by less slag penetration and wettability with a molten metal. However, the spalling and pore generation by the oxidation of graphite caused deteriorations in mechanical and thermal properties of the MgO-C refractories [1-3].

These refractories have excellent corrosion resistance due to the low wettability of carbon by the slag, so the service life of the MgO-C bricks increases. However, after the oxidation of carbon at high temperatures, the slag can penetrate into the structure of magnesia-car-

bon brick because it is destroyed. Therefore, antioxidants such as metals, compounds or alloys are added to prevent oxidation of carbon [4].

Corrosion can be identified as debonding and the destruction of the bond liquid glass together with the chemical dissolution of all phases of the refractory, subsequent physical fragmentation [5].

The vast quantity of waste tires is a serious environmental problem of our age. In the European Union countries, the amount of used tyres was estimated at 3.6 million tonnes in 2013 and about 4 million tonnes of used tyres were generated in the U.S. in 2015. A systematic approach for the recycling and reuse of waste tyres should be handled around the world because they are a source of great potential for valuable chemicals, materials, and fuels [6-7].

Waste tyres are primarily made up of carbon black, natural rubber (NR), and synthetic rubber (SR) [8]. Pyrolysis is a useful method for the recovery of waste tyres to produce three potentially useful products (oil,

Article History:

Received: 2018/03/06

Accepted: 2018/07/09

Online: 2019/01/31

Correspondence to: Tuba Bahtli

Necmettin Erbakan University,
Department of Metallurgical and Materials
Engineering
Tel: 0(332) 325 20 24
E-Mail: taksoy@konya.edu.tr

gas, and char) [9]. The pyrolytic oil can be used directly or added to fuels. The gas has enough energy for the pyrolysis process itself, and the solid product (char) can be used as a solid fuel, carbon black or upgraded to produce activated carbon or other carbon products [10].

Although phenolic resin binder is used in very low amounts, it is a very important ingredient for the refractory body. Due to its sticky structure, it holds raw materials together. Through the curing process which is usually below 300 °C, the binder in the shaped refractory is transformed into a solid state with a macromolecular network structure. In higher temperatures at which refractory is fired, the cured phenolic resin binder is transformed into a rigid carbon skeleton [11]. Waste tyre derived pyrolytic liquid is a complex mixture of aromatic and aliphatic compounds and it can be a carbon source for the refractory body.

In the present study, the effect of pyrolytic liquid obtained by waste tyre pyrolysis on corrosion behaviours of the MgO-C refractories was investigated. The refractory samples were produced by incorporating two different binders as phenolic resin and pyrolytic liquid. The effect of porosity on the corrosion resistance of those refractories according to types of binders was examined. The microstructures of corroded MgO-C refractories were characterized by Scanning Electron Microscopy (SEM- FEI NOVANOSEM 650) and Energy Dispersive X-Ray Analyser (EDX - FEI NOVANOSEM 650).

MATERIAL AND EXPERIMENTAL PROCEDURE

In this study, MgO-C refractories were produced by incorporating flake graphite (10% by weight) into fused MgO. Moreover, phenolic resin and pyrolytic liquid were used as binders. Pyrolytic liquid was produced by pyrolysis of waste tyre whose particle sizes were between about 70 µm and 850 µm, at 500°C with 15°C/min heating rate, and 0,5 litre/min N₂ flow rate. Density, viscosity, pH, and sulphur content values of that liquid were measured as 0.95 g/ml, 45.2 cST, 6.7, and 1.56%, respectively. After pyrolysis, this liquid product was extracted twice by 10% H₂SO₄ acid in order to provide sulphur removal. After this improvement, the density, viscosity, pH, and sulphur values were measured as 0.98 g/ml, 351.4 cST, 5.8, and %1.08, respectively.

Raw materials, antioxidant (metallic Al), novalac (phenolformaldehyde resin), hexamine ((CH₂)₆N₄), and binder solutions (totally 2 wt.%) were mixed, square prism shaped refractories (50 mm×50 mm×50 mm) were produced by applying ~ 100 MPa pressure. Graphite was used as a carbon source in all refractories. Phenolic resin in K1, only pyrolytic liquid in K2, and either phenolic resin or pyrolytic

Table 1. XRF analysis of blast furnace slag

Oxide	(%)
SiO ₂	37.92
CaO	34.90
Al ₂ O ₃	11.75
MgO	7.92
MnO	2.06
Fe ₂ O ₃	1.58
SO ₃	1.20
TiO ₂	0.85
K ₂ O	0.76
BaO	0.38
Na ₂ O	0.33
ZrO ₂	0.06
SrO	0.06
CuO	0.03
P ₂ O ₅	0.02
Loss of ignition	0.18

liquid in K3 were used as binder(s). Then those shaped samples were tempered in Nabertherm N11/R ash furnace at 250 °C for 3 hours with of 5°C/min heating rate.

Three parts were cut and, waited in water about 24 hours in room temperature for each in order to determine the density and open porosity values by Archimedes principles.

In order to determine the interaction of the blast furnace slag with MgO-C composite refractory materials, corrosion tests were performed in two ways according to the ASTM C621-09 standard:

- In the first one, the hole (diameter: ~ 20 mm, depth: ~ 20 mm) was drilled on top of 50 mm×50 mm×50 mm square prism shaped refractories. Then, 4 g (D₁₀₀ < 63 µm) blast furnace slag was put into those holes and, static corrosion tests were performed for 3 hours at 1450 °C under argon atmosphere using 10 °C/min of heating and cooling rates.

Using the SEM-Mapping analysis with backscattered electron images at 1000x magnification, characterization of the microstructures of those corroded samples was performed in the regions including: i) Zone 1 (close to slag) where the blast furnace slag started to penetrate into refractories, ii) Zone 2 that was the middle region between the slag and refractory, and iii) Zone 3 (close to refractory) where the blast furnace slag penetration into refractories was finished. Furthermore, elemental analysis was examined by Energy Dispersive X-Ray Analysis (EDX).

- Secondly, 4 g blast furnace slag was placed at the

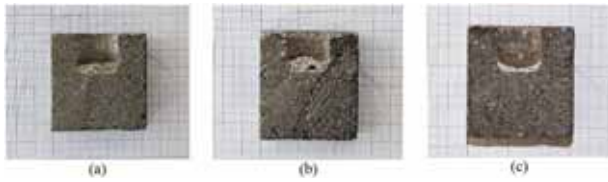


Figure 1. The cross-sectional view of 5cm×5cm×5cm square prism shaped and corroded MgO-C refractories: a) K1, b) K2 and c) K3

centre of the surfaces of refractory materials whose dimensions were 10cm×10cm×2cm (length×width×height) in order to determine the spreading area of slag on the refractory surfaces. Then, the static corrosion tests were conducted at 1450 °C for 3 hours with 10 °C/min heating and cooling rates under argon atmosphere. The measurements of spreading areas were carried out by Image J program [12].

XRF chemical analysis of the blast furnace slag used in this study were given in Table 1.

RESULTS AND DISCUSSION

Images of 5cm×5cm×5cm square prism shaped and corroded MgO-C refractory samples at 1450 °C in argon atmosphere are given in Figure. I. Different binder types were used in MgO-C refractories: only phenolic resin in the K1, only pyrolytic liquid in K2 and either phenolic resin or pyrolytic liquid in K3. Graphite was used as a carbon source in all refractory samples. The light coloured area seen in the cross-sectional view of all refractory materials indicated the slag material (Fig. 1).

The penetration distance of the blast furnace slag into the refractory could not be measured due to the lack of colour contrast in the images (Fig. 1).

Microstructures of those materials were analyzed by the SEM, and also, the corrosion effects were interpreted

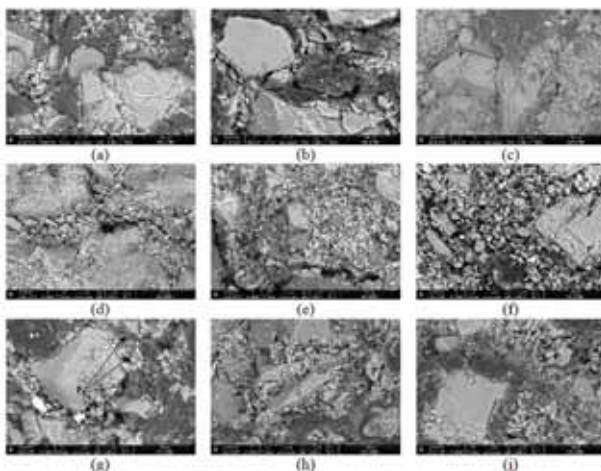


Figure 2. Back scattered electron images of corroded MgO-C refractories (1000×) a)K1-Zone1, b)K1- Zone 2, c)K1- Zone 3, d)K2- Zone 1, e)K2- Zone 2, f)K2- Zone 3, g)K3- Zone 1, h)K3- Zone 2, i)K3- Zone 3, P:Pores

Table 2. SEM/EDX analysis of MgO-C refractories

Composition	Mg	C	O	Ca	Si	Al	Fe
K1 Zone 1	45	25	7	10	6	3	3
K1 Zone 2	51	21	8	8	5	4	3
K1 Zone 3	62	13	9	6	3	5	2
K2 Zone 1	35	13	11	14	21	5	1
K2 Zone 2	43	11	12	13	16	4	1
K2 Zone 3	69	9	11	3	3	4	1
K3 Zone 1	43	23	7	13	9	4	0
K3 Zone 2	50	17	11	9	7	3	2
K3 Zone 3	59	15	9	5	3	7	2

according to EDX analysis, elemental distributions, and microstructural changes (Fig.2).

According to EDX analysis results (Table 2), for K1 refractory material generally the amounts of Ca, Si, and Al were higher in Zone1 than other zones. More amount of carbon and less amount of magnesia in the regions near the slag were observed in K2 than K1. It was thought that magnesite material more and more dissolved in the slag for K2 refractory material and also, it was more affected by the slag due to slag penetration into the porosities. Also, similar to K1, in general, the amounts of Ca, Si, and Al were high in Zone1 according to EDX analysis results (Table 2) for K2 and K3 refractories. Those results confirmed the result of the chemical analysis of the slag (Table 1).

When going to the Zone3, which was close the refractory, from Zone1, which was close to slag, the amount of Mg was generally increased and the amounts of C, Ca and Si were generally decreased for the K1 sample (Figure 2 and Table 2). Ca could be either impurity in MgO or at high amount in the slag. Mg element referred to the periclase phase which was the main matrix of refractories. It was thought that more magnesite grains were dissolved by the influence of the slag than carbon grains, and then the amount of carbon increased in percentage in Zone1. Furthermore, it was seen that the slag concentrated especially on the thin and medium sized MgO grains and affected those grains (Fig. 2a-2c).

In the microstructure images of K1, little amounts of Ca, Si, and Al elements, which were at high amount in the slag, located in regions where the dark gray carbon grains were present. It was also seen that there were more amounts of porosities in the structure due to the dissolution of the magnesite grains into the slag for Zone1 (close to slag) and Zone2 (between refractory and slag) than the Zone3 (close to refractory).

K2 refractory material that was produced by incorporation of pyrolytic liquid as a binder had more porosities and

microcracks because the pyrolytic liquid could not bind the structure as the resin did. Also, Ca and Si elements (indicated with light colour), which were at high amount in slag, were also observed in the graphite regions meaning that refractory was affected by slag more than K1 (Fig. 2d-2f). The slag concentration especially on the thin and medium sized MgO grains and its influence on those grains were observed.

Generally MgO contents decreased whereas slag phase content increased similar to results of the work of Zhang and Lee. Oxidation of carbon and dissolution of MgO in the slag were the main factors for corrosion of MgO-C refractories. [13].

According to SEM microstructure images of K3 after corrosion test (Fig. 2g-2i), either thin or medium sized or bigger sized magnesia grains were affected by slag, and also microcracks were observed. The slag located in porosities and grain boundaries of magnesite and carbon grains in the structure.

When K2 and K3 materials were examined after corrosion test, from Zone1, which was close to slag, to Zone3, which was close the refractory, the amounts of Mg was generally increased, and the amounts of C, Ca, and Si were generally decreased. In this case, when the graphite was used as a carbon source, the slag mainly affected the magnesite grains.

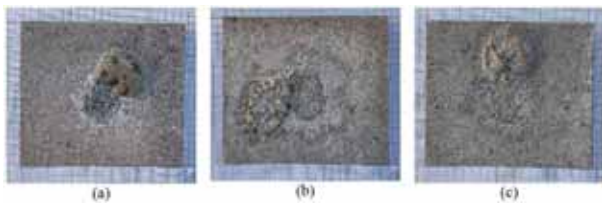


Figure 3. Images of spreading area of slag on the surfaces of 10cm×10cm×2cm (length×width×height) shaped and corroded refractory materials a) K1, b) K2 and c) K3

Images of refractory materials subjected to corrosion tests in argon atmosphere in order to determine the spreading areas of blast furnace slag on refractory surfaces are given in Fig. 3.

In general, the spreading area values of slag on the refractory surfaces decreased as the amount of porosities in the refractory materials decreased (Fig. 3 and Fig. 4). As the decrease of the amount of porosity and the pore size led to the increase of the corrosion resistance, and it was determined that porosity was an important parameter affecting the corrosion resistance. Also, for refractory materials, which were produced by incorporation of phenolic resin as a binder, more dense structure was formed due to better binding property of phenolic resin.

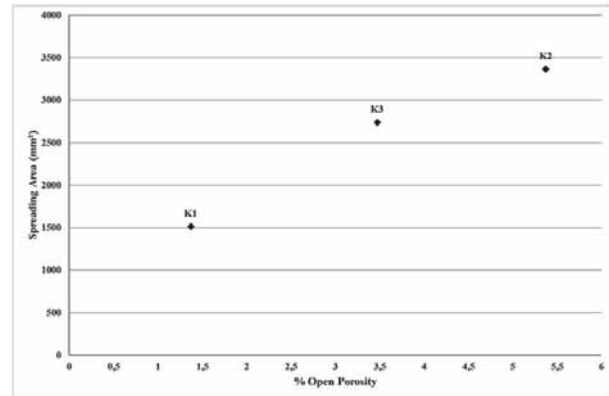


Figure 4. The spreading area of slag on the surfaces of the corroded refractory materials as a function of open porosities

CONCLUSION

When pyrolytic liquid was used in MgO-C refractories as a binder, microcracks and porosities were formed in the structure because of its less binding property than that of resin.

When the spreading areas of slag on the refractory surfaces were examined, it was found that as the amount of porosity in the refractory materials decreased, the spreading area values of the slag on the refractory surfaces decreased, as well.

In the present study, the use of pyrolytic liquid product alone could not show a sufficient effect on corrosion resistance of MgO-C refractories. Therefore, it was suggested to use pyrolytic liquid by mixing it with phenolic resin at different ratios.

ACKNOWLEDGEMENT

This study was supported by TUBITAK under the project no: 115M371.

REFERENCES

1. Mousom B, Sukumar A, Ritwik S. Study on low carbon containing MgO-C refractory: Use of nano carbon. *Ceramics International* 38(3) (2012) 2339-2346.
2. Cho G, Kim E, Li J, Lee J, Jung Y, Byeun Y, Jo C. Improvement of oxidation resistance in graphite for MgO-C refractory through surface modification. *Transactions of Nonferrous Metals Society of China* 24(1) (2014) 119-124.
3. Sadh P.R, Lodha R, Singh K, Singh V. Exfoliated Graphite Fortified MgO-C Refractories. *International Journal for Research in Applied Science & Engineering Technology (IJRASET)* 4 (IX) (2016) 81-89.
4. Gokce A.S, Gurcan C, Ozgen S, Aydin S. The Effect of Antioxidants on the Oxidation Behaviour of Magnesite Carbon Refractory Bricks. *Ceramics International* 34 (2) (2008) 323-330.
5. Aksoy Bahtli T, Aksel C, Kavas T. Corrosion behavior of MgO-MgAl₂O₄-FeAl₂O₄ composite refractory materials. *Journal of Australian Ceramic Society* 53(1) (2017) 33-40.
6. European tyre and rubber manufacturers association (2015) End-of-life Tyre Report (Belgium:Brussels) <http://www.etrma.org/>

- uploads/Modules/Documentsmanger/elt-report-v9a---final.pdf (Accessed 19 December 2017)
7. Rubber manufacturers association (2016) 2015 US scrap tire management summary (WashingtonDC, USA). http://rma.org/sites/default/files/RMA_scrap_tire_summ_2015.pdf (Accessed 21 December 2017)
 8. Maroufi S, Mayyas M, Sahajwalla V. Nano-carbons from waste tyre rubber: An insight into structure and morphology. *Waste Management* 69 (2017) 110-116.
 9. Kordoghli S, Paraschiv M, Tazerout M, Khiari B, Zagrouba F. Novel catalytic systems for waste tires pyrolysis: optimization of gas fraction. *Journal of Energy Resources Technology* 139 (2016).
 10. Williams P.T. Pyrolysis of waste tyres: a review. *Waste Management* 33(8) (2013) 1714-1728.
 11. Zhang J, Mei G, Xie Z, Zhao S. Firing mechanism of oxide-carbon refractories with phenolic resin binder. *Ceramics International* 44 (2018) 5594–5600.
 12. Imagej program. Available: <http://imagej.net> [Date of Access: 21.09.2017]
 13. Zhang S, Lee W.E. Influence of additives on corrosion resistance and corroded microstructures of MgO–C refractories. *Journal of the European Ceramic Society* 21 (2001) 2393-2405.

The Analysis of The Researches on Metal-Semiconductor Structures with and without Interfacial Layer in Turkey

Serhat Orkun Tan 

Karabuk University, Department of Electronics and Automation, Karabuk, Turkey

ABSTRACT

Today, there are fairly large number of theoretical and experimental studies on metal-semiconductor structures or Schottky structures which formed by a tight contact of the metal and semiconductor. Having different physical, chemical and electrical properties many materials have been used to produce metal-semiconductor structures with and without interface layer from past to present. The distinctive properties which are not exist at other diodes, open for improvement and widespread use of electronic technology has led scientists to make studies on the metal-semiconductor structures. Considering the scientific studies on metal-semiconductor structures, the examination of the metal-semiconductor and the metal-semiconductor with interfacial layer structures, the observation of its progress over time and the statistical analysis of academic studies in this area in Turkey have been made in this study. The analysis of the academic studies which are scanned in Web of Science database and made in Turkey were performed with data mining by using automated data collection methods and SQL Server Management Studio program. The statistical analysis results show that the academic studies made for every type of MS structure in Turkey increase for almost every year. Considering the academic studies conducted in 2018, the studies on MS and MPS have reached the highest level in all years with 118 and 13 publications. The last five years rate of the number of publications form nearly %45 of all-time publications and the academic studies made for every type of MS structure in Turkey increase for almost every year.

Keywords:

Metal-Semiconductor; Interfacial Layer; Schottky Structures; Academic studies; Statistical analysis

INTRODUCTION

Metal-semiconductor (MS) or Schottky structures, which form the basis of semiconductor base circuit elements, formed by the tight contact of metal and semiconductors instead of a semiconductor-semiconductor junction as in typical diodes constructed by p-type and n-type semiconductors (PN junction) in contact. In metal-semiconductor structures, typically used metals are gold (Au), silver (Ag), platinum (Pt), tungsten (W), aluminium (Al) and molybdenum (Mo) and semiconductors are gallium arsenide (GaAs), zinc selenide (ZnSe), cadmium telluride (CdTe) besides mostly used Silicon (Si). These structures can respond quickly to the transitions between conductivity and insulator states at high frequencies and become widespread in production and use in the semiconductor industry due to their significant advantages. The voltage drops across PN and Schottky junctions are approximately between 0.6

- 1.7 volts and 0.15 - 0.45 volts, respectively. The typical current - voltage (I-V) curve of Schottky structure and 3D figure of interfacial layered MS structure is given in Fig. 1.

The lower voltage drop of Schottky diode can provide fast switching and also very low switching time. Besides, low power consumption, negligible storage time, rapid response to a change in biases are the other advantages of these structures. These fast switching devices are used in various electronics applications, such as AC to DC (ADC) converters, clamping and clipping circuits, switch mode power supplies, digital computers, mixer and detectors, etc. As a result of this widespread use, many theoretical and experimental researches have been made on MS and interface-layered metal-insulator-semiconductor (MIS) structures [1-4]. Metal-polymer-semiconductors (MPS) and metal-ferroelect-

Article History:

Received: 2018/04/17

Accepted: 2019/02/04

Online: 2019/02/07

Correspondence to: Serhat Orkun Tan

Karabuk University, Department of

Electronics and Automation, Karabuk,

Turkey

Tel: 0(370) 418 7202

Fax: 0(370) 418 7203

E-Mail: serhatorkuntan@karabuk.edu.tr

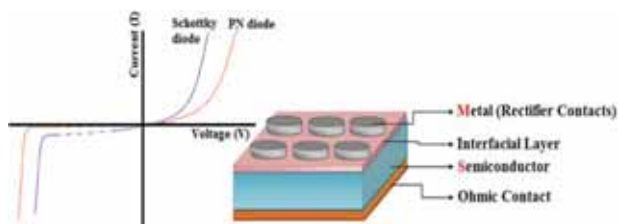


Figure 1. The I-V characteristics of Schottky structure and the structural view of the interfacial layered MS structure.

ric-semiconducting or metal-ferroelectric / insulator-semiconducting (MFS/MFIS) are obtained when a polymer and ferroelectric material is used as an interface layer between the metal and the semiconductor. A thin layer of insulator, polymer, ferro-electric grown by different methods between the metal and the semiconductor isolates the metal from the semiconductor and regulates the load transitions between them. Solid-liquid phase separation, self-assembly, template synthesis and electrospinning are the most used methods to grow the thin interlayer between metal and semiconductor.

The first rectification with MS diodes was performed by Braun in 1874 using metal point contacts on lead sulphide and ferrite sulphide semiconductors [2]. The developed shape of these contacts is Schottky barrier diodes (SBDs) which have a vacuum between the metal and the semiconductor, and the contact potential and the current distribution is homogenous in the junction region. Afterwards, the calculation of the barrier between the metal and the semiconductor has been independently proved by Schottky and Mott [1]. The behaviour of the contacts formed in relation to the character of the MS interface occurs in two forms, Schottky or rectifier contact and ohmic contact. The motion of electrons in the created contacts also determines the contact states. In both MS and MIS type structures, the "rectifier contact" state occurs, if the electron motion in one direction is quite easy at low potential barrier height (forward biases), and it becomes very difficult by increasing potential barrier height (reverse biases) at reverse direction. The ohmic contact states occurs while the electrons can move freely in both directions.

Metal-Insulator-Semiconductor (MIS) structures are obtained by using natural methods or by forming an insulating layer between metal and semiconductor layers by artificial oxidation method. If the thickness of this insulating layer is about 100-200 Å, it is called as MIS structures and above these values it is called as metal oxide semiconductors (MOS) structures or capacitors. Unlike MIS structures, MOS structures usually exhibit capacitor properties due to the thickness of the interface layer. In other words, instead of transmitting loads MOS structures store loads and this means they store huge amount of energy. Generally, compounds such as silicon dioxide (SiO₂) and tin-dioxide (SnO₂) utilize as insulators between metal and semiconductors, isolating metal and semiconductors from each other and

also regulating charge transitions [5-7].

The electrical properties of MPS and MFS / MFIS structures are similar to those of MIS structures in case of the interfacial characteristics between the metal semiconductors, the formation of the insulator / polymer interface layer, the homogeneity at the Schottky barrier height and the series resistance [4]. The quality of the insulating / organic / ferroelectric layer between the semiconductor surface and the metal semiconductors also significantly affects the diode performance. Attention should be paid to the choice of materials with a high dielectric constant, a surface passivation, controlled current conduction mechanism, and the least leakage current as the interface layer [8,9]. The materials with these properties are SiO₂, TiO₂, SnO₂ and Si₃N₄ for insulating materials, and poly-indole, poly-aniline and polyvinyl alcohol (PVA) for organic materials which has been subjected to many studies in chemistry [10-12]. Organic semiconductors have been preferred as interface materials in many recent studies to modify the electrical properties of MS structures [13-16]. The most important reasons for choosing organic semiconductors are high cost, flexible and twistable structure, high loss ratio and high nonlinearity. Beside MS structures, with these important properties organic semiconductors are widely used in electronic and optoelectronic applications such as organic field effect transistors (OFET), organic light emitting diodes (OLED), solar cells, etc., [16].

MFS and MFIS structures have been extensively investigated towards the end of the 1950s in order to acquire field-effect transistors (FETs) by directly growing a variety of ferroelectric materials on Si or by adding a dielectric layer [17-19]. Due to their remarkable physical properties, researches on ferroelectric materials have been increased in the last decade. FeRAM (ferroelectric random-access memories) developed with ferroelectric thin films can store information without needing a stable memory unit [20]. A typical ferroelectric material, bismuth titanite (Bi₄Ti₃O₁₂), is preferred over piezoelectric, optical memories, FeRAMs and electro-optical devices [21,22]. Due to the incompatibility in the formation of MFI structures, which are types of MOS structures, thin insulating layers are added to BTO / Si interfaces by natural or artificial oxidation method to form MFIS structures. It is known that the ferroelectric layer in the MFIS structure gains memory property to the MOS capacitor [23,24].

There are many reasons for researchers to make new researches on MS structures. For instance, it is possible to use a wide range of interlayers and doping materials, such as many metals with different percentages, which are able to increase the conductivity of interlayers. Thanks to this characteristic diversity, it is possible to develop a structure that

emerges to the ideal case and improves its performance. On the other side, new methods can be developed to control the growth and assembly of nanostructures to further improve the development of metal and semiconductor nanostructures. At the same time, in addition to isolated metal or semiconductor nanostructures, they can also be combined with super or hetero structures, resulting in many new features that differ from the characteristics of the main components through interactions such as charge and energy transfer. Considering these significant properties, the area of metal-semiconductor structures is open for improvement and the academic studies on these structures in Turkey are increasing every year. Especially in recent years, many academic studies have been added to the literature on MS, MOS, MPS and MFS / MFIS structures with both MS and interface layers [25-29]. The aim of this study is to examine the MS structures and the statistical distribution of the data obtained from the academic studies on MS structures in Turkey for finding out the increasing rate of the studies, their publication years and the most focusing area of MS structures. Automatic data collection methods were used to obtain data from the Web of Science database and statistical analyses were performed with the SQL server management studio program. The increment of the academic studies on distinct types of MS structures every year indicates the interests of the researchers in Turkey to this area.

MATERIALS AND METHODS

Depending on the data in the Web of Science database, automatic retrieval of information is done by a data retrieval method that uses a data collection program to periodically read the table when any new data is placed. Through the program, each new data search is checked whether predetermined criteria are met. Here, the predetermined criterion is the existence of word sequences which are included in publications at Web of Science database such as "Metal Semiconductor" or "MS Structure", "MIS Structure" OR "Metal Insulator Semiconductor". In addition, if the program meets the criteria, it starts a data retrieval by performing a web-based search based on the data. If the criteria are not met, the program will not perform data retrieval [30]. Data retrieval from the Web of Science database and statistical analysis with the SQL server management studio are done through the logic of the study of Automatic Data Collection Method. The statistical distributions of the studies on the MS structures and the analysis values of the data were transferred to Excel Power Pivot and the analysis results were displayed.

Keywords focused on the study are entered in the Web of Science database as all possible word sequences for MS, interface layered MIS, MPS, MOS and MFS/MFIS structures in order to avoid bypass any publication in this area.

RESULTS AND DISCUSSION

Many electronic circuits and devices use the MS interface as Schottky contacts or as ohmic contacts. MS structures, which have been developed in the past as microwave diodes and radar and radar detectors, are now widely used in many areas, such as solar cells, varactors and switching circuits, metal-semiconductor field effect transistors (MESFETs). The factors that lead the researchers to study on MS structures can be explained as it is an open for improvement area by forming different materials and structures and the expansion of its application field is consistently increasing.

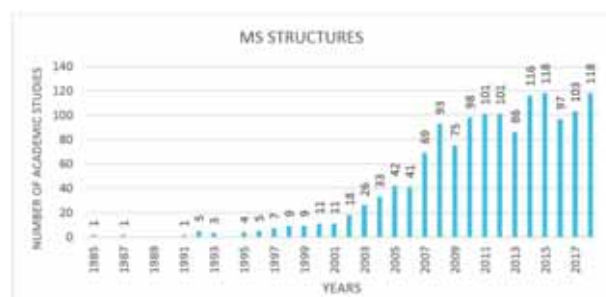


Figure 2. Distribution of the number of Web of Science database indexed academic studies on MS structures in Turkey by years.

Many scientific researches and academic studies have been made in Turkey over the past decade. The distribution of the number of academic studies scanned in Web of Science database on MS structures in Turkey by years is presented in Fig. 2.

Especially in the last decade, the increment rate of the number academic studies on MS structures in Turkey can clearly be seen in Fig. 2. The academic studies on MS structures in Turkey reaches the highest level in 2014 and 2015 and it is expected to increase in the future as well when considering the interest given to this area. It can be predicted that, the increase in the number of researchers and their co-operations and the examinations of different types metal and semiconductor structures due to various parameters, such as temperature, frequency and radiation, are the reasons of this increment between 2014-2015. When an insulating layer is added between the metal semiconductors, MIS structures are formed, and it is known as MPS and MFS / MFIS structures when organic polymers and ferroelectric materials are used as an interface layer. The distribution of the number of Web of Science database indexed academic studies in Turkey on MIS, MPS and MFS/MFIS structures by years is given in Fig. 3.

As clearly seen in Fig. 3, until the last five years there has not been any academic studies made in Turkey on MPS type structures. However, even if a small number of academic studies has been made in this area it was later uncovered that the polymer interface layer enhanced the quality

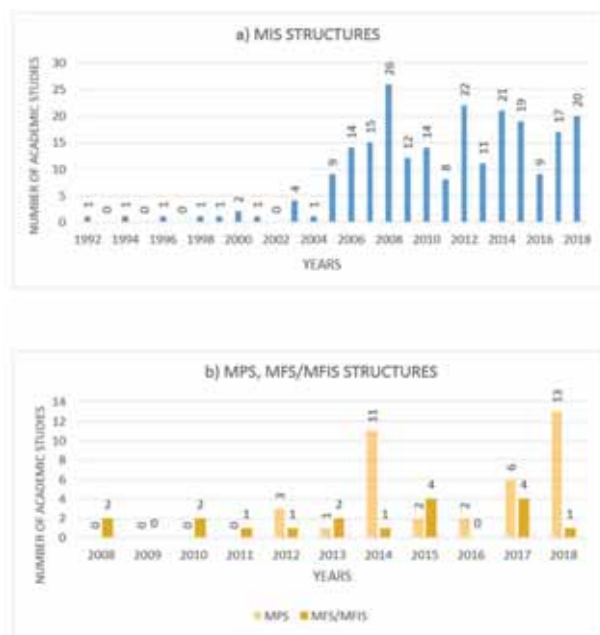


Figure 3. Distribution of the number of Web of Science database indexed academic studies in Turkey on a) MIS b) MPS and MFS/MFIS structures by years.

and performance of the MS structures. The increment of the polymer materials usage at semiconductor technology in recent years indicates that the academic studies on these structures will increase in the following period. On the other hand, although ferroelectric materials are used as interfaces at MS structures earlier than polymer materials, it is observed that ferroelectric materials are less preferred than polymer materials as an interlayer. As mentioned earlier, the addition of an insulator interface layer between the metal and the semiconductors, such as natural or thermal oxidation, forms MIS and MOS type structures. If the thickness of the insulator layer which isolates the metal and semiconductor layers is less than 100 Å, MIS type structure are formed otherwise it will be MOS type structure. The statistical analyses of the academic studies in Turkey scanned at Web of Science database on MOS type structures is presented in Fig. 4.

The number of academic studies made on MOS structures has lagged behind the number of academic studies made on the MIS structures in Turkey. This situation may be explained by the availability of compounds such as silicon dioxide (SiO₂), tin-dioxide (SnO₂) as an interface insu-

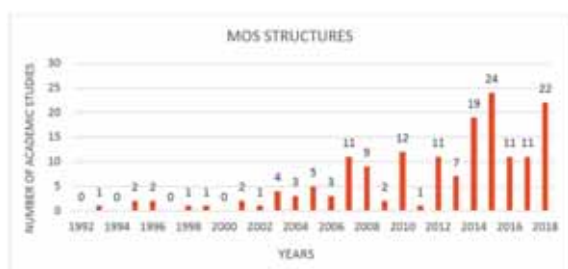


Figure 4. Distribution of academic studies by years on MOS structures and indexed in Web of Science database in Turkey.

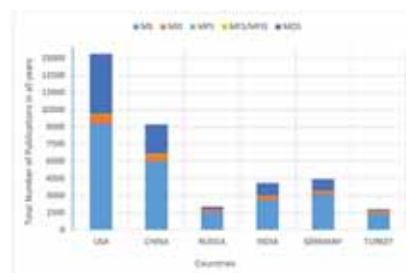


Figure 5. Distribution of the total number of academic studies indexed in Web of Science database in all years on with and without interlayer MS structures by countries.

lating layer and by the fact that diode production capable of fast switching is more preferred than capacitor production. In order to see and compare clearly, the total number of academic studies indexed in Web of Science database for every type of MS structure are presented in Table 1. On the other hand, the number of academic studies on MS structures were comparatively analysed in the world and in Turkey in previous article [31]. According to this research, approximately 5% of the total publications in the world indexed in Web of Science database on MS structures are from Turkey. This rate was 4% for MIS structures, 29.4% for MPS structures, 3% for MFS / MFIS structures and 1% for MOS structures [31]. The rates here indicate that MPS type structures have been considerably attracted in Turkey in recent years. This information is supported by the results which included some leading countries such as USA, China, Russia, India and Germany in addition to Turkey. The total number of academic studies on with and without interlayer MS structures by these leading countries and Turkey are given in Fig.5.

Referring to Fig.5 and Table 1, Turkey seems to be lagging behind in almost all areas except the MPS structures between leading countries of the world. However, when we look at the studies on MS, MIS and MFS / MFIS structures, it is seen that it has almost the same number of studies with the countries except USA and China. The number of publications on the MPS structures in Turkey appears to be greater than the number of total publications in all other leading countries. This shows that MPS structures are attracted too

Table 1. The number of academic studies indexed in Web of Science database on MS and interlayered MS structures in Turkey and some leading countries.

SOME LEADING COUNTRIES ON WITH AND WITHOUT INTERFACIAL LAYER MS STRUCTURES						
TYPES OF MS STRUCTURES	USA	CHINA	RUSSIA	INDIA	GERMANY	TURKEY
MS	9305	6003	1537	2661	3153	1402
MIS	744	530	252	324	242	230
MPS	16	12	1	1	6	38
MFS/MFIS	67	100	6	37	23	18
MOS	5256	2563	255	1094	1026	165

much interest in Turkey. Contrary to this, the studies on the MOS structures in Turkey left behind the other leading countries.

CONCLUSION

In the light of the analysis results, it can obviously be seen that the academic studies on MS structures increased with the years of 2000s and the number of academic studies has increased almost every year. Comparing with the leading countries as USA, China, Russia, India and Germany, the number of publications on MS, MIS and MFS / MFIS in Turkey are very close to the number of publications made in Russia, India and Germany. Meanwhile, in comparison with the academic studies on MS structures in Turkey, the number of academic studies on MIS, MPS and MFS / MFIS structures seem to be considerably less. This can be explained by the adverse effects of the interlayer that reduces the MS structure's quality. Another reason for the smaller number of academic studies on interfacial layered MS structures is the organic polymers usage as an interlayer on MS structures is almost a new area. Although polymers have been used as an interlayer for a few years, it is also a remarkable situation that the number of publications on the MPS structures in Turkey appears to be greater than the numbers of total publications in all other leading countries. Moreover, the increase in the number of academic studies on organic polymers used as interfacial layers in MS structures over the last five years indicates that the studies on MPS structures will increase every year. On the other hand, it is certainly known that, as given for some leading countries, there are also a lot of researches and academic studies on MOS structures around the world. However, in Turkey, the number of academic studies scanned in Web of Science database on MIS structures are more than the academic studies on MOS structures.

REFERENCES

- Sze SM, Kwok KN. *Physics of Semiconductor Devices* 3rd ed., John Wiley & Sons, New Jersey, 2007.
- Rhoderick EH, Williams RH. *Metal Semiconductor Contacts*, 2nd ed., Oxford Press, USA, 1988.
- Farag AAM, Yahia IS, Fadel M. Electrical and photovoltaic characteristics of Au/n-CdS Schottky diode. *International Journal of Hydrogen Energy* 34 (2009) 4906-4913.
- Sharma BL. *Metal-Semiconductor Schottky Barrier Junctions and Their Application*, Plenum Press, New York, 1984.
- Sing A, Reinhard KC, Anderson WA. Temperature dependence of the electrical characteristics of Yb/p-InP tunnel metal-insulator-semiconductor junctions. *Journal of Applied Physics* 68 (1990) 3475-3479.
- Depas MR, Van Meirhaegh L, Laflere WH, Cardon F. Electrical characteristics of Al/SiO₂/n-Si tunnel diodes with an oxide layer grown by rapid thermal oxidation. *Solid State Electronics* 37 (1994) 433-441.
- Goetzberger A, Klausmann E, Schulz MJ. Interface states on semiconductor/insulator surfaces. *CRC Critical Reviews in Solid State Sciences* 6 (1976) 226-233.
- Ichenko VV, Marin VV, Lin SD, Panarn KY, Buyanin AA, Tretyak OV. Room temperature negative differential capacitance in self-assembled quantum dots. *Journal of Physics D: Applied Physics* 41 (2008) 235107.
- Werner J, Guttler H. Barrier inhomogeneities at Schottky contacts. *Journal of Applied Physics*, 69 (1991) 1522-1533.
- Boran F, Akti F. Synthesis and characterization of Poly(HEMA-co-AAc)/Diatomite hydrogel composites: Their application for heavy metal removal from the aqueous solution. *Hittite Journal of Science & Engineering* 2:2 (2015) 173-180.
- Tamahkar E, Özkahraman B. Potential evaluation of PVA-based hydrogels for biomedical applications. *Hittite Journal of Science & Engineering* 2:2 (2015) 165-171.
- Boran F, Akti F. Synthesis of Chitosan-Based Hydrogels as a Novel Drug Release Device for Wound Healing, *Hittite Journal of Science & Engineering* 4:2 (2017) 137-144.
- Aydoğan Ş, İncekara Ü, Türüt A. Determination of contact parameters of Au/Carmine/n-Si Schottky device. *Thin Solid Films* 518 (2010) 7156-7160.
- Gupta RK, Singh RA. Fabrication and characteristics of Schottky diode based on composite organics semiconductor. *Composites and Science and Technology* 65 (2005) 677-681.
- Yahia IS, Farag AA, Yakuphanoglu F, Farooq WA. Temperature dependence of electronic parameters of organic Schottky diode based on fluorescein sodium salt. *Synthetic Metals* 161 (2011) 881-887.
- Çiçek O, Uslu Tecimer H, Tan SO, Tecimer H, Altındal Ş, Uslu İ. Evaluation of electrical and photovoltaic behaviours as comparative of Au/n-GaAs (MS) diodes with and without pure and graphene (Gr)-doped polyvinyl alcohol (PVA) interfacial layer under dark and illuminated conditions. *Composites Part B* 98 (2016) 260-268.
- Fujimori Y, Nakamura T, Kamisawa A. Properties of ferroelectric memory FET using Sr₂(Ta,Nb)2O₇ thin film. *Journal of Applied Physics* 38 (1999) 2285-2288.
- Tokomitsu E, Fujii G, Ishivara H. Nonvolatile ferroelectric-gate field effect transistors using SrBi₂Ta₂O₉/Pt/SrTa₂O₆/SiON/Si structures. *Applied Physics Letter* 75:4 (1999) 575-577.
- Fujisaki Y, Iseki K, Ishiwara H. Long retention performance of a MFIS device achieved by introducing high-k Al₂O₃/Si₃N₄/Si buffer layer. *Material Research Society Symposium Proceedings* 786 (2004) 297.
- Wu D, Li A, Ming N. Characteristics of metal-ferroelectric-insulator-semiconductor structure using La-modified Bi₄Ti₃O₁₂ as the ferroelectric layer. *Microelectronic Engineering* 66 (2003) 773-778.
- Yang Ch-H, Wang Zh, Xu HY, Sun XQ, Han JR. Samarium doped Bi₄Ti₃O₁₂ thin films grown on SiO₂/p-Si (111) by spin coating metalorganic solution decomposition method. *Materials Chemistry and Physics* 88 (2004) 67-70.
- Joshi PC, Krupanidh SB. Structural and electrical studies on rapid thermally processed ferroelectric Bi₄Ti₃O₁₂ thin films by metalloorganic solution deposition. *Journal of Applied Physics* 72:12 (1992) 5817-5819.
- Lea KC, Kim WS, Park H, Jeon H, Pae YH. Thermal-stress stability of yttrium oxide as a buffer layer of metal-ferroelectric-insulator-semiconductor field effect transistor. *Thin Solid Films* 473 (2005) 335-339.
- Hill WAC, Coleman CC. A single-frequency approximation for interface-state density determination. *Solid State Electronics* 23

- (1980) 987-993.
25. Yu J, Wang H, Dong X, Zhou W, Wang Y, Zheng Y, Zhao J. Fabrication and characteristics of Au/PZT/BIT/p-Si ferroelectric memory diode. *Solid-State Electronics* 45 (2001) 411-415.
 26. Dakhel AA. Nanocrystalline Pr-doped ZnO insulator for metal-insulator-Si Schottky diodes. *Journal of Crystal Growth* 311 (2009) 4183-4187.
 27. Tatarođlu A, Altındal Ş. Gamma-ray irradiation effects on the interface states of MIS structures. *Sensors and Actuators A: Physical* 151 (2009) 168-172.
 28. Chen G, Yu J, Lai PT. A study on MIS Schottky diode-based hydrogen sensor using La₂O₃ as gate insulator. *Microelectronics Reliability* 52 (2012) 1660-1664.
 29. Filip LD, Pintilie L, Stancu V, Pintilie I. Simulation of the capacitance-voltage characteristic in the case of epitaxial ferroelectric films with Schottky contacts. *Thin Solid Films* 592 (2015) 200-206.
 30. Tan SO, Türker İ, Toku T. The scientific studies on smart grid in selected European countries. *MATEC Web of Conferences* 112 (2017) 10012.
 31. Tan SO. Schottky Yapılar Üzerine İnceleme ve Analiz Çalışması. *Journal of Polytechnic* 21: 4 (2018) 977-989.

Evaluation of Angiogenic Factor Release from Thermosensitive Poly(N-Vinylcaprolactam)-g-Collagen: In Vitro and In Vivo Studies

Serap Durkut

Ankara University, Tissue Engineering, Biomaterials and Nanobiotechnology Laboratory, Ankara, Turkey

ABSTRACT

In this study, a thermosensitive poly(N-vinylcaprolactam)-g-collagen (PNVCL-g-Col) hybrid hydrogel was synthesized by conjugation using the NHS/EDC cross-linking system, and characterized. At first, the efficiency of in vitro sustained delivery of human vascular endothelial growth factor (VEGF) from the thermosensitive PNVCL-g-Col hydrogel modified with heparin, was evaluated for duration of ten days under in vitro physiological conditions (37°C, pH 7.4). The results indicated that PNVCL-g-Col hydrogel preserved its stability and released ~90% of the loaded VEGF within this time period. In vitro study showed that PNVCL-g-Col was basically histocompatible. Then, the in vivo angiogenic activity of the VEGF-releasing PNVCL-g-Col was investigated using a subcutaneous rat model. In vivo study confirmed that angiogenic-factor-loaded PNVCL-g-Col had the capacity to induce neovascularization indicating that the in vivo bioactivity of the VEGF was preserved in the thermosensitive PNVCL-g-Col.

Keywords:

Thermosensitive polymer; Sustained release; Conjugation; Angiogenesis; Hybrid hydrogel; VEGF.

INTRODUCTION

Intelligent hydrogels which are sensitive to an external stimulus, such as temperature, pH, light, etc. rapidly change their physical structure (size, shape, solubility etc) in response to the stimulus [1-3]. Thermosensitive hydrogels are among the most widely employed intelligent hydrogels. They are characterized by their low critical solution temperature (LCST) [4], and exhibit a distinct and highly reversible temperature-triggered behaviour. Poly (N-vinylcaprolactam) (PNVCL) is a thermosensitive synthetic polymer with a LCST of ~32°C, which is near the range of physiological temperature [5,6]. It is in a swollen state at a temperature below the LCST; however the polymer networks collapse at temperatures above the LCST. Unlike the well-known thermosensitive polymer PNIPAM, hydrolysis of PNVCL does not produce toxic amide compounds making it attractive for biomedical and pharmaceutical applications.

Collagen as a biodegradable and biocompatible natural polymer is the most abundant structural protein in the extracellular matrix (ECM) [7]. Due to its excellent properties, there is great interest in using collagen-based biomaterials for tissue engineering and regenerati-

ve applications. However, one of the problems of using collagen hydrogels is their poor mechanical properties. Collagen can be conjugated with other polymers using carbonyl moiety (-C=O), amine groups (-NH₂/-CONH₂ amide bonds), and hydroxyl groups (-OH) as side groups.

The combination of a thermosensitive synthetic polymer and a natural polymer (such as, collagen, hyaluronic acid, or fibrin) is defined as a hybrid polymer, and may have the potential to produce biomimetic scaffolds with desirable mechanical, biocompatibility, and other properties. Such hybrids could have potential applications in the broad fields of biomedicine [8], biotechnology, and tissue engineering [9].

Fundamental challenges associated with biomimetic scaffolds are lack of a microvascular system which is essential for certain tissues to maintain their viability and function in terms of the transport of nutrients and the signal molecules. Vascular endothelial growth factor (VEGF) is a major regulator of the neovascularization (angiogenesis). Daily injections of angiogenic factors are not suitable due to their short half-lives; thus it is necessary to incorporate the growth factors into hydrogels for

Article History:

Received: 2018/04/29

Accepted: 2019/01/10

Online: 2019/03/28

Correspondence to: Serap Durkut,
Ankara University, Tissue Engineering,
Biomaterials and Nanobiotechnology
Laboratory, 06100, Ankara, Turkey
E-Mail: durkut@science.ankara.edu.tr

their use [10]. Promotion of localized angiogenesis via sustained release of growth factors from hydrogel systems is an attractive field [11].

In this study, a novel thermosensitive PNVCL-g-Col copolymer was synthesized, and evaluated for its potential as a carrier for the sustained release of an angiogenic growth factor. The thermosensitive growth factor release was investigated in terms of the change in the hydrophilic-hydrophobic character, gel-forming and swelling properties of the hybrid biopolymer. The thermosensitive PNVCL-g-Col hydrogel underwent reversible structural transitions from a closed state to an open state with the help of external temperature stimuli, giving on-off switches to modulate growth factor delivery.

MATERIALS AND METHODS

Chemicals

N-Vinylcaprolactam (NVCL), EDC, NHS, and 3-mercaptopropionic acid (MPA) were purchased from Sigma-Aldrich Chemical Co. (St. Louis, MO, USA). 2,2'-Azobisobutyronitrile (AIBN) was supplied from Acros Organics (Thermo Fisher Scientific, Geel, Belgium). All other chemicals and solvents were supplied from either Sigma or Merck (Darmstadt, Germany).

Synthesis of PNVCL with Carboxyl End Group

Thermosensitive PNVCL-COOH was synthesized by radical polymerization in solution [12]. The mixture of monomer NVCL (37.35 mmol), MPA (3.278 mmol) in 50 mL of pure ethanol was added to a sealed flask. The oxygen was removed from the reaction solution through dried nitrogen for 20 min. Then, the initiator AIBN (0.304 mmol) was added to the reaction mixture. Polymerization was performed under nitrogen atmosphere at 75°C for 8 h. Samples were precipitated in diethyl ether. Upon drying in vacuum, the solid was re-suspended in ultrapure water. Then, the solution was dialyzed for 3 days against ultrapure water in cellulose membrane tubing (MW cutoff 1000 Da), followed by lyophilization.

Synthesis of the copolymer

Collagen (isolated from rat-tail tendon; Sigma) solution was prepared in 0.1% acetic acid. Ten milliliter collagen solution (1% w/v) was mixed with aqueous PNVCL-COOH solution. Later, 0.1 mL solution of NHS (0.023 g) and EDC (0.0384 g) in ultrapure water was introduced (PNVCL-COOH/Collagen; 5:1). The reaction was performed under constant stirring for 4 h at room temperature.

Fabrication of PNVCL-g-Col Constructs

In order to obtain PNVCL-g-Col constructs, the PNVCL-g-collagen solution was individually dropped onto the wells of a 24-well cell culture plate (1 mL/well each) and frozen overnight at -80°C. The solidified PNVCL-g-Col was then transferred into a freeze-drying vessel (Alpha1-4 LD Plus, Christ, Osterode am Harz, Germany) under vacuum (<20 Pa) at -60°C temperature and freeze-dried for 24 hours. Finally, PNVCL-g-Col hydrogel constructs were obtained.

ESEM Analysis

Morphology of the lyophilized PNVCL-g-Col construct was analyzed by environmental scanning electron microscopy (ESEM). The samples were coated with a thin layer of gold and analyzed under a (FEI Quanta 200 F FEG) environmental scanning electron microscope.

Angiogenic Factor Loading and in Vitro Release Study

PNVCL-g-Col hydrogel constructs were incorporated with the angiogenic factor, VEGF (from Sigma). Loading of VEGF on PNVCL-g-Col was carried out as follows: 200 µL of heparin (0.5 %) was slowly dropped onto each dry PNVCL-g-Col construct and incubated for 2 hours at 4°C and then 400 ng of VEGF in 200 µL of PBS with 1 mg/mL BSA was added dropwise onto each construct and incubated overnight at 4°C. Heparin was immobilized by the free carboxyl groups of PNVCL-g-Col copolymer, and then VEGF was bound to heparin, since it is a heparin-binding growth factor. All the procedures were conducted under aseptic conditions.

In vitro release of VEGF from thermosensitive PNVCL-g-Col was performed under static conditions. Briefly, the VEGF-loaded PNVCL-g-Col was immersed in 1 mL of 0.1 M PBS (pH 7.2) and incubated at 37°C. The release medium was removed (400 µL) and replaced with fresh buffer at 3, 6, 9, 12 and 24 h, and at days 2, 3, 7, 10, 14 and 21. The amount of released VEGF throughout of the PNVCL-g-Col hydrogel construct (n=3) was quantified by an VEGF enzyme-linked immunosorbent assay (Thermo-Fisher) using a spectrophotometer at 450 nm. The experiments were performed in triplicates.

In Vivo Study

A total of 4 adult male Wistar rats (200-250 grams in weight) were used in this study. The animals were exposed to 12 h of light followed by 12 h of dark, temperature (24°C) and humidity (50%), were supplied with unlimi-

ted drinking water and food on daily basis for 14 days. At implantation, the rats were anaesthetized by Avertin (Sigma), their abdominal regions were shaved, swabbed with 70% isopropanol and then Wescodyn. Using a sterile surgical set-up, the animals were draped and an incision of ca. 3 cm in length was made on the skin and the PNVCL-g-Col constructs (ca. 0.5 g) loaded with 200 μ L of heparin (0.5 %) and 200 μ L of VEGF (200 ng for each construct) were placed in the right and left groin fascia. The skin was sutured after the addition of 0.1 mL sodium cefazolin antibiotic, and closed using 9 mm wound clips (Becton Dickinson, Sparks, MD). The implants were carefully explanted with some of the surrounding tissue after 14 days, fixed, embedded in paraffin, and analyzed by histochemistry.

Statistical Analysis

All quantitative experiments were performed in triplicates. Results were expressed as mean \pm standard deviation, and evaluated with one-way analysis of variance. Statistical significance value was set at $P < 0.05$.

RESULTS AND DISCUSSION

The grafting reaction of the PNVCL-g-Col (Fig. 1(A)) was carried out by amidation of the collagen amine groups with the acid groups of the PNVCL-COOH, using cross-linking agents (EDC/NHS) at room temperature. The PNVCL-g-Collagen hydrogel constructs with approximately 15-mm diameter ($h=5$ mm) were formed using the PNVCL-g-Collagen solution in 24 well culture plates by the lyophilization method, and stored at room temperature until further use (Fig.s 1(B) and 1(C)).

PNVCL-g-Col exhibited a phase transition at around 38°C. The PNVCL-g-Col was transparent below the LCST, and became white and opaque due to a higher temperature than the LCST (Fig. 2).

The higher thermal transition temperature of PNVCL-g-Col copolymer when compared with PNVCL-COOH was attributed to the increase in hydrophilic groups of the collagen. In connection with the new hydrogen bond formation between water molecules and the polar functional groups in the collagen, it is necessary to reach higher temperatures to remove water from the polymer network. The chemical structure and grafting level of the newly-formed copolymer directly influence the LCST of the thermosensitive hydrogel [13]. Other studies with thermosensitive PNIPAAm have shown that the presence of proteins increase the hydrophilicity of the polymer-protein complex [14].

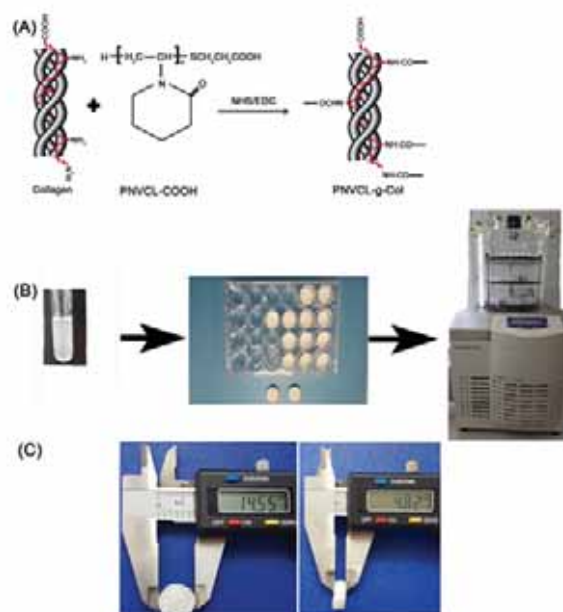


Figure 1. (A) Chemical structure of crosslinked PNVCL-g-Col. (B) Fabrication of PNVCL-g-Col scaffold by lyophilization. (C) The fabricated scaffolds had dimensions of ~ 15 mm in diameter and 5 mm in thickness.

In vitro VEGF Release

PNVCL-g-Col constructs exhibited repeated and reversible swelling-shrinking behavior in aqueous solution depending on environmental temperature. Findings indicate that below the LCST, PNVCL-g-Col copolymer was in a swollen state, while above the LCST an insoluble white-colored form was generated due to the collapse and shrinkage of the PNVCL-g-Col network. Previous studies based on the controlled release of bovine serum albumin and lidocain from PNVCL-g-Col have shown a release behavior in relation to the change in the LCST [15].

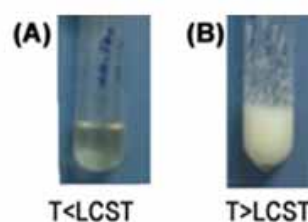


Figure 2. Phase-transition behavior of thermosensitive PNVCL-g-Col: (A) soluble form below LCST. (B) insoluble form above LCST.

The time course of cumulative and daily VEGF release from PNVCL-g-Col hydrogel was investigated at 37°C and the results are presented in Fig.s 3(A) and (B), respectively. According to the in vitro cumulative release results, an initial burst VEGF release was observed at the first 24 hours. The release rate slowed down gradually till the end of 72 hours. A daily in vitro release rate of ~ 1000 -200 pg/ml VEGF was obtained; thus this daily dose was later found to be sufficient to support neovascularization in vivo. From

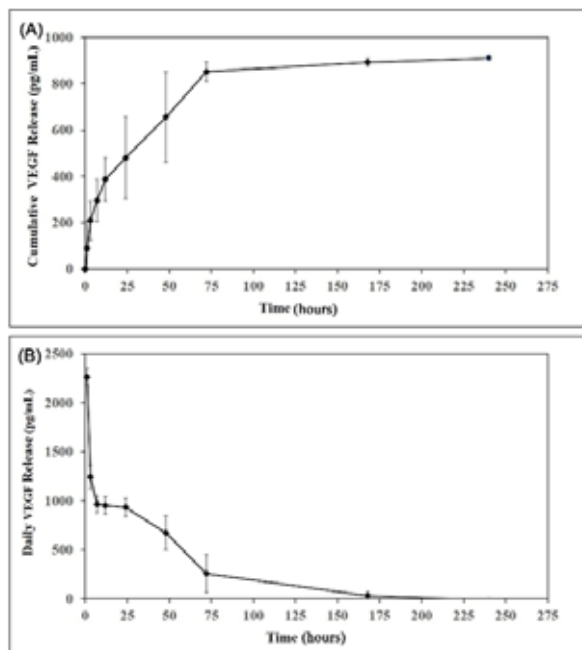


Figure 3. (A) Cumulative in vitro release, and (B) daily in vitro release of VEGF from PNVCL-g-Col.

day 4 to 7, VEGF release had at a slow steady-state phase. After seven days, release of VEGF from PNVCL-g-Col had significantly decreased.

In a study, the VEGF release from a combination of poly(lactide-co-glycolide) (PLGA) microspheres embedded in PLGA matrix was investigated during one month [16]. VEGF release from embedded microspheres was found to be 197 ng/ml which was an initial burst, followed by release at a significantly lower amount (1.1 ng/ml) [16]. In another study, it was reported that VEGF (2.5 and 5.0 μ g) released from activated PLGA sponges displayed a burst like release (~48% first day) profile at the first 3 days (~72%) and observed a relatively slower VEGF release later [17].

We used heparin modification, in order to provide a suitable binding site for the growth factor; as known, VEGF is a heparin-binding growth factor. In another study, hydrogels composed of chemically-modified hyaluronan (HA) and gelatin were used as for the sustained release of human VEGF, in vitro and in vivo [18]. In this particular study, heparin was incorporated similarly with the hydrogel for obtaining a prolonged and greater angiogenic response.

Apparently, the major factor responsible for the decrease in the diffusion of bioactive agents from a hydrogel is its phase transition from the swollen state at low temperatures, to the compact state at high temperatures. The morphology of the collapsed of PNVCL-g-Col shows a reduced pore size, and as a result of this condition free diffusion is prevented leading to the slow release of the growth factors at physiological temperature. VEGF was not completely released from

the PNVCL-g-Col hydrogels after 21 days duration. One possible reason for this could be the presence of interactions between the proteins and the PNVCL-g-Col membranes.

ESEM Analysis

The PNVCL-g-Col demonstrated a distinctly different appearance with physical changes evident even at the macroscopic level, including the color and rigidity depending on temperature. The surface and internal morphology of the PNVCL-g-Col had different microstructure. PNVCL-g-Col constructs had a smoother structure with lesser pores. (Fig. 4). ESEM of the lyophilized PNVCL-g-Col construct exhibited a relatively homogeneous and ordered structure, highly porous and pores connected with each other. Pore structure, size and distribution of the hydrogel constructs are known to influence the equilibrium swelling ratio, the release profile, mobility and mass transfer.

In Vivo Study

The in vivo angiogenic effect of the VEGF-loaded PNVCL-g-Col construct was evaluated in the Wistar rat subcutaneous model for control and experimental treatment cases, including (i) HA-loaded PNVCL-g-Col, and (ii) HA-VEGF loaded PNVCL-g-Col (Fig. 5). In brief, signs of significant inflammation were not observed, and the polymer conjugates were quite well-tolerated by the subjects. Histology showed that the hydrogel was well tolerated and could be defined as histocompatible, as also

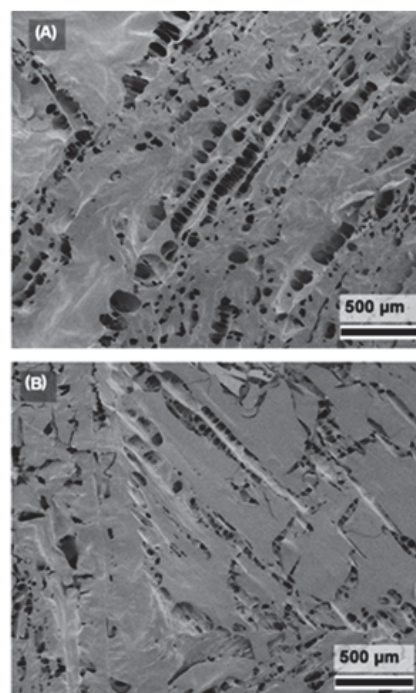


Figure 4. SEM micrographs of freeze-dried PNVCL-g-Col: (A) surface, (B) cross-section (scale bars= 500 μ m).

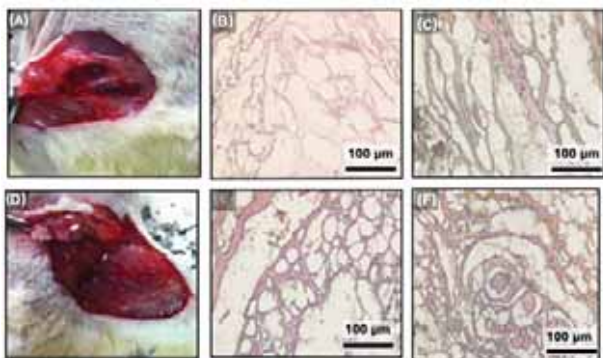


Figure 5. Macroscopic images of VEGF-releasing hydrogel explants 1 weeks (A) and 2 weeks (D) post-implantation. Histochemical findings (H&E-stainings): (B) Col, (C, E) PNVCL-g-Col-VEGF after 7 days, and (F) PNVCL-g-Col-VEGF after 14 days. Scale bars= 100 μ m.

shown previously [15].

H&E stainings indicated that HA-VEGF loaded PNVCL-g-Col scaffold induced in vivo neovascularization. The newly-formed vessels could be observed in the H&E histology sections retrieved at 2 weeks. This findings support that the released VEGF from the PNVCL-g-Col had preserved its angiogenic activity, which is mandatory for neovascularization [19].

CONCLUSION

A thermosensitive PNVCL-g-Col hybrid construct was fabricated by chemical copolymerization, and lyophilization. Incorporation of the angiogenic growth factor VEGF was successfully achieved. The hybrid hydrogel supported in vitro sustained release of VEGF. PNVCL-g-Col exhibited a sustained release depending on temperature. The in vivo angiogenic effect was achieved by the VEGF-releasing thermosensitive hydrogel as well. This hybrid thermosensitive hydrogel may have potential for neovascularization therapies and tissue engineering, in the future.

ACKNOWLEDGMENT

This work was supported by the Ankara University Research Fund (No. 14B0430002). I thank Prof. Y. Murat Elçin and Prof. A. Eser Elçin very warmly for their advice and support.

References

- Hoffman AS. Stimuli-responsive polymers: Biomedical applications and challenges for clinical translation. *Adv. Drug Deliv. Rev.*, 65, 10–16, 2013.

- Qiu Y, Park K. Environment-sensitive hydrogels for drug delivery. *Adv. Drug Deliv. Rev.*, 64, 49–60, 2012.
- Peppas NA, Hilt JZ, Khademhosseini A. Hydrogels in biology and medicine: from molecular principles to bionanotechnology. *Adv Mater*;18:1345–60, 2006.
- Jeong B, Kim SW, Bae YH. Rev. Thermosensitive Sol–Gel Reversible Hydrogels. *Adv. Drug Delivery*, 64 (Supplement), 154–162, 2012.
- Cortez-Lemus NA, Licea-Claverie A. Poly(Nvinylcaprolactam), a comprehensive review on a thermoresponsive polymer becoming popular. *Prog Polym Sci* 53,1, 2016.
- Ferraz CC, Varca GHCC, Ruiz J, Lopes PS, Mathor MB, Lugão AB, Bucio E. Radiation-grafting of thermo- and pH-responsive poly(N-vinylcaprolactam-coacrylic acid) onto silicone rubber and polypropylene films for biomedical purposes, *Radiat. Phys. Chem.* 97, 298–303, 2014.
- Gillette BM, Jensen JA, Tang B. In situ collagen assembly for integrating microfabricated three-dimensional cell-seeded matrices. *Nat. Mater.* 7(8):636–640, 2008.
- Klouda L, Mikos AG. Thermoresponsive hydrogels in biomedical applications. *Eur. J. Pharm. Biopharm.* 68, 34–45, 2008.
- Lee SC, Kwon IK, Park K. Hydrogels for delivery of bioactive agents: A historical perspective. *Adv Drug Deliv Rev*; 65:17–20, 2013.
- Chu H, and Wang Y. Therapeutic angiogenesis: controlled delivery of angiogenic factors. *Ther. Deliv.* 3, 693–714, 2012.
- Gu C, Zheng R, Yang Z, Wen A, Wu H, Zhang H, Yi D. Novel glycidyl methacrylated dextran/ gelatin nanoparticles loaded with basic fibroblast growth factor: Formulation and characteristics. *Drug Dev Ind Pharm*;35: 1419–142, 2009.
- Prabakaran M, Grailer JJ, Steeber DA, Gong S. Stimuli-Responsive Chitosan-graft-Poly(Nvinylcaprolactam) as a Promising Material for Controlled Hydrophobic Drug Delivery. *Macromol. Biosci.*, 8, 843–851, 2008.
- Liu J, Debuigne A, Detrembleur C, Jerome C. Poly(N-vinylcaprolactam): a thermoresponsive macromolecule with promising future in biomedical field. *Adv Healthc Mater.* 3, 1941–68, 2014.
- Wu JY, Liu SQ, Heng PWS, Yang YY. Evaluating proteins release from, and their interactions with, thermosensitive poly (N-isopropylacrylamide) hydrogels. *J Control Release.* 102:361–372, 2005.
- Durkut S, Elçin YM. Synthesis and characterization of thermosensitive poly(N-vinylcaprolactam)-g-collagen. *Artificial Cells, Nanomedicine, and Biotechnology*, 45: 8, 1665-1674, 2017.
- Nortona LW, Tegnella E, Toporek SS, Reichert WM. In vitro characterization of vascular endothelial growth factor and dexamethasone releasing hydrogels for implantable probe coatings. *Biomaterials* 26 3285–3297, 2005.
- Elcin EA and Elcin MY. Localized Angiogenesis Induced by Human Vascular Endothelial Growth Factor-Activated PLGA Sponge. *Tissue Engineering* 12(4):959-6, 2006.
- Pike DB, Cai S, Pomraning KR, Firpo MA, Fisher RJ, Shu XZ, Prestwich GD, Peattie RA. Heparin-regulated release of growth factors in vitro and angiogenic response in vivo to implanted hyaluronan hydrogels containing VEGF and bFGF. *Biomaterials* Volume 27, Issue 30, October, Pages 5242-5251, 2006.
- Peattie RA, Rieke ER, Hewett EM, Fisher RJ, Shu XZ, Prestwich GD. Dual growth factor-induced angiogenesis in vivo using hyaluronan hydrogel implants. *Biomaterials*, 27 (2006), pp. 1868-1875, 2006.

Synthesis and Characterization of Two New Co-Crystals: p-Aminobenzoic Acid with Isonicotinamide and Pyrazine (1:1)

Fureya Elif Ozbek 

Kafkas University, Department of Chemical Engineering, Kars, Turkey

ABSTRACT

Two co-crystals of p-aminobenzoic acid with isonicotinamide and pyrazine were prepared in acetone-ethanol solution by solvent evaporation method in the 1:1 cytochiometric ratio. Their structures were characterized by FT-IR, ¹H NMR and ¹³C NMR spectroscopies, powder X-Ray diffraction and differential scanning calorimetry (DSC) method. Both of the structures have shown the COOH/N heterosynthon. The thermal stability of the co-crystals was investigated by using DSC and it was determined that the melting points of the co-crystals 1 and 2 were lower and in-between from those of their cofomers, respectively.

Keywords:

P-aminobenzoic acid; Isonicotinamide; Pyrazine; Co-crystal

INTRODUCTION

Co-crystals are made up of two or more molecular or ionic compounds combining at a cytochiometric rate, having a different crystallographic pattern than the precursor compounds, and being two or multi-component molecular crystals [1–3]. Molecules forming them are connected to each other by intermolecular interactions such as hydrogen bonds, π - π stacking interactions, C-H... π and Van der Waals forces [4,5]. The most preferred methods used in the preparation of the co-crystals are precipitation, slurry formation, cooling crystallization, grinding, as well as the evaporation that is the most common method. These methods can be applied differently within themselves [6–10]. Co-crystals have been widely used in the field of pharmacology, cosmetics, agriculture, paint, food, optoelectronic and photonic device industries in recent years. A co-crystal usually has some different properties than its constituent compounds, such as resolution, crystallization, melting point, optical properties, biocompatibility and thermodynamic stability [4, 11–14]. In previous studies, two new co-crystals composed of benzoic acid derivatives and pyridine derivatives have been reported. Many different biological activities of these organic ligands and their metal complexes have been investigated, and these complexes have been proven to be more biologically active compounds than free ligands. This phenomenon is not only for metal complexes but

also for the co-crystals [15, 16].

p-Aminobenzoic acid is one of the B group vitamins, having drug property. In addition to vitamin properties, its antiviral, antioxidant, anticoagulant, fibrinolytic, antifungal, sunscreen protective properties are known, and it is used in diagnostic tests of gastrointestinal diseases. p-Aminobenzoic acid, one of the anthranilic acid derivatives, is a compound having a group of amine and a carboxylate groups attached to the benzene ring. These groups that are involved in its structure provide the formation of supramolecular structures by non-covalent interactions with heterocyclic rings which has aromatic ring nitrogen atoms and amide groups [17–19]. The isonicotinamide and pyrazine, which are used as co-formers in the formation of the co-crystals, have aromatic ring nitrogen atom that can form heterosynthon bonds with p-aminobenzoic acid. In addition, isonicotinamide is an antibacterial, antituberculosis compound capable of forming hydrogen bonds with oxygen and nitrogen atoms by means of potential donor atoms in amide group [20–25]. Pharmacological properties of pyrazine and its derivatives are also known. The increase in pharmacological and pharmacokinetic properties of co-crystals, in comparison to its constituent compounds, leads to an enhancement in the potential of its use as a drug. If at least one of the compounds forming the co-crystals is an active pharmaceutical

Article History:

Received: 2018/06/13

Accepted: 2018/10/14

Online: 2019/03/28

Correspondence to: Fureya Elif Ozbek
Kafkas University, Department of Chemical Engineering, Kars, Turkey
Tel: 0(474) 225 1150
Fax: 0(474) 225 1282
E-Mail:fozturkkan36gmail.com

ingredient (API) and the other compound has a pharmacological use, it is regarded as a pharmaceutical crystal [2, 26–28]. In this context, we synthesized two new co-crystals of p-aminobenzoic acid that is an active pharmacological compound (API), with isonicotinamide and pyrazine in the 1:1 cytochiometric ratio, through solvent evaporation method. We examined the structures of these synthesized co-crystals with the method of ^1H NMR, ^{13}C NMR and FT-IR Spectroscopy, Differential Scanning Calorimetry (DSC) and Powder X-Ray Diffraction Analysis (XRPD).

MATERIALS AND INSTRUMENTS

p-Aminobenzoic acid, pyrazine, ethanol and acetone (Sigma Aldrich, Germany) and isonicotinamide (Aldrich, Germany) were purchased commercially available and used as received without purification. IR spectra (from solid samples) were recorded in the range of 600–4000 cm^{-1} with a Perkin Elmer FrontierTM FT-IR Spectrometer using a Diamond ATR accessory. Resolution was set up to 4 cm^{-1} , signal/noise ratio was established by 16 scans. ^1H and ^{13}C NMR spectra were obtained with help of Bruker 400 Mhz spectrometer at ambient temperature using DMSO- d_6 as solvent. Powder X-Ray Analysis were carried out Philips X'Pert Pro diffractometer with Cu, $K\alpha$ radiations, 40 kV of voltage and a current of 35 mA. The samples were analyzed from 5° to 75° (2θ) with 0.2° min^{-1} and a step size of 0.02°. The DSC analyses were carried out a Perkin Elmer Diamond DSC analyzer at heating rates of 10 $^\circ\text{C min}^{-1}$, using a nitrogen atmosphere and a scanning range of 60–400 $^\circ\text{C}$.

Preparation of Co-crystals

To obtain Co-crystal 1, p-aminobenzoic acid (10 mmol, 1.37 g) and isonicotinamide (10 mmol, 1.22 g) were stirring and heating at about 60 $^\circ\text{C}$ for thirty minutes in beakers in acetone:ethanol (1:1) solution. Prepared solution was kept to evaporate for three days and obtained crystals were filtered and washed with acetone:ethanol (1:1) solution.

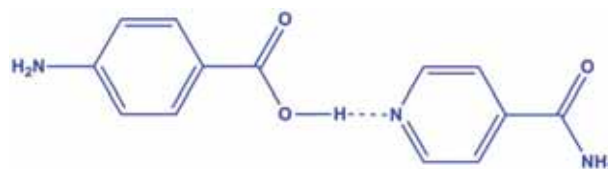


Figure 1. The molecular structure of Co-crystal 1.

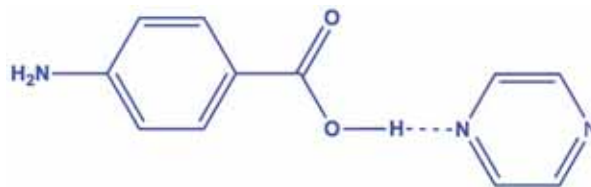


Figure 2. The molecular structure of Co-crystal 2.

To prepare Co-crystal 2, p-aminobenzoic acid (20 mmol 2.74 g) and pyrazine (10 mmol, 0.80 g) were stirring and heating at about 60 $^\circ\text{C}$ for thirty minutes in beakers in acetone:ethanol (1:1) solution. Prepared solution was kept to evaporate for two days and obtained crystals were filtered and washed with acetone:ethanol (1:1) solution.

RESULTS AND DISCUSSION

Evaluation of Structures

The structures of co-crystal 1 and 2 are given in Fig. 1 and 2, respectively. The co-formers are connected by O—H...N hydrogen bonds.

NMR Spectroscopy

4ABA-INA

^1H NMR (400MHz, DMSO- d_6) δ 5.85 (s, 2H, NH₂), 6.61 (d, 2H, ArH; J=8.80 Hz), 7.69 (d, 2H, ArH; J=8.80 Hz), 7.78 (s, 1H, NH), 7.80 (d, 2H, ArH; J=6.00 Hz), 8.30 (s, 1H, NH), 8.71 (d, 2H, ArH; J=6.00 Hz), 12.04 (s, 1H, OH); ^{13}C NMR (100MHz, DMSO- d_6) δ 112.78 (2C), 117.43, 121.44 (2C), 131.30 (2C), 141.34, 150.09 (2C), 153.04 (Ar-C), 166.62, 167.66 (C=O) (Fig. 3).

4ABA-py

^1H NMR (400MHz, DMSO- d_6) δ 5.88 (s, 2H, NH₂), 6.61 (d, 2H, ArH; J=6.00 Hz), 7.70 (d, 2H, ArH; J=8.80 Hz), 8.63

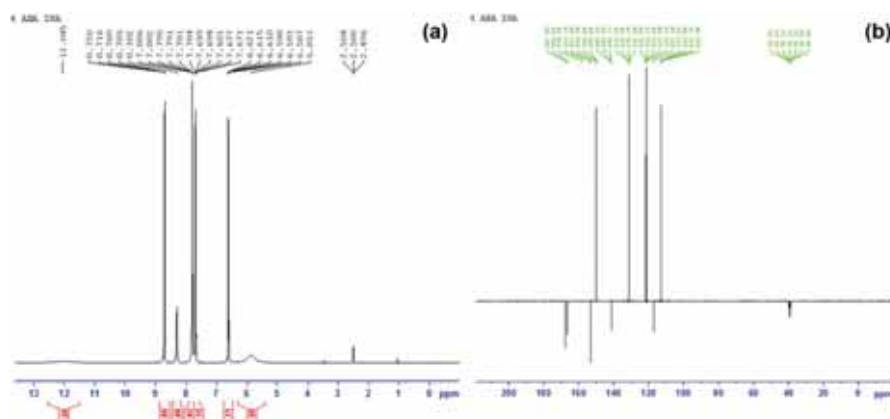


Figure 3. ^1H (a) and ^{13}C NMR (b) NMR Spectra of of Co-crystal 1.

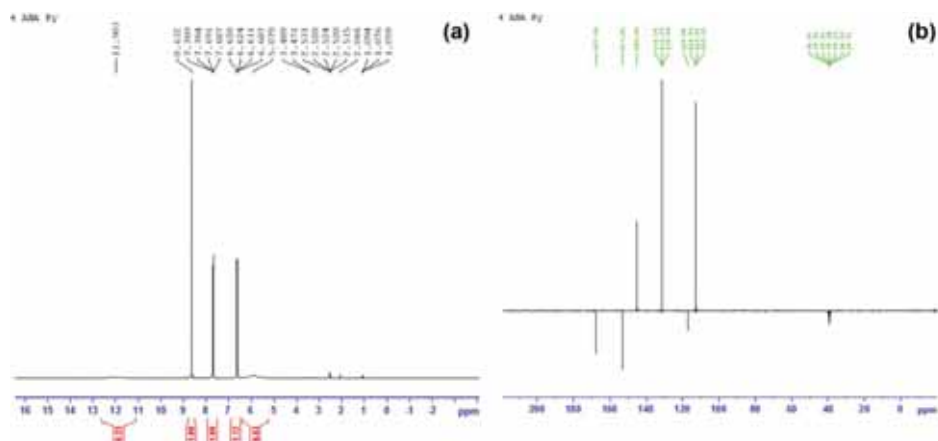


Figure 4. ^1H (a) and ^{13}C NMR (b) Spectra of of Co-crystal 2.

(s, 4H, pirazin-H), 11.98 (s, 1H, OH); ^{13}C NMR (100MHz, DMSO- d_6) δ 112.67 (2C), 117.07, 131.28 (2C), 145.08 (4C), 153.06 (Ar-C), 167.60 (C=O) (Fig. 4).

FT-IR Spectroscopy

The formation of co-crystals 1 and 2 were determined by evaluating the changes in the vibration modes of the functional groups of their co-formers (Fig. 5 and 6). The co-formers of synthesized co-crystals contains an aromatic amine (from the p-aminobenzoic acid) and a heteroamide (from the isonicotinamide) group. The vibration

bands of these are observed at 3363 cm^{-1} and 3227 cm^{-1} ; 3363 cm^{-1} and 3177 cm^{-1} , respectively [29]. In co-crystals, these stretching frequencies cocrystal 1 an co-crystal 2 were appeared at 3355 cm^{-1} and 3177 cm^{-1} ; 3331 cm^{-1} and 3210 cm^{-1} , respectively. The p-aminobenzoic acid and isonicotinamide display to characteristic absorption bands at 1660 cm^{-1} and 1658 cm^{-1} related to carboxyl and carbonyl streches, respectively [29]. These bands were observed at 1688 cm^{-1} and 1651 cm^{-1} in co-crystal's spectra, while in the spectra of co-crystal 2, a single peak related to the carboxyl stretch was observed at 1662 cm^{-1} . The-

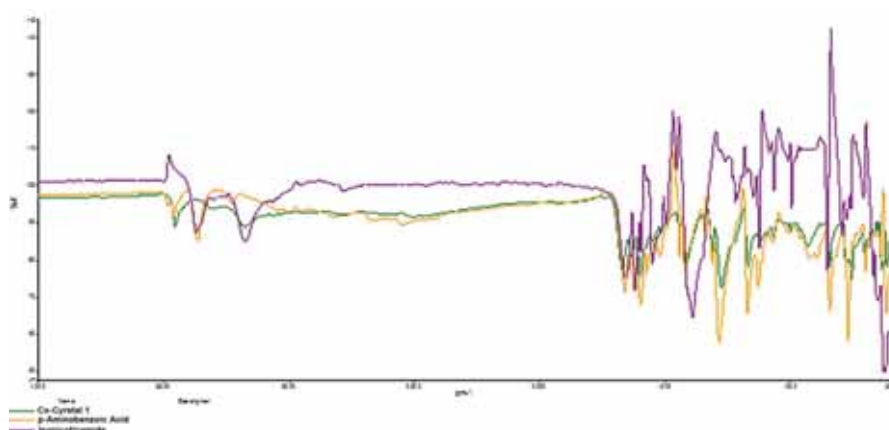


Figure 5. FT-IR Spectra of Co-Crystal 1 and its co-formers.

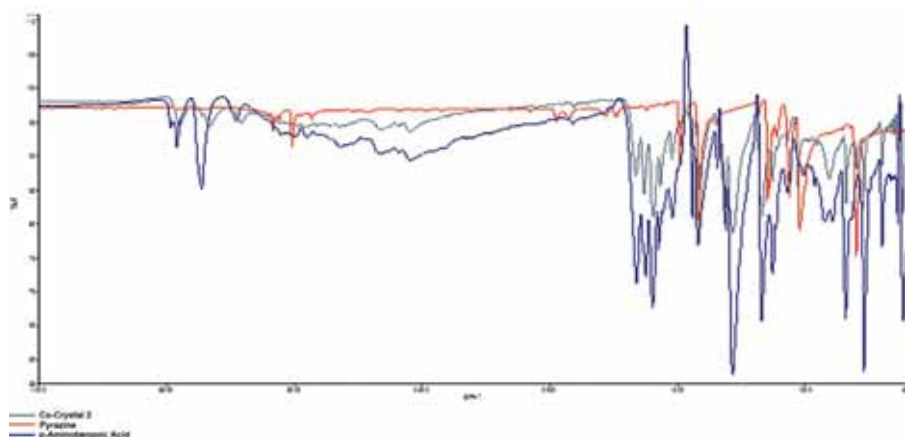


Figure 6. FT-IR Spectra of Co-Crystal 2 and its co-formers.

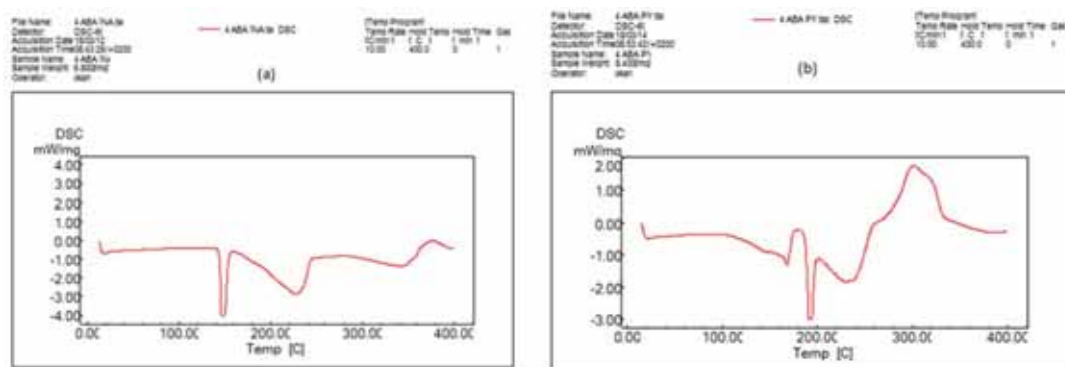


Figure 7. DSC curves of Co-crystal 1 and Co-crystal 2

se vibrational shifts can be attributed to the presence of hydrogen bonds in the co-crystals. C-N stretch and N-H bends were shown at 1410 cm^{-1} and 1310 cm^{-1} (co-crystal 1) and 1411 cm^{-1} and 1315 cm^{-1} (co-crystal 2), respectively.

DIFFERENTIAL SCANNING CALORIMETRY AND POWDER X-RAY DIFFRACTION

Melting points of co-crystals and starting materials were measured with a melting point determination device (Fig. 7 a-b). These values for co-crystal 1, co-crystal 2, p-aminobenzoic acid, isonicotinamide and pyrazine are 145-157 $^{\circ}\text{C}$, 169-170 $^{\circ}\text{C}$, 187-189 $^{\circ}\text{C}$, 155-156 $^{\circ}\text{C}$ and 52-53 $^{\circ}\text{C}$, respectively. DSC analysis were performed to determine the melting points of the co-crystals. According to the results of the DSC analysis, co-crystal 1 is thermally stable up to 143 $^{\circ}\text{C}$. The melting point of crystal 1 is lower (146 $^{\circ}\text{C}$) than the melting points of the starting components p-aminobenzoic acid and isonicotinamide. This proves that the thermal stability of the crystal is less than that of the co-formers. The melting point of co-crystal 2 at 168 $^{\circ}\text{C}$ is higher than the melting point of pyrazine and lower than the melting point of p-aminobenzoic acid. It

can be said that thermal stability is higher than pyrazine and less than p-aminobenzoic acid depending on these values [30,31].

The diffractograms of the co-crystals and their co-formers are shown in Fig. 8-9. Significant differences were observed between the diffractograms of the crystals and the initial substrates. The characteristic diffraction peaks of p-aminobenzoic acid are 9.37, 6.40, 5.79, 4.07 and 2.51 at $2^{\circ}\theta$. For the isonicotinamide, these peaks are 4.99, 4.72, 4.56, 4.26, 3.85, 3.81, 3.44, 3.36 and 2.89 $2^{\circ}\theta$. pyrazine presents diffraction peaks at 4.99, 4.66, 3.54, 3.21, 3.04, 2.75 $2^{\circ}\theta$. Significant differences were observed between the diffractograms of the crystals and the initial substrates. Co-crystal 1 indicates different peaks from p-aminobenzoic acid and isonicotinamide in: 10.99, 7.09, 5.77, 5.12, 4.82, 3.92, 3.53, 3.49, 3.17 and 3.10 $2^{\circ}\theta$. Co-crystal 2 presents different peaks from p-aminobenzoic acid and pyrazine in: 8.87, 6.30, 5.61, 4.43, 3.96, 3.33, 3.22, 2.66 and 2.50 $2^{\circ}\theta$. The diffraction peaks of 5.12, 3.92 and 3.49 $2^{\circ}\theta$ (for co-crystal 1) and 5.61 and 4.43 $2^{\circ}\theta$ (for co-crystal 2) are evidence of the formation of new crystallographic structures.

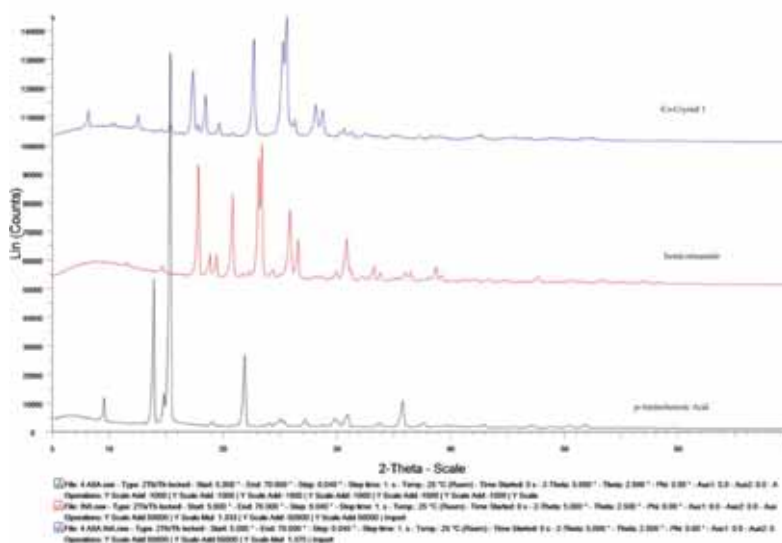


Figure 8. XRD Patterns of Co-crystal 1 and its coformers

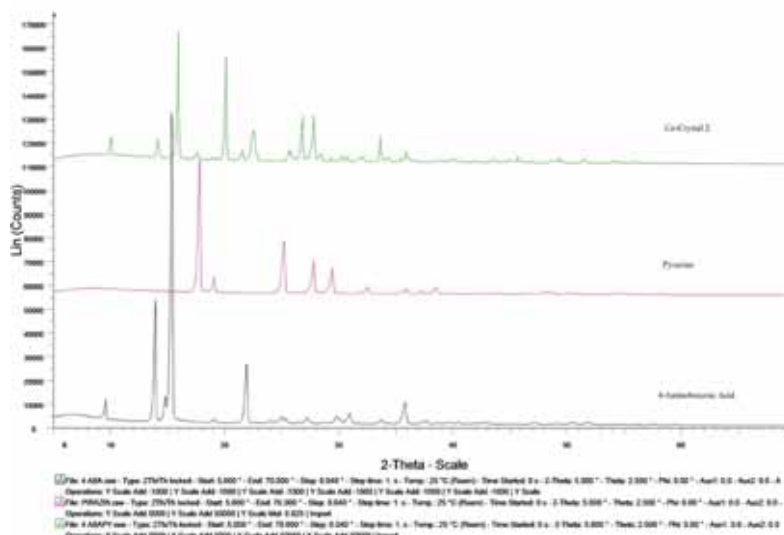


Figure 9. XRD Patterns of Co-crystal 2 and its coformers

CONCLUSION

Co-crystals of 4-aminobenzoic acid with isonicotinamide and pyrazine have been successfully synthesized and characterized by powder X-ray diffraction, FTIR spectroscopy, DSC analysis. The cocrystal 1 and 2 exhibited the carboxylic acid/heterocyclic ring's nitrogen atom heterosynthon. In the synthesized co-crystals, there are hydrogen bonds between the isonicotinamide/pyrazine ring nitrogen atom and the COOH group of the p-aminobenzoic acid. The co-crystals demonstrate same stoichiometry with 1:1 ratio. Because the p-aminobenzoic acid, isonicotinamide and pyrazine which are the coformers of our co-crystals, show pharmacological properties, the synthesized compounds are likely to have pharmacological potential.

ACKNOWLEDGEMENT

The author is thankful to Prof. Dr. Hacali Necefoğlu, Prof. Dr. İmammedin Amiraslanov, Dr. Mustafa Sertçelik, Dr. Murat Beytur and Yusuf Tuncel for valuable contributions.

REFERENCES

- Korotkova EI, Kratochvíl B. Pharmaceutical Cocrystals. *Procedia Chem* 10 (2014) 473-476.
- Gadade DD, Pekamwar SS. Pharmaceutical Cocrystals: Regulatory and Strategic Aspects, Design and Development. *Adv Pharm Bull* 6(4) (2016) 479-494.
- Bond AD. What is a co-crystal? *CrystEngComm* 9(9) (2007) 833-834.
- Stoler E, Warner J. Non-Covalent Derivatives: Cocrystals and Eutectics. *Molecules* 20(8) (2015) 14833-14848.
- Cannon AS, Warner JC. Noncovalent Derivatization: Green Chemistry Applications of Crystal Engineering. *Cryst Growth Des* 2(4) 2002 255-257.
- Hickey MB, Peterson ML, Scoppettuolo LA, Morrisette SL, Vetter A, Guzmán H, et al. Performance comparison of a co-crystal of carbamazepine with marketed product. *Eur J Pharm Biopharm* 67(1) (2007) 112-119.
- Amombo Noa FM, Jacobs A. Phenylacetic acid co-crystals with acridine, caffeine, isonicotinamide and nicotinamide: Crystal structures, thermal analysis, FTIR spectroscopy and Hirshfeld surface analysis. *J Mol Struct* 1139 (2017) 60-66.
- Boyd S, Back K, Chadwick K, Davey RJ, Seaton CC. Solubility Metastable Zone Width Measurement and Crystal Growth of the 1:1 Benzoic Acid/Isonicotinamide Cocrystal in Solutions of Variable Stoichiometry. *J Pharm Sci* 99(9) (2010) 3779-3786.
- Patil SP, Modi SR, Bansal AK. Generation of 1:1 Carbamazepine:Nicotinamide cocrystals by spray drying. *Eur J Pharm Sci* 62 (2014) 251-257.
- McNamara DP, Childs SL, Giordano J, Iarriccio A, Cassidy J, Shet MS, et al. Use of a Glutaric Acid Cocrystal to Improve Oral Bioavailability of a Low Solubility API. *Pharm Res* 23(8) (2006) 1888-1897.
- Yadav A, Shete A, Dabke A, Kulkarni P, Sakhare S. Co-crystals: A novel approach to modify physicochemical properties of active pharmaceutical ingredients. *Indian J Pharm Sci* 71(4) (2009) 359-370.
- Li Z, Huang J, Meng A, Zheng B. Crystal structure, energy band and optical properties of benzoic acid -2-amino-4,6-dimethylpyrimidine (1:1) co-crystals. *J Struct Chem* 51(1) (2010) 53-59.
- Tiekink ERT, Vittal JJ, Zaworotko M (eds.). *Organic crystal engineering: frontiers in crystal engineering*. Wiley: Chichester, U.K, 2010.
- Vijayalakshmi A, Vidyavathy B, Vinitha G. Crystal structure, growth and nonlinear optical studies of isonicotinamide p-nitrophenol: A new organic crystal for optical limiting applications. *J Cryst Growth* 448 (2016) 82-88.
- Sudhakar P, Srivijaya R, Sreekanth BR, Jayanthi PK, Vishweshwar P, Babu MJ, et al. Carboxylic acid-pyridine supramolecular heterocatermer in a co-crystal. *J Mol Struct* 885(1-3) (2008) 45-49.
- Vishweshwar P, Nangia A, Lynch VM. Recurrence of Carboxylic Acid+Pyridine Supramolecular Synthon in the Crystal Structures of Some Pyrazinecarboxylic Acids. *J Org Chem* 67(2) (2002) 556-565.

17. Akberova SI. New Biological Properties of p-Aminobenzoic Acid. *Biol Bull Russ Acad Sci* 29(4) (2002) 390-393.
18. Batool SS, Gilani SR, Tahir MN, Rüffer T. Synthesis, and structural characterization of mixed ligand copper(II) complexes of N,N,N',N'-tetramethylethylenediamine incorporating carboxylates. *J Mol Struct* 1148 (2017) 7-14.
19. Vijayalakshmi A., Vidyavathy B, Vinitha G. Structure and characterization of a new organic crystal for optical limiting applications, isonicotinamide bis-p-aminobenzoic acid. *Ukr J Phys Opt* 17(3) (2016) 98-104.
20. Arıcı M, Yeşilel OZ, Acar E, Dege N. Synthesis, characterization and properties of nicotinamide and isonicotinamide complexes with diverse dicarboxylic acids. *Polyhedron* 127 (2017) 293-301.
21. Ratajczak HM, Bryndal I, Ledoux-Rak I, Barnes AJ. Search for molecular crystals with NLO properties: 3-Nitrophenol with nicotinamide and isonicotinamide. *J Mol Struct* 1047 (2013) 310-316.
22. Bhardwaj RM, Yang H, Florence AJ. Crystal structure of the co-crystal butylparaben-isonicotinamide (1/1). *Acta Crystallogr Sect E Crystallogr Commun* 72(1) (2016) 53-55.
23. Gotoh K, Ishida H. 4-Chloro-2-nitrobenzoic acid-pyrazine (2/1). *Acta Crystallogr Sect E Struct Rep Online* 67(12) (2011) o3222-o3222.
24. Wen G-J, Gu L-S, Sun B-W. Tuning crystal structure and absorption properties of 4-hydroxyisophthalic acid co-crystals using pyrazine derivatives. *J Mol Struct* 1150 (2017) 96-102.
25. Amombo Noa FM, Mehlana G. Co-crystals and salts of vanillic acid and vanillin with amines. *CrystEngComm* 20(7) (2018) 896-905.
26. Steed JW. The role of co-crystals in pharmaceutical design. *Trends Pharmacol Sci* 34(3) (2013) 185-193.
27. Gadade DD, Pekamwar SS, Lahoti SR, Patni SD, Sarode MC. Cocrystallization of Etodolac: Prediction of Cocrystallization, Synthesis, Solid State Characterization And In Vitro Drug Release. *Marmara Pharm J* 21(24530) (2016) 78-88.
28. Jones W, Motherwell WDS, Trask AV. Pharmaceutical Cocrystals: An Emerging Approach to Physical Property Enhancement. *MRS Bull* 31(11) 2006 875-879.
29. Pavia DL, Lampman GM, Kriz GS. Introduction to spectroscopy: a guide for students of organic chemistry. 3. ed. Brooks/Cole: South Melbourne, 2001.
30. Manin AN, Voronin AP, Drozd KV, Manin NG, Bauer-Brandl A, Perlovich GL. Cocrystal screening of hydroxybenzamides with benzoic acid derivatives: A comparative study of thermal and solution-based methods. *Eur J Pharm Sci* 65 (2014) 56-64.
31. Lu E, Rodríguez-Hornedo N, Suryanarayanan R. A rapid thermal method for cocrystal screening. *CrystEngComm* 10(6) (2008) 665-668.

Lightweight design of Rotor Supporting for Large Permanent Magnet Direct Drive Wind Generator

Zhenyu Wu¹, Siming Wang¹  Ling Li²

¹Department of Mechanical Engineering, Hubei University of Technology, 430068, Wuhan, China

²Wuhan Puhui Ocean Optoelectronic Technology Co., Ltd., 430223, Wuhan, China

ABSTRACT

Under the action of electromagnetic force, mechanical force and gravity, the radial deformation of rotor supporting must meet the design standard while ensuring the lightest mass. At first, the mathematical model of single objective optimization is established. Then, the objective function is optimized by the combination of genetic algorithm and finite element method (GA-FEM). With the help of this method, the optimal design parameters of the rotor supporting are obtained. This paper takes the actual rotor supporting of 7MW prototype as the optimization object. The optimal solution of this structure without the lightweight holes can be obtained by first optimization. And then, the optimal solution of the final structure with the lightweight holes is obtained by the second optimization. The final simulation shows that the stiffness can be met while reducing the mass by 40%.

Keywords:

Wind generator; Optimization; Mathematical model; Genetic algorithm; Finite element method

Article History:

Received: 2018/10/12

Accepted: 2018/11/25

Online: 2019/03/28

Correspondence to: Siming Wang,
Department of Mechanical
Engineering, Hubei University of
Technology, Wuhan, China
E-mail: wsm58407818@126.com
Phone: +86 13510785269

INTRODUCTION

Permanent magnet direct drive motor has become the most promising solution for wind generation because of its advantages of high power density, high efficiency, high reliability and low maintenance cost. However, with the increase of the motor power grade, the excessive volume and weight of the motor are obstacles to its manufacture, assembly, transportation and installation [1]. The large permanent magnet direct drive wind generators are large in volume and mass. The main reason is that they not only include effective materials that produce electromagnetic torque, but also include structural materials that transmit torque. In order to overcome the torque load without plastic deformation or fracture, and ensure that the deformation at the air gap of the generator does not exceed the allowable value. The size and mass of structural are greatly increased for its Stiffness and strength requirements.

Rotor supporting is one of the key factors to determine the weight of generator [2]. In the specific construction design stage of wind generator, when it comes to the design of every component, the designers often depend on their experiences, lack theoretical guidance, and often for safety reasons to choose some structural dimensions. Therefore, the design is conservative. This

design method based on subjective experience directly leads to the increase of rotor supporting. Aiming at the optimization of rotor supporting of 7MW prototype. Firstly, the optimization model is established in this paper. The minimum mass of the rotor supporting is selected as the optimization objective. And the deformation of the rotor yoke satisfying the design standard is taken as the constraint condition, when the rotor supporting is under the action of electromagnetic force, mechanical force and gravity. Then, the finite element model is parameterized and the analytical solution is transformed into numerical solution. At last, the optimal solution is obtained through the data exchange between the genetic algorithm and finite element method. This method also provides reference for the optimization design of other large structures in large permanent magnet direct drive wind generator.

STRUCTURE OF 7MW PMDD GENERATOR

The rotor supporting of the 7MW prototype is a large structure which is used to install electromagnetic materials. In addition to ensure that materials should have sufficient strength to overcome the effect of torque load without plastic deformation or fracture.

The rotor supporting should have enough stiffness to ensure that the deformation amount of the Generator air gap does not exceed a certain value. The rotor supporting adapts disc structure which is welded to the steel shaft as a whole. There are several lightweight holes in the rotor disc for reducing the weight. And there are stiffeners on the back of the supporting plate for strengthening the support stiffness.

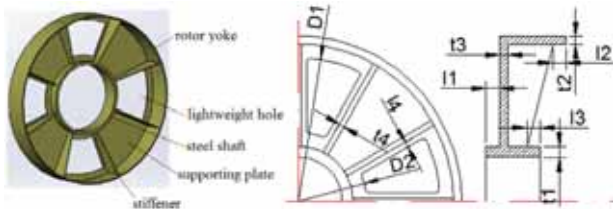


Figure 1. Rotor supporting structure

As shown in Fig. 1. Where:

- D_1 = Outside diameter of the lightweight hole
- D_2 = Inner diameter of the lightweight hole
- l_1 = Distance between the supporting plate and the steel shaft
- l_2 = Upper side length of the stiffener
- l_3 = Lower side length of the stiffener
- l_4 = Distance between the stiffener and the lightweight hole
- t_1 = Thickness of the steel shaft
- t_2 = Thickness of the rotor yoke
- t_3 = Thickness of the supporting plate
- t_4 = Thickness of the stiffener
- n_1 = Number of the stiffener
- n_2 = Number of the lightweight hole

The selection of these parameters directly affects the weight of rotor supporting and mechanical stiffness and strength. Therefore, the purpose of this paper is to determine the most reasonable dimensions of the parameters shown in Figure 1 under the premise of ensuring that the stiffness and strength of the rotor supporting is adequate and the mass is minimum. The rotor supporting determined by this design method can meet the requirements of stiffness and strength under the condition of the lightest weight. Compared with the traditional design method based on experience and conservatism, this method is more scientific and is a lightweight design method for large structural which can be applied in engineering.

OPTIMIZATION PROCEDURE

Optimization model

The least weight of rotor supporting is selected as the optimal objective. And then the radical deformation of the rotor yoke which meet the design criterion is taken

as the constraint condition when the rotor supporting under the action of electromagnetic force, mechanical force and gravity. Radical deformation is usually set to 5% of the gap length. Taking the structural dimension in Fig. 1 as design variables, the optimization mathematical model can be established [3,4]:

$$M_{min} = f(l_1, l_2, l_3, l_4, t_1, t_2, t_3, t_4, D_1, D_2, n_1, n_2) \quad (1)$$

$$\text{s.t. RMS} \leq 5\% \xi$$

Where:

- M_{min} = Mass of the rotor supporting
- RMS = Air gap deformation quantity of the rotor yoke under the action of electromagnetic force and gravity
- ξ = Air gap length, which is equal to 7mm through the electromagnetic scheme.

The value range of each design variable is as follows.

$$0.2835m \leq l_1 \leq 0.347m \quad 0.1395m \leq l_2 \leq 0.171m$$

$$0.0981m \leq l_3 \leq 0.1296m \quad 0.09m \leq l_4 \leq 0.121m$$

$$0.1125m \leq t_1 \leq 0.144m \quad 0.0405m \leq t_2 \leq 0.048m$$

$$0.045m \leq t_3 \leq 0.0605m \quad 0.018m \leq t_4 \leq 0.0215m$$

$$6.025m \leq D_1 \leq 7.3m \quad 3.2m \leq D_2 \leq 3.825m$$

$$n_1 = 6, 8, 10, 12 \quad n_2 = 3, 6$$

Parameterized finite element model

The biggest difference between the study of this paper and the traditional optimal design method is to establish the mathematical model of constraint conditions by using finite element instead of analytical method. The air gap deformation of the rotor yoke is taken as the constraint condition in this paper. If the traditional optimization method is used, the analytical expression of the air gap deformation of the rotor supporting under the action of electromagnetic force, mechanical force and gravity must be established according to the theory of material mechanics and elastic mechanics, which is very difficult for complex geometry. Therefore, the radial deformation of the rotor yoke is calculated by finite element method.

For any optimization problem, it is necessary to find the optimal solution from many groups of feasible solutions. Therefore, the established finite element model is not a finite element model with a set of design variable, but can be modified according to the assignment of design variables which is based on the ANSYS Parametric Design Language (APDL) of the finite element model [5]. The design variable is parameterized. Consequently, the value of the design

variable can be changed by reading the external data file. Therefore, in this paper, the finite element analysis model of rotor supporting parameterization which include modelling, solving and post - processing should be established by using APDL at first. The parameterized finite element analysis flow is as follows.

Step 1: The design variable data file is read.

Step 2: The finite element model is established.

Step 3: Air gap deformation and rotor supporting volume are calculated.

Step 4: The calculation result of the air gap deformation and rotor supporting volume are saved as data file.

Process of GA-FEM

Fig. 2 is used to explain the optimization process of GA-FEM. Genetic algorithm is written in MATLAB language, and finite element calculation is written in APDL [6,9]. The optimization process is as follows.

Step 1: The value range of the design variables are input according to the design requirement.

Step 2: The initial population is generated, and fitness calculations and statistics of it are performed.

Step 3: The new population is generated and decoded through genetic operators such as selection, crossover and mutation. And the fitness calculations and statistics of it are also performed through this method.

Step 4: The individuals of the new and old populations are compared and survival of the fittest.

Step 5: The population periodically update and evolve. If the new population meets the optimization termination condition, the step 6 is executed. Else, the procedure returns to step 3.

Step 6: The optimal scheme is obtained, the iteration optimization is terminated, the parameter optimization is finished, and the optimization results are output.

OPTIMIZATION RESULT

The number and size of the lightweight holes changes with the quantity and rigidity of the stiffener. Therefore, the rotor supporting with no lightweight holes but with stiffeners is optimized first in the process of optimizing the rotor supporting. After determining the optimal rotor supporting with no lightweight holes, based on which, the structure with lightweight holes is optimized. Because the axial direction of the rotor supporting after

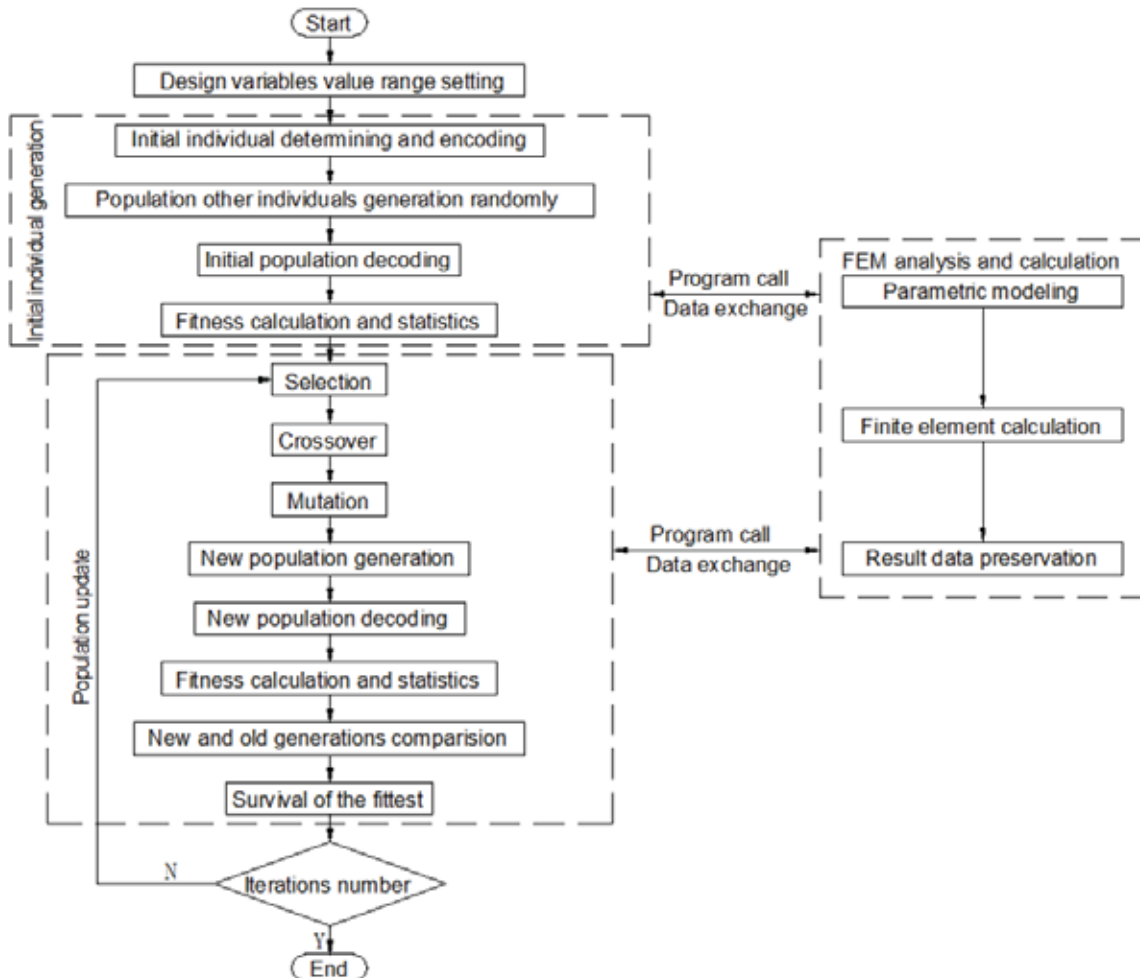


Figure 2. GA-FEM flow chart

installation is parallel to the ground and the structure is nonlinear, the deformation of the rotor supporting is non-uniform under the electromagnetic force, mechanical force and gravity, and the maximum deformation position is changeable according to the structure of the rotor supporting. The deformation of initial structure with no lightweight holes under the action of electromagnetic force, mechanical force and gravity is shown in Fig. 3. The maximum deformation is at the rotor yoke which is 0.101mm, and the allowable deformation is 0.35mm. Therefore, the initial structure can be further optimized.

The rotor supporting is optimized on the bases of initial structure through GA-FEM. And the deformation result of first optimization is shown in Fig. 4. The maximum deformation is 0.132mm which is still less than the allowable value. This indicates that the material of the rotor supporting has not been effectively utilized. So the rotor supporting should be further optimized through machining lightweight holes.

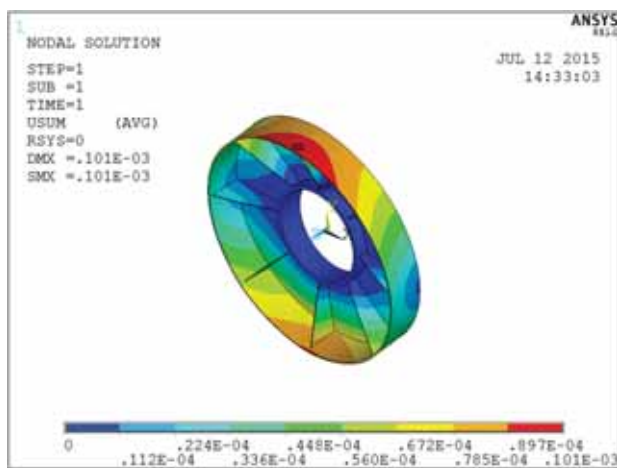


Figure 3. Initial structure deformation

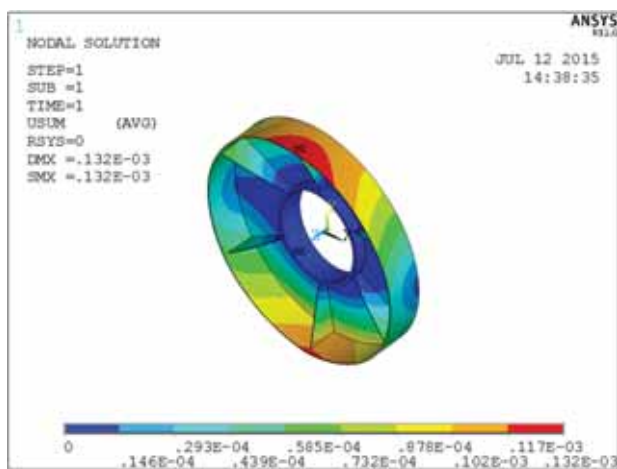


Figure 4. First optimization deformation

As shown in Table 1, the mass of the rotor supporting decreases from 32000kg to 28600kg after first optimization. The evolutionary process of genetic algorithm during first optimization is shown in Fig. 5.

Table 1. Comparison of results before and after optimization

Design variables	Initial structure	First optimization	Maximum
l_1	315mm	343mm	343mm
l_2	155mm	154mm	154mm
l_3	109mm	109mm	109mm
l_4			107mm
t_1	125mm	115m	115mm
t_2	42mm	41mm	41mm
t_3	50mm	45mm	45mm
t_4	20mm	19mm	19mm
D_1			6900mm
D_2			3235mm
n_1	8	6	6
n_2			6
Deformation	0.101mm	0.132mm	0.305mm
Mass	32000kg	28600kg	19000kg

When the population evolves to the 8th generation, the optimization results have become stable, which indicates that the selection of the genetic generation for 10 can meet the requirements of convergence of the optimization results.

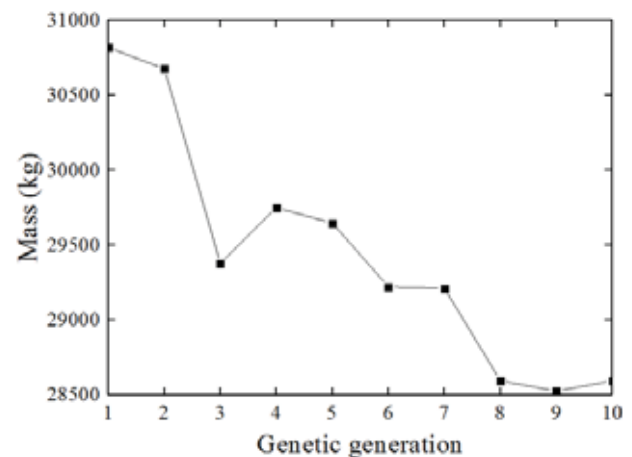


Figure 5. Evolutionary process of first optimization

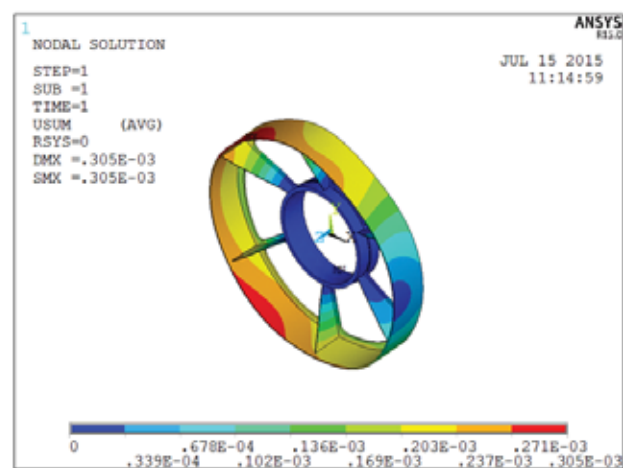


Figure 6. Deformation after second optimization

On the bases of first optimization, the rotor supporting is further optimized to reduce the mass by machining lightweight holes. The number and size of the lightweight holes is optimized during second optimization. The deformation of second optimization is shown in Fig. 6. The maximum deformation value is 0.305mm, which is less than 0.35mm, but very close to the allowable value. Therefore, the design of rotor supporting structure is reasonable. And the mass of the rotor supporting is reduced from 32000kg to 19000kg after two optimization, with the weight loss 40%.

CONCLUSION

The optimization method of combining the genetic algorithm with finite element method which is used to determine the dimension parameters of the structure can be applied to the design of the actual rotor supporting, and it can ensure that the designed rotor supporting satisfies the rigidity and strength with the lightest weight and smallest volume. Because of the more efficient data exchange between the MATLAB and ANSYS, the analysis result is more accurate than the traditional method.

ACKNOWLEDGEMENTS

This work was supported in part by the Hubei Province Natural Science Foundation under Grant 2017CFB324, Science and Technology Supporting Program of Educational Commission of Hubei province under Grant D20171404 and Doctoral Researching Funding under Grant BSQD2015016.

References

1. A.S. McDonald, M.A Mueller, H. Polinder. Structural mass in direct drive permanent magnet electrical generator. *IEE Renewable Power Generation 2* (2008) 3–15.
2. T. M. Jahns. The expanding role of PM machines in direct-drive applications, 2011 International Conference on Electrical Machines and Systems. (2011) 1–8.
3. Wang J, Luo S.M., Su Deyu. Multi-objective optimal design of cycloid speed reducer based on genetic algorithm. *Mechanism and Machine Theory* 102 (2016) 139–148.
4. Wu Z.Y, Qu R.H, Li J., et al., Lightweight Design of Rotor Supporting Structure of Large PM Wind Generator Based on Response Surface Model. 2015 18th International Conference on Electrical Machines and Systems (ICEMS), pp. 705–709, 2015.
5. Gui S.G., Optimal design of product structure based on ANSYS APDL. *Modular Machine Tool & Automatic Manufacturing Technique* 07 (2010) 92–96.
6. Wu Z.Y, Qu R.H, Li J., et al. Structure optimization of rotor supporting of permanent magnet direct drive synchronous generators for large wind turbine based on genetic algorithm and finite element method. 2015 IEEE International Electric Machines & Drives Conference (IEMDC), vol. 2, no. 1, pp. 1755–1760, 2015.
7. N. Taran and M. Ardebili. Efficiency optimization of an axial flux permanent magnet synchronous generator for low speed wind power applications. 2014 22nd Iranian Conference on Electrical Engineering (ICEE), pp. 539–544, 2014.
8. A. Mahmoudi, S. Kahourzade, N.A. Rahim, et al., Design, analysis and prototyping of an axial flux permanent magnet motor based on Genetic Algorithm and Finite-Element Analysis. *IEEE Transactions on Magnetics*, vol. 49, no. 4, pp. 1479–1492, 2013.
9. M.J. Navardi, B. Babaghorbani, A. Ketabi. Efficiency improvement and torque ripple minimization of switched reluctance motor using FEM and seeker optimization algorithm. *Energy Conversion and Management*, 78 (2013) 237–244.

Annual performance simulation of a solar cogeneration plant with sensible heat storage to provide electricity demand for a small community: A transient model

Cagri Kutlu¹  Jing Li^{1,2}  Yuehong Su¹  Yubo Wang³  Gang Pei²  Saffa Riffat¹ 

¹University of Nottingham, Department of Architecture and Built Environment, Nottingham, United Kingdom

²University of Science and Technology of China, Department of Thermal Science and Energy Engineering, Hefei, Anhui, China

³Hubei University of Technology, School of Economics and Management, Wuhan, Hubei, China

ABSTRACT

In this paper, a solar-driven power system as a means of meeting electricity demand in a small community has been investigated in terms of its transient performance on an annual basis. Using a sensible heat storage unit, the heat collected by evacuated flat plate collectors (EFP) can be stored and used at other times to feed an organic Rankine cycle (ORC). The storage unit is analysed using a one-dimensional temperature distribution model including heat loss to the ambient. The stored heat in the unit makes it possible to produce electricity at night. In order to meet the electricity demand in all seasons, evaporation temperature is controlled by the present model via adjusting the water mass flow rate of the heat source. Solar ORC using EFP collectors is a promising technology but dynamic simulation on its annual performance has not been conducted yet. Investigation of the daily performance with consideration of transient behaviour of the components is the main aim of the study. The system performance is evaluated for different seasonal weather conditions. An 8-kW expander output is desired for the peak period which is in the evening for a small community, when sufficient solar irradiance is available. The system also operates in combined heat and power mode during the winter period to supply heat for space heating purpose. Results show that 23296.8 kWh electricity is produced considering the demand pattern during the year and 19344.7 kWh heat can be used for heating for the selected four months.

Keywords:

Solar ORC; Cogeneration; Heat storage; Annual transient simulation.

INTRODUCTION

Nowadays electricity has become the most demanded energy source for household consumers because it has practical conversion ability to other needs in a dwelling. It is not only used for everyday home appliances but is also required for heating, cooling, ventilating systems and in some countries, it is also used for purification of drinking water. However, this electricity demand differs from country to country, month to month and is not same during the day. The results of a study about UK households given in Fig. 1 [1], reveals that electricity demand peaks in December and the lowest demand is noted in May. However, peak demand occurs between 6 -7 pm for all months. Fig.1 gives the results for the UK, though the trend is quite similar for all European countries [2]. It should be noted that this trend may differ according to geographical locations which receive

higher solar irradiance with higher ambient temperatures; the demand will be affected because of air conditioning needs. In Cyprus, for example, winter demand is similar to that of the UK but summer demand is generally flatter with high overnight and day time consumption by the air conditioners [3].

To meet the electricity demand, production using sustainable sources is encouraged by governments and societies. However, there is the need for significantly more development in this field in order to fully satisfy the demand. Photovoltaics have been preferred for years and have an important percentage in future electricity production systems, but generation is intermitted by environmental factors. Moreover, peak demand occurs when there is no, or significantly less residual solar irradiance and residents still demand electricity at night-

Article History:

Received: 2018/10/12

Accepted: 2018/12/05

Online: 2019/03/28

Correspondence to: Cagri Kutlu, University of Nottingham, Department of Architecture and Built Environment, Nottingham, United Kingdom

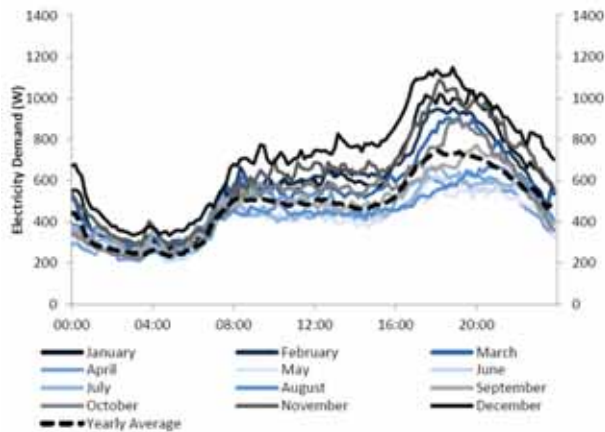


Figure 1. Monthly average electricity demand from the household in UK [1]

time. Therefore, solar ORC systems coupled with heat storage units offer an appropriate sustainable solution to this demand problem.

Since parabolic through collectors (PTC) offer high temperature output, they have been commonly preferred for Solar ORC systems. Chacartegui et al. [4] analyzed an ORC system coupled with a thermal storage unit. They conducted an off-design analysis and observed that the investment cost of direct thermal energy storage systems is lower than indirect storage systems. Li et al. [5] designed and investigated a solar thermal electricity system with water as the heat transfer and storage fluid in thermodynamic and economic considerations. They reported that the direct steam generation system offers both thermodynamic and economic advantages compared to thermal oil used systems. Although PTCs are preferred in solar power plants, these kinds of systems are not easily implemented for domestic use. They require a sun tracking system to use direct beam radiations to concentrate on the receiver. In contrast, evacuated collectors are quite good candidates for heat and power production as they do not need direct beam radiations and

have promising performance under low ambient temperature and radiation conditions in regard to standard flat plate collectors. Freeman et al. [3] used evacuated flat plate collectors and studied a domestic-scale solar combined heat and power system with a thermal storage unit for matching end-user demands. They suggested that using PCM as a heat storage gives a better output for a smaller equivalent storage volume than water. Finally, Kutlu et al. [6] prepared an off-design modelling of a solar ORC system with considering to match user demand during the day. For a given typical day's conditions, they showed that power output can be adjusted by controlling the flow rate of the circulation water and it is possible to meet electricity demand even at night.

Solar ORC using EFP collectors is a promising technology but dynamic simulation on its annual performance has not been conducted yet. According to the literature review, previous studies have used average monthly weather data to analyse the annual performance of systems in general. However, in this study, real daily weather data have been used and simulations have been conducted according to a transient model and considering hourly electricity demand. This study also focuses on controlling the ORC operations related to weather conditions and output requirements such as supporting heat during the winter months.

SYSTEM DESCRIPTION AND METHODOLOGY

The proposed system as given in Fig. 2 consists of three subsystems. The first one is solar field. TVP SOLAR HT-Power EFP collectors are used for heating water which comes from the bottom of the tank, which is then discharged into the top of the water tank. The second subsystem is a sensible thermal storage unit. A water tank is used as a heat storage unit to provide heat for the ORC. Moreover, it facilitates operation of the ORC when solar radiation

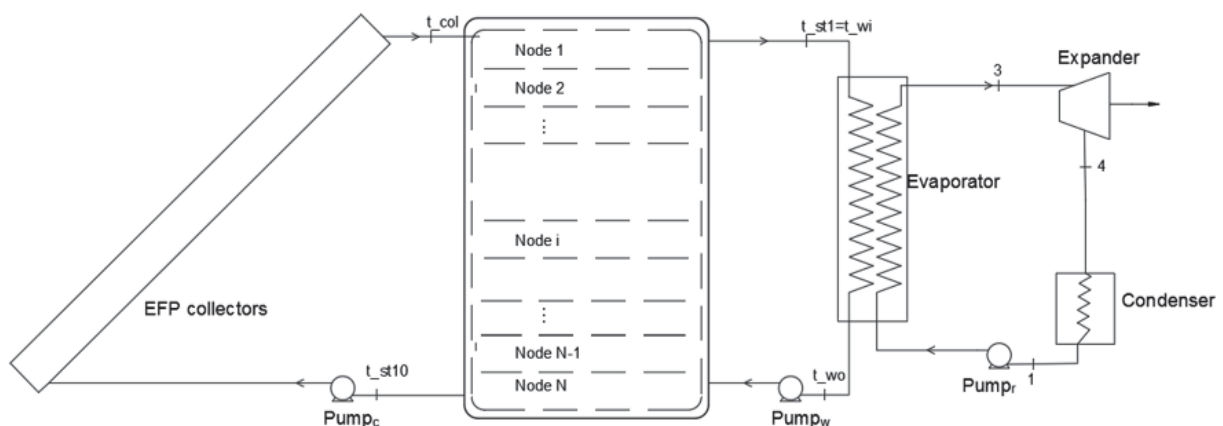


Figure 2. Schematic of the Solar ORC system

is insufficient or unavailable. The last subsystem is the ORC unit. There are four main components in the ORC namely pump, evaporator, expander and condenser.

Regarding mathematical models, the equations for the collectors were adapted from reference [7] and [8]. Thermal efficiency of the collector is given in Eq. (1):

$$\eta_{col} = \eta_0 - c_1 \frac{\bar{T} - T_{am}}{G} - c_2 \frac{(\bar{T} - T_{am})^2}{G} \quad (1)$$

Parameters are taken as $\eta_0 = 0.76$, $c_1 = 0.399$, $c_2 = 0.0067$. Absorbed heat by the collector increases the water temperature, the related equation is given in Eq.(2):

$$\dot{Q}_{col} = \eta_{col} \cdot A_{col} \cdot G = \dot{m}_{cw} \cdot c_{pcw} \cdot (T_{col} - T_{st10}) \quad (2)$$

\dot{Q}_{col} is absorbed heat rate by the collectors, A_{col} is total collector area, G is solar irradiance, T_{col} and T_{st10} are collector outlet and collector inlet temperatures, respectively.

The transient heat storage unit model considers thermal stratification of the water tank. It is analyzed by using multi node tank model which refers one-dimensional temperature distribution model [9]. The cylinder volume has been divided into 10 equal nodes to obtain temperature distribution throughout tank height. Energy balance equation can be written considering the heat loss to the environment in every control volume. Eq. (3) and Eq. (5) show the energy balance equations for the first and last nodes. Eq. (4) shows internal nodes:

$$M_{st1} \cdot c_{pw} \cdot \frac{\partial T_{st1}}{\partial t} = \dot{m}_{cw} \cdot c_{pcw} \cdot (T_{col} - T_{st1}) + \dot{m}_w \cdot c_{pw} \cdot (T_{st2} - T_{st1}) - U_t \cdot A_{st1} \cdot (T_{st1} - T_{am}) \quad (3)$$

$$M_{st,i} \cdot c_{p,w} \cdot \frac{\partial T_{st,i}}{\partial t} = \dot{m}_{cw} \cdot c_{p,cw} \cdot (T_{st,i-1} - T_{st,i}) + \dot{m}_w \cdot c_{p,w} \cdot (T_{st,i+1} - T_{st,i}) - U_t \cdot A_{st,i} \cdot (T_{st,i} - T_{am}) \quad (4)$$

$$M_{stN} \cdot c_{pw} \cdot \frac{\partial T_{stN}}{\partial t} = \dot{m}_{cw} \cdot c_{pcw} \cdot (T_{st(N-1)} - T_{stN}) + \dot{m}_w \cdot c_{pw} \cdot (T_{wo} - T_{stN}) - U_t \cdot A_{stN} \cdot (T_{stN} - T_{am}) \quad (5)$$

\dot{m}_{cw} and \dot{m}_w are mass flow rates of collector and evaporator sides, T_{wo} is the water temperature coming from the evaporator to the tank bottom node. U_t indicates the thermal loss coefficient of the well-insulated tank.

It was decided that a scroll type expander would be used in the analysis as this is particularly well-adapted to small-scale Rankine cycle applications. An empirical model was adapted from [10]. The evaporator is the most important component of the system given that control strategies would be possible by controlling the evaporation temperature in this study. The evaporator is designed according to NTU method. Firstly, evaporator heat transfer area is determined

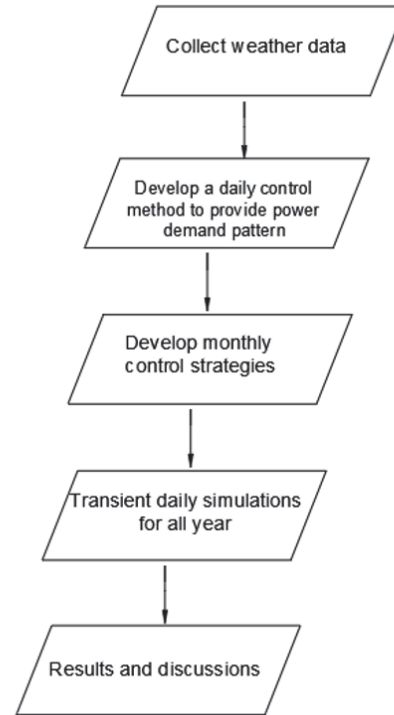


Figure 3. Procedure of the system simulation

after that the analysis is conducted for different operating conditions by using the same evaporator. To find the effectiveness for given conditions, the effectiveness-NTU method is implemented in the analysis. Related equations and detailed investigation about the effects of circulation water mass flow rate on system performance is given in Reference [6].

The paper follows the order given in Fig. 3. EnergyPlus weather data is collected, as it is known that ambient temperature has an influence on condensing temperature and monthly control strategies are developed according to weather conditions. Moreover, daily control strategies are developed considering the demands. Controlled parameters are explained in Section 4. Daily simulations are conducted, results and discussions are presented in Section 5. Finally, the last section introduces the results

WEATHER DATA

The weather data in this paper relates to the climate conditions of Istanbul, Turkey. Relevant parameters such as solar irradiance and ambient temperature profiles are obtained by using the software EnergyPlus [11]. Fig. 4 and Fig. 5 show solar irradiance and environment temperature variations during the year, respectively. Istanbul is chosen for the analysis given that its irradiance profile is similar to some Mediterranean cities in summer but in winter, it is colder than in most other cities around the Mediterranean Basin. As seen in Fig. 4, solar irradiance profile is intermitted during the summer period, which contributes to testing the performance of the system

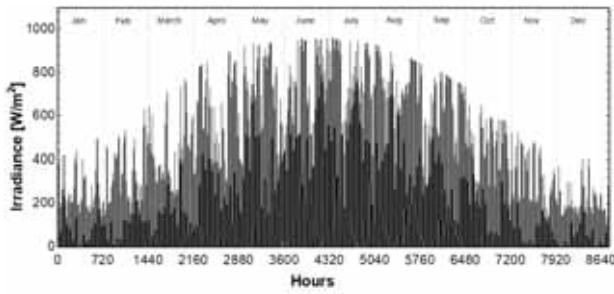


Figure 4. Solar irradiance variation during the year

under variable operating conditions. Moreover, average solar irradiance is quite low in the winter period, being around 200 W/m². The system is not able to produce satisfactory electricity under this irradiance values. Therefore, winter mode (CHP mode) can be activated to produce useful condensing heat for space heating purposes.

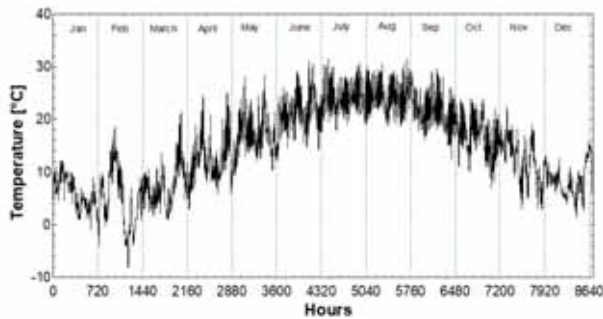


Figure 5. Ambient temperature variation during the year

CONTROL STRATEGIES

The main aim of this paper focuses on application of the control strategies. To maintain the demand profile which is given in Fig. 1, 24hrs of a day is analyzed in three different periods then heat source water circulation mass flow

rate is adjusted for every period. Adjusted mass flow rates contribute to controlling the evaporating temperature, that is to say, controlling the electricity output [6]. Therefore, regarding the expander model, mass flowrate of the refrigerant R245fa is determined by the evaporating temperature. Collector mass flow rate is also adjusted according to weather conditions. In order to reach a higher temperature in the top part of the water tank, collector mass flow rates are reduced in winter months. To maintain similar operation for next days, a stop criterion must be defined. The fifth water element in the tank is chosen as stop consideration; this activates to refrigerant pump is shut off and the tank is switched to static mode until 08:00 the next day. Condensing temperature is dependent upon the ambient temperature except CHP mode.

In CHP mode, the target is to produce electricity only for collector pumps due to weak solar radiation. The condensing temperature is increased, and condensing heat can be used for space heating purposes. A summary of the monthly control strategies is given in Table 1.

SIMULATIONS

The presented system is analyzed for a small community; ten houses are selected, so the total collector area of the system is selected as 550 m² and water storage tank as 88 m³. Heat exchangers are dimensioned according to NTU methods so off-design operation is considered for the whole year. Although the main aim is conducting the yearly simulation considering the transient behaviour, application of the control strategies are necessary for meeting the user electricity demand. The operation follows the given strategy; the collector pump runs, and solar energy is stored in the tank, meanwhile the ORC produ-

Table 1. Summary of the control strategies in monthly basis

Months	\dot{m}_{col} (kg/s)	T_{cond}	Stop Temp.	Water flowrate (kg/s) 08:00-18:00	Water flowrate (kg/s) 18:00-24:00	Water flowrate (kg/s) 24:00-08:00
1	0.01	45	80	2	2	-
2	0.01	45	80	2	2	-
3	0.01	20	80	1	2	0.5
4	0.015	25	85	1	2	0.5
5	0.02	30	85	1	2	0.5
6	0.02	35	95	1	2	0.5
7	0.02	35	95	1	2	0.5
8	0.02	35	95	1	2	0.5
9	0.015	35	85	1	2	0.5
10	0.01	30	85	1	2	0.5
11	0.01	45	80	2	2	-
12	0.01	45	80	2	2	-

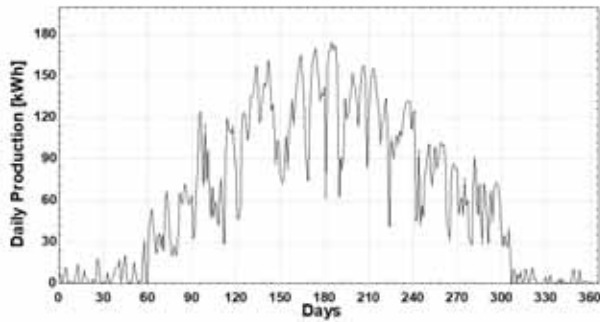


Figure 6. Daily produced electricity

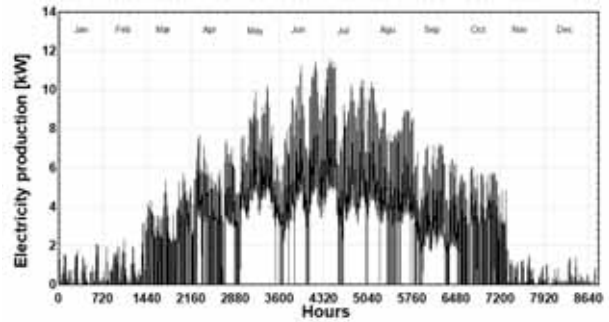


Figure 8. Hourly produced electricity

ces electricity between 08:00 and 18:00. When sun sets, peak demand period starts, water flow rate is adjusted to provide higher output until 24:00. The last period is from 24:00 to 08:00. During the last period, the circulation water mass flow rate is switched to 0.5 kg/s, as generation of a high amount of electricity is not required. Simulations are conducted considering both aforementioned strategies and also every per day's irradiance profile.

Fig. 6 shows daily produced electricity as kWh. Four months (namely November, December, January and February) are adjusted for CHP mode so output is quite low. Additionally, large fluctuations are observed throughout the year regarding electricity outputs. These fluctuations occur as the solar irradiance does not follow a stable trend naturally. The control strategy allows these sharp decrements for conserving the thermal energy in the tank for following day.

Stop criterion is activated when condition is provided thus, the ORC pump is turned off and electricity production ends for this certain day.

To understand the specifications of CHP operation, Fig 7a is given to compare CHP and sole power generation modes. It is clearly seen from the figure that electricity output is lower in CHP mode. The main reason is a higher condensing temperature which causes a lower expansion ratio in the expander. However, high condensing temperature allows the use of condensing heat for other purposes for example space heating. Fig 7b shows produced condensing heat on a daily basis. The trend is quite similar with electricity generation as heat can only be obtained while the ORC is working. CHP mode is active for four months and received useful heat is recorded as 19344.7kWh.

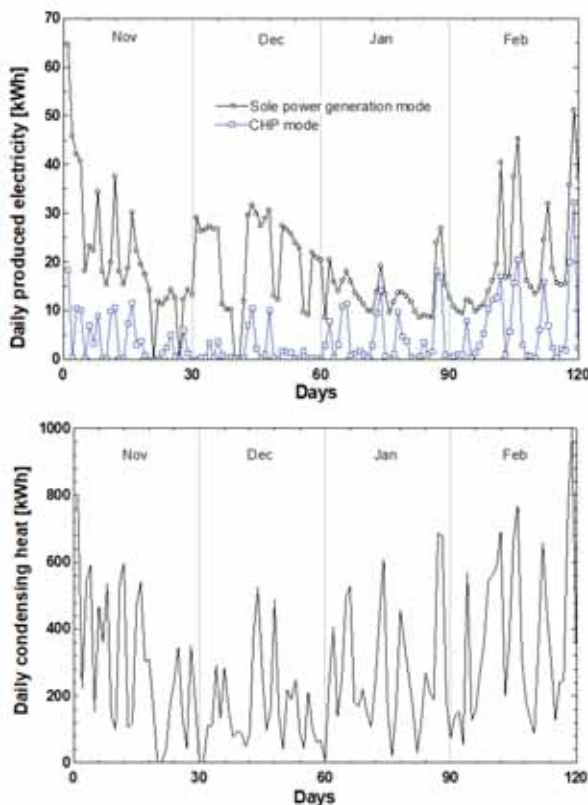


Figure 7. Comparison of outputs of the CHP and sole power generation modes and condensing heat for space heating

One of the aims of this study is matching the electricity output with demand during the operation. Therefore, electricity yield is given in Fig. 8. The figure shows the effect

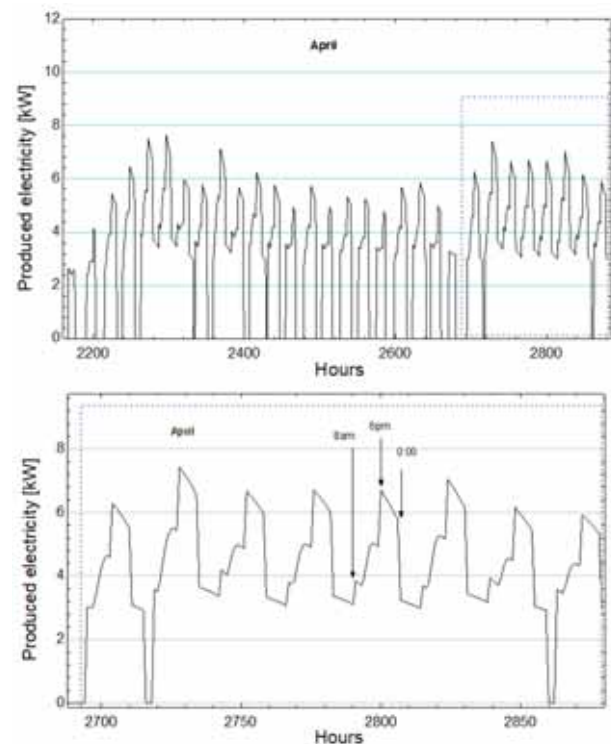


Figure 9. April hourly production

of the CHP mode on production in the winter period and as expected, higher output in summer period. In order to clearly observe the output trend and continuous production profile, there should be zoomed on a specified month. Fig. 9 presents the electricity production profile during April. Since April is a transition month, the output profile is also of a similar nature. From April, continuous (24h) production begins to form. Fig.9 shows that the 24hr production is observed for 11 days. When focusing on the last 8 days, continuous production and controlling hours can be seen clearly.

The last figure is plotted to offer an explanation of different outputs. June and September electricity generations and water tank top temperatures are compared in Fig. 10. Since these two months have the same condensing temperature, the only effecting parameter on output is the evaporating temperature which is directly related with top temperature. Thus, it is obvious that three days have almost the same output and top temperature in Fig.10.

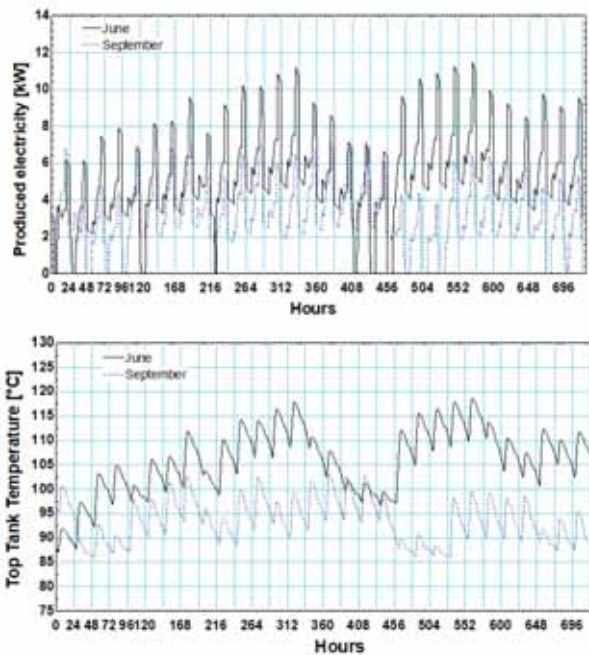


Figure 10. Comparison between June and September

Heat losses to the environment from the tank are also considered, compared and calculated as 5251 kWh during June and 4451 kWh during September. The difference is approximately 15% but produced electricity difference falls by almost 40%. This figure shows wasted heat from heat loss is a serious problem which cannot be neglected as even the ORC stops, heat loss from tank to environment never ends until to be same temperature with ambient.

CONCLUSION

In this study, a solar-driven Organic Rankine Cycle was investigated for a year with consideration given to mee-

ting electricity demand. Components were modelled and analyzed in a transient state for the whole year. When weak solar irradiance was available in the winter period, operation was switched into CHP mode and the system produced heat and power simultaneously. Weather conditions were used as real data and performance was predicted under real conditions. The system also focused on control strategies. On the basis of the presented study, the following conclusions can be written:

- EFP collectors have been successfully implemented in the ORC system even for low irradiance periods for CHP operation.
- Although solar ORC performance totally depends on an irradiance profile, by controlling the system operation, it is possible to conserve the stored heat for next day with dispensable late-night production. However, this intermitted generation causes sharp falls in daily electricity production.
- 24hrs production needs sufficient solar irradiance. According to simulation 24hrs production occurs by April, but it depends on weather conditions.
- Electricity output depends on control strategies. Stop criteria assignment is one of the main parameters to obtain magnitude of output and production time in daily basis.
- Using 550m² collector area, 23296.8 kWh electricity has been produced considering the demand pattern for ten dwellings in year.

References

1. Chan A, Hughes M. Further Analysis of Data from the HEUS Correlation of Consumption with Low Carbon Technologies. Elementenergy, March, (2014).
2. Hayn M, Bertsch V, Fichtner W. Electricity load profiles in Europe: The importance of household segmentation. *Energy Res. Soc. Sci.* 3 (2014) 30–45.
3. Freeman J, Guarracino I, Kalogirou SA, Markides C N. A small-scale solar organic Rankine cycle combined heat and power system with integrated thermal energy storage. *Appl. Therm. Eng.* 127 (2017) 1543–1554.
4. Chacartegui R, Vigna L, Becerra JA, Verda V. Analysis of two heat storage integrations for an Organic Rankine Cycle Parabolic trough solar power plant. *Energy Convers. Manag.* 125 (2016) 353–367.
5. Li J, Li P, Gao G, Pei G, Su Y, Ji J. Thermodynamic and economic investigation of a screw expander-based direct steam generation solar cascade Rankine cycle system using water as thermal storage fluid. *Appl. Energy* 195 (2017) 137–151.
6. Kutlu C, Li J, Su Y, Pei G, Riffat S. Off-design performance modelling of a solar organic Rankine cycle integrated with pressurized hot water storage unit for community level application. *Energy Convers. Manag.* 166 (2018) 132–145.

7. Freeman J, Hellgardt K, Markides CN. Working fluid selection and electrical performance optimisation of a domestic solar-ORC combined heat and power system for year-round operation in the UK. *Appl. Energy*. 186 (2017) 291–303.
8. Calise F, D'Accadia MD, Vicidomini M, Scarpellino M. Design and simulation of a prototype of a small-scale solar CHP system based on evacuated flat-plate solar collectors and Organic Rankine Cycle. *Energy Convers. Manag.* 90 (2015) 347–363.
9. Bellos E, Tzivanidis C, Symeou C, Antonopoulos KA. Energetic , exergetic and financial evaluation of a solar driven absorption chiller – A dynamic approach. *Energy Convers. Manag.* 137 (2017) 34–48.
10. Declaye S, Quoilin S, Guillaume L, Lemort V. Experimental study on an open-drive scroll expander integrated into an ORC (Organic Rankine Cycle) system with R245fa as working fluid. *Energy*. 55 (2013) 173–183.
11. Crawley DB, Lawrie LK, Pedersen CO, Winkelmann FC. *EnergyPlus: Energy Simulation Program*. ASHRAE J. 42 (2000) 49–56.

